Natural source zone depletion of petroleum hydrocarbons under variable temperature and moisture conditions

by

Mehdi Ramezanzadeh

A thesis

presented to the University of Waterloo

in fulfillment of the

thesis requirement for the degree of

Master of Science

in

Earth Sciences

Waterloo, Ontario, Canada, 2023

Author's declaration

This thesis consists of material all of which I authored or co-authored: see Statement of Contributions included in the thesis. This is a true copy of the thesis, including any required final revisions, as accepted by my examiners. I understand that my thesis may be made electronically available to the public.

Statement of contributions

Chapters 2 and 3 of this thesis consist of two co-authored, manuscript-format papers. As the first author, I was primarily responsible for the study design, execution, data collection and analysis, and writing. The contributions of the listed co-authors are as follows:

The experiments and numerical simulations were designed by me and Stephanie Slowinski. All laboratory work was carried out by me, with the assistance of Stephanie Slowinski, Kathleen Murr, Christina Lam, Jane Ye, and Marianne Vandergriendt for sample and data analyses. Christina Smeaton and Clement Alibert contributed to data analysis and interpreting the data. Fereidoun Rezanezhad and Philippe Van Cappellen supervised the project and helped me interpret the data. All authors contributed to the preparation of the manuscripts and have approved its final version.

Abstract

In subsurface environments contaminated by petroleum hydrocarbons (PHCs), the steep geochemical and redox gradients near the water table, the oxygen availability, moisture content, salinity, pH, nutrient concentrations and temperature, modulate microbial pathways and process rates that affect the fate of hydrocarbons. The reactive transport of PHCs is strongly controlled by hydrological and climatic forcings, including water table fluctuations (WTFs) and freeze-thaw cycles (FTCs), which cause large temporal variations in the local geochemical conditions and the distributions of temperature and soil water content which are key determinants of natural source zone depletion (NSZD) process rates. FTCs and WTFs modify the biogeochemical and physical processes controlling the biodegradation of PHCs and the associated generation of methane (CH_4) and carbon dioxide (CO_2). Therefore, understanding the impacts of FTCs and WTFs in PHC-contaminated soils and groundwater is critical for environmental risk assessment and natural attenuation of PHCs.

A diffusion-reaction model that accounts for the effects of FTCs on methanogenic toluene biodegradation was developed. The model is verified against data generated from a 215 day-long batch experiment with soil collected from a PHC contaminated site in Ontario, Canada. The fully saturated soil was exposed to successive 4-week FTCs under anoxic conditions with temperatures fluctuating between -10°C and +15°C. The headspace gas for the concentrations and ^{13}C isotope compositions of CH_4 and CO_2, and the porewater for pH, acetate, dissolved organic and inorganic carbon, and toluene were analyzed. The model represents solute diffusion, volatilization, sorption, as well as a reaction network of 13 biogeochemical processes. The model successfully simulated the soil porewater and headspace concentration time series by representing the temperature dependencies of microbial reaction and gas diffusion rates during FTCs. According to the model results, the observed increases in the headspace concentrations of CH_4 and CO_2 by 87% and 136%, respectively, following toluene addition are due to toluene fermentation and subsequent methanogenesis reactions. The experimental results and model simulations both confirm that methanogenic degradation under anoxic soil conditions is the dominant reaction for toluene attenuation, representing 74% of the attenuation, with sorption contributing to 11%, and volatilization contributing to 15%. Also, the model-predicted contribution of acetate-based

methanogenesis to total produced CH_4 agrees with that derived from the ^{13}C isotope data. The freezing-induced soil matrix organic carbon release is considered as an important process causing an increase in dissolved organic carbon (DOC) following each freezing period according to the calculations of carbon balance and specific UV absorbance (SUVA) index. The simulation results of a no FTC scenario indicate that, in the absence of FTCs, CO_2 and CH_4 generation would decrease by 29% and 26%, respectively, and that toluene would be biodegraded 23% faster than in the FTC scenario. Given its ability to represent the dominant processes controlling CH_4 and CO_2 fluxes and porewater chemical changes, this modelling approach can be used to simulate the sensitivity of soil biodegradation processes to FTC frequency and duration driven by temperature fluctuations in anoxic soil conditions.

A ten-month soil column experiment to simulate the effects of water table fluctuations on methanogenic PHCs biodegradation rates and pathways was conducted. Eight columns were filled with 45 cm of undisturbed soil core samples collected from a PHC contaminated site in London, Ontario. Four columns simulating fluctuating water table conditions were subjected to three successive 3-week cycles of drainage and imbibition. In the remaining four columns, the soils remained saturated over the period of the experiment, simulating a static water table. The responses to the imposed water table fluctuations and ethanol/naphthalene injections were monitored by measuring soil surface CO_2 and CH_4 effluxes, dissolved CO_2 and CH_4 concentrations, depth-dependent moisture content, $\delta^{13}C$ isotope composition of CO_2 and CH_4, DOC, dissolved inorganic carbon (DIC), and major anions at the end of each drainage-imbibition cycle. The results show that maximum CO_2 and CH_4 effluxes were up to 10 times higher during the drainage periods than during the imbibition periods due to the release of accumulated CO_2 and CH_4 and aerobic degradation. Also, the average dissolved CH_4 concentration decreased by 29% during the drainage periods because of the release of CO_2 and CH_4, aerobic CH_4 oxidation, and inhibition of methanogenesis in the presence of O_2, while the average dissolved CO_2 increased by 105% due to the oxidation of DOC and CH_4. The results of $\delta^{13}C$ for CO_2 and CH_4 show that the prevailing methanogenic pathway shifted from hydrogen-based methanogenesis to acetate-based methanogenesis in the ethanol/naphthalene spiked soils due to the increase in acetate concentrations. In the fluctuating columns, CH_4 oxidation became the prevailing pathway controlling CH_4 flux dynamics after the first drainage period. Moreover, naphthalene was

consumed 29% faster in the fluctuating columns compared to the static soil columns. Both experiment and model demonstrate that there is a trade-off associated with water table fluctuations: lowering the water level can exacerbate global warming via more CO_2 and CH_4 effluxes, while this is effective for PHC attenuation. The results of this study shed new light on the role of the soil drying and rewetting effects on methanogenic hydrocarbon degradation and CO_2 and CH_4 effluxes.

Acknowledgements

Words cannot express my deepest gratitude to my supervisors, Dr. Fereidoun Rezanezhad and Dr. Philippe Van Cappellen who perfectly guided my education from the day first. Encouraging critical thinking, being an independent researcher and adopting interdisciplinary approaches are just a few of their great advice that help me during my study. I am also grateful to the members of my thesis committee members Dr. Neil Thomson and Dr. David Rudolph for taking time to review my thesis and for their invaluable comments to improve my work.

Thanks should also go to Stephanie Slowinski, for all her supports and constructive comments and for always being able to answer my questions– your advice has been so valuable to me. Many thanks to Marianne VanderGriendt, whose diligent training in the lab throughout my time with Ecohydrology Research Group is a major reason for the success of my Masters research.

I greatly appreciate the financial support for this research which came from the Canada Excellence Research Chair (CERC) program, a Natural Sciences and Engineering Research Council Partnership Grant with Imperial Oil Resources Ltd. (Collaborative Research and Development Grant to Van Cappellen: CRDPJ: 533227-18), and Global Water Futures (Canada Excellence Research Fund).

My thanks go to everyone in the Ecohydrology Research Group who taught me something in the lab, helped me interpret the results, or shared encouraging words with me. Thank you to Jane Ye for your guidance and your endless encouragement. I also want to thank Dr. Shuhuan Li, Tara Ferguson, Maitri Lad, Richard Dinh Pham, Danielle Green, Hannah Adams, Laurel McBride, Shirley Chatten, and Christina Lam for their assistance with laboratory experiments and analyses.

And last but not the least, I would like to thank my mom, dad and sisters for their constant love and support. I dedicate this thesis to them whom I owe everything.

Table of Contents

List of figures

List of tables

List of abbreviations

FTCs	Freeze-Thaw Cycles
WTFs	Water Table Fluctuations
PHCs	Petroleum Hydrocarbons
CH_4	Methane
CO_2	Carbon dioxide
O_2	Oxygen
H_2	Hydrogen
N_2O	Nitrous oxide
NO_3^-	Nitrate
Fe^{3+}	Iron
Mn^{4+}	Manganese
SO_4^{2-}	Sulfate
HCO_3^-	Bicarbonate
$C_3H_5O_3^-$	Lactate
$C_2H_3O_2^-$	Acetate
$C_6H_{12}O_6$	Glucose
C_7H_8	Toluene
$C_{10}H_8$	Naphthalene
C_2H_6O	Ethanol
NSZD	Natural Source Zone Depletion
GHG	Greenhouse gas
DOC	Dissolved organic carbon
DIC	Dissolved inorganic carbon
IC	Ion chromatography
EC	Electrical conductivity
EA	Electron acceptor
ED	Electron donor
HBM	Hydrogen-based methanogenesis
ABM	Acetate-based methanogenesis
C	Carbon
N	Nitrogen
NL	No lactate added
LA	Lactate amended
BES	2-bromoethanesulfonate (BES) amended
TA	Toluene amended
FEN	Fluctuating ethanol-naphthalene amended columns
SEN	Static ethanol-naphthalene amended columns
FEC	Fluctuating ethanol control column
SEC	Static ethanol control column
FWC	Fluctuating water control column
SWC	Static water control column

List of symbols

ϕ	Porosity
ϕ_e	Effective porosity
ρ_b	Bulk density
c_i	Concentration of a specimen i
α_{CO_2/CH_4}	The fractionation factor between CO_2 and CH_4
α_{obs}	The α_{CO_2/CH_4} values observed during the experiment
α_{HBM}	The average value of the α_{CO_2/CH_4}values reported for HBM
α_{ABM}	The average value of the α_{CO_2/CH_4}values reported for HBM
f_{ABM}	The fraction of methane produced by ABM
R_i	Reaction rate of substance *i*
$J_{d,i}$	Diffusive flux tensor for each substance
$D_{e,i}$	Effective diffusion coefficient for substance *i*
ρ_b	Bulk density
$c_{p,i}$	Langmuir adsorption isotherm foI substance *i*
θ_l	Soil water content
$c_{pmax,i}$	Maximum adsorption capacity fIr substance *i*
$K_{L,i}$	Langmuir constant for substance *i*
r_j	The rate of *j*th reaction in a reaction network
$\nu_{i,j}$	Stoichiometric coefficient of specimen *i* in the reaction *j*
C_{ED}	Concentration of electron donors
C_{EA}	Concentration of electron acceptors
T_{min}	Minimum temperature
T_{max}	Maximum temperature
T_{opt}	Optimum temperature
pH_{min}	Minimum pH
pH_{max}	Maximum pH
pH_{opt}	Optimum pH
$K_{inh,i,j}$	Inhibition constant Ior substance *i* in reaction *j*
$r_{inh,j}$	Inhibition factor
K_i^H	Henry constant for substance *i*
K_d	Sorption distribution coefficients
θ_g	Volume fraction of gas phase in soil for substance i
$k_{G,i}$	Volatilization of substance *i*
$D_{L,i}$	Solute diffusion coefficients for substance *i* in the aqueous phase
$D_{G,i}$	Solute diffusion coefficients for substance *i* in gas phase
C_m	Specific moisture capacity
S_{ew}	Effective saturation
S	Storage coefficient
H_p	Pressure head
H	Hydraulic head
Eh	Redox potential

1 Introduction

1.1 Natural source zone depletion at petroleum hydrocarbon contaminated sites

Contamination of subsurface environments by petroleum hydrocarbons (PHCs) is one of the major global environmental issues because some PHCs pose a significant threat to human health due to their high toxicity (Mayer & Hassanizadeh, 2005). Thus, it is important to comprehend the fate, transport and distribution of PHCs, and major hydrologic and climatic factors affecting remediation of PHCs (Ossai *et al.*, 2020). Natural source zone depletion (NSZD) of PHCs due to biodegradation, dissolution, sorption, and volatilization as an effective remediation approach has been attracting attention in the last few decades (Garg *et al.*, 2017).

A conceptual diagram of the microbial reactions (*i.e.*, respiration, fermentation, and methanogenic pathways) leading to NSZD in a PHC-contaminated subsurface environment is presented in Figure 1-1. As illustrated in this diagram, aerobic and anaerobic respiration takes place where the reduction of electron acceptors (EA) such as oxygen (O_2), nitrate (NO_3^-), iron (III) (Fe^{3+}), manganese(IV) (Mn^{4+}), and sulfate (SO_4^{2-}) is coupled to the oxidation of a PHC as an electron donor (ED). These electron acceptors might become scarce in a PHC-contaminated zone because of respiration or variable hydrological and climatic regimes (Haberer *et al.*, 2012). As a result, fermentative and methanogenic degradation of PHCs under anoxic condition become the dominant pathways leading to much more methane (CH_4) and carbon dioxide (CO_2) emissions. Therefore, comprehending the factors modulating the degradation pathways and greenhouse gas (GHG) emissions in PHC-contaminated sites is crucial for understanding NSZD processes and the impacts of PHC degradation on the climate system (Jones *et al.*, 2008).

Methanogenic pathways produce methane (CH_4), an important greenhouse gas (GHG) with 25 times the warming potential of CO_2, and thus understanding the controls on both CH_4 and CO_2 production is very important for comprehending the impacts of PHC degradation on the climate system (Dean *et al.*, 2018; Lemming *et al.*, 2012). There are two major microbial methane producing (*i.e.*, methanogenic) reactions: aceticlastic methanogenesis or acetate-based methanogenesis (ABM) produces both CH_4 and CO_2, while the other, hydrogenotrophic methanogenesis or hydrogen-based methanogenesis (HBM), consumes CO_2 to produce CH_4 (Conrad, 2020). Thus, the relative rates of these two major methanogenic pathways modulates the rates and amounts of CH_4 and CO_2. The rates of ABM and HBM depend on many different factors,

such as temperature, moisture content, and the availability of an organic substrate. In saturated electron acceptor-limited environments, fermentative microbial metabolisms are energetically favourable, and the accumulation of acetate, hydrogen (H_2) and CO_2 as products of the fermentation reactions enhance the rates of ABM and HBM (Blake *et al*., 2015; Jones *et al*., 2008).

Among the NSZD processes, methanogenic biodegradation has been recognized as a dominant NSZD process at PHC-contaminated sites in recent years (Conrad, 2020; Essaid *et al*., 2015; Garg *et al*., 2017; N. J. Sihota *et al.*, 2011; Sihota and Mayer, 2012). Methanogenic NSZD brings about an interesting potential tradeoff: more methanogenic biodegradation decreases harmful PHC concentrations in soils, while also increasing CH_4 emissions to the atmosphere. While ex-situ contaminant remediation methods are known to be sources of GHGs (Ellis & Hadley, 2009), the contribution of in-situ natural remediation (*i.e.*, NSZD) to GHG emissions relative to these ex-situ remediation options is still not clear (Garg *et al.*, 2017). Therefore, it is important to understand the impacts of the different environmental factors modulating PHC consumption rates and CH_4 and CO_2 emissions during methanogenic NSZD biodegradation activity.

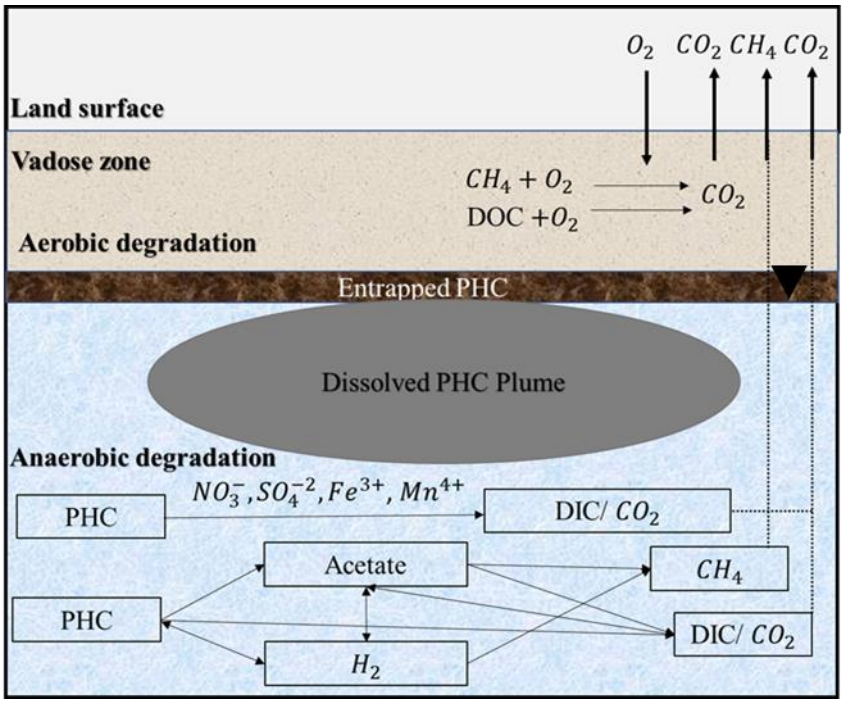

Figure 1-1: Conceptual diagram of microbial reaction network in a PHC-contaminated subsurface environment.

1.2 Environmental factors influencing NSZD processes

Climate variability is one of the main environmental factors controlling NSZD processes because it causes large variations in the spatial and temporal distributions of temperature and soil water content, which in turn modulate the rates of physical, geochemical and microbial processes that contribute to NSZD in contaminated soils (Chang *et al*., 2011, Sihota *et al.*, 2016). Cold regions are warming much faster than the global average, resulting in more frequent and intense freeze-thaw cycles (FTCs). Frequent FTCs can modulate microbial activity (Song *et al.*, 2017), soil physical properties (Ding *et al.*, 2019), and transport processes (Byun *et al.*, 2021; Öquist *et al.*, 2004). Moreover, Climate change can contribute to extreme drought and precipitation events, influencing soil moisture dynamics and water table fluctuations (Christiansen *et al.*, 2017; Dinsmore *et al.*, 2009). Water table fluctuations (WTFs) can have a significant impact on the distribution of O_2 and other electron acceptors, contaminants and natural organic matter, nutrients, and microorganisms (Rezanezhad *et al.*, 2014; Rühle *et al.*, 2015). Therefore, understanding how PHC NSZD processes respond to large temporal variations in soil moisture and temperature regimes during WTFs and FTCs is vital for predicting the fate and transport of PHCs and the associated CH_4 and CO_2 effluxes at PHC-contaminated sites.

The effect of FTCs on NSZD processes becomes even more important in the era of global warming because cold regions are warming much faster than the global average, with the fastest warming happening during the winter (Koenigk *et al.*, 2013; Natali *et al.*, 2019; Rafat *et al.*, 2021) . In fact, warmer winters result in more frequent and intense FTCs due to the variations in the duration and the thickness of snow cover (Zhang *et al*., 2005). Subsurface environments contaminated by PHCs at high latitudes are subjected to freeze-thaw cycles (FTCs), which can have significant impacts on soil physical properties (Ding *et al*., 2019; Ferrick and Gatto, 2005; McCarter *et al*., 2020), microbial community composition and microbial activity (Matzner and Borken, 2008; Sawicka *et al*., 2010; Song *et al*., 2017), as well as gas and nutrients transport processes and rates (Byun *et al*., 2021; Henry, 2007; Krogstad, 2021; Öquist *et al*., 2004; Wagner-Riddle *et al*., 2017).

Growing attention has been paid to the effect of FTCs on CO_2 and CH_4 gas production, and soil carbon and nitrogen dynamics in recent years (*e.g.*, Natali *et al.*, 2019; Rafat *et al*., 2021; Song *et al*., 2017; Voigt *et al*., 2019; Wu *et al*., 2020). Sihota *et al*. (2016) revealed that subsurface gas

transport processes and NSZD rates at PHC-contaminated sites vary seasonally due to variations in temperature profiles in the vadose zone and the presence of a physical ice barrier to gas transport in the winter. Some studies have highlighted the importance of seasonal soil FTCs for their significant contribution to annual soil CO_2 and CH_4 gas production during thaw periods (Kraev *et al.*, 2017; Öquist *et al*., 2004; Rafat *et al*., 2021; Voigt *et al*., 2017; Wagner-Riddle *et al.*, 2017; Wang *et al*., 2019). These studies confirm FTCs modulate CO_2 and CH_4 gas production because temperature is a major factor controlling the rates of CO_2 and CH_4 production, and the temporal presence of an ice layer during freezing periods can inhibit gas transport and result in lower surface CO_2 and CH_4 effluxes and higher CO_2 and CH_4 concentrations compared to thaw periods. Although previous studies have investigated NSZD processes and rates under variable environmental conditions, the impacts of FTCs on the methanogenic biodegradation of PHCs and the consequent generation of CH_4 and CO_2 in anoxic electron acceptor-limited environments are still not well understood.

Soil moisture is a major factor controlling redox conditions and the rates of physical, geochemical and microbial processes contributing to NSZD (Keiluweit *et al.*, 2016, 2017; Moyano *et al.*, 2013; Pronk *et al.*, 2020; Prowse *et al.*, 2009) since it modulates the distribution of O_2 and other electron acceptors, contaminants and natural organic matter, nutrients, and microorganisms in the subsurface (Haberer *et al.*, 2012; Holden & Fierer, 2005; Lin *et al*., 2012; Rezanezhad *et al.*, 2014; Rühle *et al*., 2015; Williams & Oostrom, 2000). The rates of GHG effluxes and PHCs degradation can potentially be affected by groundwater level fluctuations (Henneberg *et al.*, 2016). In fact, high water level leads to greater generation of CH_4 because of aceticlastic methanogenesis and hydrogenotrophic methanogenesis under anoxic condition (Brewer *et al.*, 2018; Conrad, 2020; Von Fischer & Hedin, 2007; Günther *et al.*, 2020; Sexstone *et al.*, 1985; Sun *et al.*, 2012), while it lowers the rates of hydrocarbon degradation and CO_2 generation (Basiliko *et al.*, 2009; Brewer *et al.*, 2018; Christiansen *et al.*, 2016; Pronk *et al.*, 2020; Sierra *et al.*, 2017; Van De Ven *et al.*, 2021). However, water table decline usually decreases CH_4 generation due to inhibition of methanogeneis or oxidation of CH_4 in the presence of O_2, whereas this decline increases CO_2 effluxes and PHC degradation because of higher aerobic degradation rates and greater upward diffusion (Christiansen *et al.*, 2016; Elberling *et al.*, 2011; Klüpfel *et al.*, 2014; Pronk *et al.*, 2020; Sihota *et al.*, 2011; Van De Ven *et al.*, 2021).

In recent years, growing attention has been directed to the influence of soil moisture dynamics on climate change mitigation (*e.g.*, Berglund & Berglund, 2011; Günther *et al.*, 2020; Leifeld *et al.*, 2019; Xue *et al.*, 2020). Recent studies have shown how drained peatlands might exacerbate global warming through continued CO_2 and CH_4 effluxes, whereas peatland rewetting is effective for climate change mitigation, despite the increase in CH_4 generation (Franz *et al.*, 2016; Günther *et al.*, 2020; Hahn *et al.*, 2015; Leifeld *et al.*, 2019). Van De Ven *et al.* (2021) quantified the impact of WTFs on NSZD rates in a biodiesel-contaminated sandtank. They state that WTFs affect surface effluxes due to the redistribution of contaminants, increased aerobic degradation, and the liberation of anaerobically produced gas accumulated below the water table.

There are many studies that have investigated the impact of WTFs and soil moisture dynamic on carbon turnover, but the methanogenic biodegradation of PHCs and the resultant CO_2 and CH_4 effluxes in soils undergoing WTFs and variable moisture regime has not been investigated in detail. Hence, understanding how NSZD of PHCs responds to large temporal variations in soil moisture regime during WTFs is vital for predicting NSZD rates and the associated soil CH_4 and CO_2 effluxes (Klüpfel *et al.*, 2014; Moyano *et al.*, 2013; Pronk *et al.*, 2020).

1.3 Thesis objectives

The overall objective of this research is to delineate the effects of WTFs and FTCs on methanogenic biodegradation of PHCs and the consequent generation of CH_4 and CO_2 through two research projects using experiments and numerical simulations.

The specific objectives addressed in Chapter 2 were:

1) monitor the responses of methanogenic biodegradation of PHCs to FTCs by measuring headspace CO_2 and CH_4 concentrations, PHC concentrations, $\delta^{13}C$ isotope composition of CO_2 and CH_4, alongside other geochemical variables in PHC-contaminated soil batch experiments subjected to temperature fluctuations between -10°C and +15°C.
2) develop a diffusion-reaction model to simulate the effect of FTCs on physical, geochemical, and microbial processes and rates, and hence to simulate the experimental results.

The specific objectives addressed in Chapter 3 were:

1) monitor the responses of methanogenic biodegradation of PHCs to WTFs by measuring CO_2 and CH_4 effluxes, dissolved CO_2 and CH_4, depth-dependent moisture content, and dissolved O_2 concentrations, and by analyzing the porewater chemistry at the end of each drainage-imbibition cycle.
2) develop a diffusion-reaction model to simulate the impact of WTFs on NSZD of PHCs and the consequent effluxes of CO_2 and CH_4.

1.4 Thesis outline

This thesis comprises three additional chapters. Chapter 2 consists of a manuscript submitted to the Journal of *Chemosphere* (Impact Factor: 8.943). The manuscript was written as a stand-alone document but has been modified slightly in this thesis for consistent formatting. This chapter describes a batch experiment and numerical simulation investigating the effects of FTCs on PHC degradation and CO_2 and CH_4 generations. Chapter 3 comprises a soil column experiment and numerical simulation examining the impact of WTFs on CO_2 and CH_4 emissions and NSZD of PHCs. Chapter 4 consists of overall conclusions, recommendations, and future research opportunities. The appendix includes additional experimental results that are not included in Chapters 2 and 3.

Effects of Freeze-Thaw Cycles on Methanogenic Hydrocarbon Degradation: Experiment and Numerical Simulation

Mehdi Ramezanzadeh[1†*], Stephanie Slowinski[1†], Fereidoun Rezanezhad[1], Kathleen Murr[1], Christina Lam[1], Christina Smeaton[2], Clement Alibert[1], Marianne Vandergriendt[1], and Philippe Van Cappellen[1]

[1] Ecohydrology Research Group, Department of Earth and Environmental Sciences and Water Institute, University of Waterloo

[2] School of Science and the Environment, Grenfell Campus, Memorial University of Newfoundland, Canada

†Authors contributed equally to this work.

[*]Corresponding author: Mehdi Ramezanzadeh
Ecohydrology Research Group, Department of Earth and Environmental Sciences and Water Institute, University of Waterloo
200 University Avenue West, Waterloo, Ontario, Canada N2L 3G1
Email: m8ramezanzadeh@uwaterloo.ca

This chapter has been submitted the journal *Chemosphere*:

M. Ramezanzadeh, S. Slowinski, F. Rezanezhad, K. Murr, C. Lam, C. Smeaton, C. Alibert, M. Vandergriendt, and P. Van Cappellen. Effects of Freeze-Thaw Cycles on Methanogenic Hydrocarbon Degradation: Experiment and Numerical Simulation. *Chemosphere*, CHEM112628, (Under Review)

2 Effects of Freeze-Thaw Cycles on Methanogenic Hydrocarbon Degradation: Experiment and Numerical Simulation

2.1 Introduction

Natural source zone depletion (NSZD) of PHCs in the subsurface due to dissolution, volatilization, sorption, and most significantly biodegradation as an effective remediation approach has been increasingly attracting attention in the last few decades due to advances in understanding of microbiogeochemical processes and environmental capacity to degrade PHC constituents under varying conditions over time (BenIsrael *et al.*, 2019; Garg *et al.*, 2017; Khasi *et al.*, 2019; Kulkarni *et al.*, 2020; Ramezanzadeh *et al.*, 2022; Shi *et al.*, 2020). Figure 2-1 conceptualizes the microbial reactions leading to NSZD in soil subsurface of a PHC-contaminated site whereby PHC degradation is governed by respiration, fermentation, and methanogenic pathways. Respiration is an important subsurface PHC biodegradation pathway whereby the oxidation of a PHC (*i.e.*, electron donor (ED)) is coupled to the reduction of electron acceptors such as oxygen (O_2), nitrate (NO_3^-), iron(III) (Fe^{3+}), manganese(IV) (Mn^{4+}), and sulfate (SO_4^{2-}). However, electron acceptors are depleted at many PHC-contaminated sites because the PHC contaminants are in excess of the electron acceptors or because of transport constraints (*e.g.*, ice formation at the soil surface) (Garg *et al*., 2017; Irianni-Renno *et al*., 2016; Karimi Askarani *et al*., 2018). Hence, fermentative microbial metabolisms become energetically favourable, and acetate, hydrogen (H_2) and carbon dioxide (CO_2) accumulate in the subsurface (Blake *et al*., 2015; Jones *et al*., 2008) such that fermentation and methanogenic pathways become the dominant process leading to NSZD in PHC-contaminated zones. There are two major microbial methane producing (*i.e.*, methanogenic) reactions: acetate-based methanogenesis (ABM) produces both CH_4 and CO_2, while the other, hydrogen-based methanogenesis (HBM), consumes CO_2 to produce CH_4 (Conrad, 2020).

Climate variability is one of the main environmental factors controlling NSZD processes because it causes large variations in the spatial and temporal distributions of temperature and soil water content, which in turn modulate the rates of physical, geochemical and microbial processes that contribute to NSZD in contaminated soils (Chang *et al*., 2011, Sihota *et al.*, 2016). Subsurface environments contaminated by PHCs at high latitudes are subjected to freeze-thaw cycles (FTCs), which can have significant impacts on soil physical properties (Ding *et al*., 2019; Ferrick and Gatto, 2005; McCarter *et al*., 2020), microbial community composition and microbial activity

(Matzner and Borken, 2008; Sawicka *et al*., 2010; Song *et al*., 2017), as well as gas and nutrients transport processes and rates (Byun *et al.*, 2021; Green *et al.*, 2022; Henry, 2007; Krogstad, 2021; Öquist *et al.*, 2004; Wagner-Riddle *et al.*, 2017).

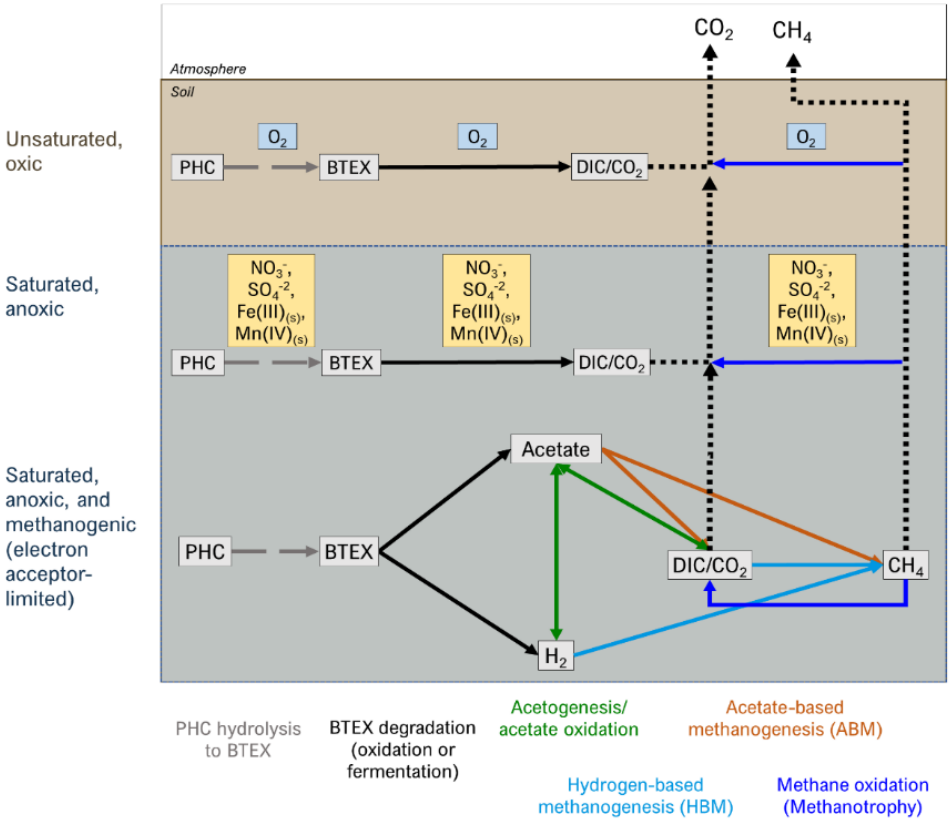

Figure 2-1: Conceptual diagram of microbial reaction network in a PHC-contaminated subsurface environment.

The impact of FTCs on NSZD processes and the generation of CO_2 and CH_4 has been studied by a number of laboratory, field, and modeling studies (*e.g.*, Byun *et al*., 2021; Garg *et al*., 2017; Henry, 2007; Matzner and Borken, 2008; Schimel and Clein, 1996; Song *et al*., 2017). Growing attention has been paid to the effect of FTCs on CO_2 and CH_4 gas production, and soil carbon and nitrogen dynamics in recent years (*e.g.*, Natali *et al.*, 2019; Rafat *et al*., 2021; Song *et al*., 2017; Voigt *et al*., 2019; Wu *et al*., 2020). Column studies have linked the cycling of carbon and nitrogen to changes in pore structure and the formation of a physical ice barrier during FTCs (Ding *et al.*, 2019; Krogstad, 2021; Sharma *et al.*, 2006; Teepe *et al.*, 2001) . A number of field studies have highlighted the importance of seasonal soil FTCs for their significant contribution to annual soil CO_2 and CH_4 gas production during the thaw periods (Kraev *et al.*, 2017; Öquist *et al*., 2004; Rafat

et al., 2021; Voigt *et al*., 2017; Wagner-Riddle *et al.*, 2017; Wang *et al*., 2019). Furthermore, some other studies used batch experiments to investigate the effects of diurnal FTCs (*i.e.*, temperatures ranging between -5°C and 14°C on a daily basis) on PHC biodegradation rate and soil microbial communities under aerobic conditions (Akbari and Ghoshal, 2015; Chang *et al*., 2011; Eriksson *et al*., 2001). Among the NSZD processes, methanogenic biodegradation has been recognized as a dominant NSZD process at PHC-contaminated sites in recent years (Conrad, 2020; Essaid *et al*., 2015; Garg *et al*., 2017; N. J. Sihota *et al.*, 2011; Sihota and Mayer, 2012). A number of field studies have therefore introduced novel methods, such as surficial gas efflux measurements to accurately measure NSZD rates at PHC-contaminated sites (Amos *et al*., 2005; Bekins *et al*., 2005; Hodgkins *et al*., 2014; Sihota *et al*., 2013; Verginelli *et al*., 2018). Sihota *et al*. (2016) revealed that subsurface gas transport processes and NSZD rates at PHC-contaminated sites vary seasonally due to variations in temperature profiles in the vadose zone and the presence of a physical ice barrier to gas transport in the winter.

In addition to experimental studies, several biogeochemical reactive transport models have been developed to simulate NSZD processes at contaminated sites (Ebrahimi & Or, 2017; Essaid *et al*., 2003; Khasi *et al.*, 2021; K. U. Mayer *et al.*, 2002; Molins *et al.*, 2010; Molins & Mayer, 2007; Ng *et al.*, 2015; Šimůnek & Suarez, 1993; Su *et al.*, 2021; Vencelides *et al.*, 2007). Mayer *et al*. (2002) and Molins and Mayer (2007) combined a biogeochemical reaction network and physical transport processes into a multiphase multicomponent flow and reactive transport model, called MIN3P, which has been used to simulate the reactive transport of PHCs, CO_2 and CH_4 during NSZD at contaminated sites. Later, Molins *et al*. (2010) simulated a PHC-contaminated site using a similar biogeochemical reactive transport model that incorporates a reaction network, multicomponent gas diffusion and advection, and solute transport. Their modeling results confirmed that methanogenic biodegradation is the dominant PHC degradation pathway at a mature PHC-contaminated site. Recent numerical modeling developments have improved reactive transport modeling of PHC-contaminated sites by implementing additional mechanisms for carbon outgassing, dissolved inorganic carbon inputs, pH buffering, and unstructured grid capabilities (Khasi *et al*., 2021; Ng *et al*., 2015; Su *et al*., 2021).

Although previous studies have investigated NSZD processes and rates under variable environmental conditions using some combination of laboratory experiments, field monitoring, and/or reactive transport modeling, the impacts of FTCs on the methanogenic biodegradation of PHCs and the consequent generation of CH_4 and CO_2 in anoxic electron acceptor-limited environments are still not well understood. Therefore, the main goal of this study was to delineate the effects of FTCs on methanogenic toluene biodegradation and CH_4 and CO_2 generation. Using a combined experimental and modeling approach, we: (1) monitored changes in toluene concentrations and CH_4 and CO_2 generation, alongside other geochemical variables, in a soil batch experiment where the soil was subjected to temperature fluctuations between -10°C and +15°C and (2) developed a diffusion-reaction model to simulate the effect of FTCs on physical, geochemical, and microbial processes and rates, and hence to simulate the experimental results. Experimental results were used to validate that the diffusion-reaction model was able to accurately represent all the processes and reactions involved in NSZD during FTCs.

2.2 Materials and Methods

2.2.1 Batch experiment

2.2.1.1 Soil sampling and characterizations

Soil samples were collected from the topsoil (*i.e.*, 0 to 20 cm below ground surface) of a PHC contaminated site in London, Ontario, Canada. We determined the porosity (ϕ), bulk density (ρ_b), and solid-phase organic C and N of the soil using standard procedures. The ϕ and ρ_b were determined gravimetrically following the method of Gardner (1986), and the ϕ was calculated assuming a particle density of 2.65 g cm^{-3}. The ρ_b and ϕ were 1.22 g cm^{-3} and 0.4, respectively. Total organic carbon and nitrogen were determined to be 3.95% and <1% respectively by combustion analysis at 550°C using an Elementar vario EL cube analyzer (method detection limit, MDL, for both organic carbon and nitrogen was 1%).

2.2.1.2 Sacrificial soil incubation experiment

A sacrificial soil incubation experiment was conducted to delineate the relative contributions of electron-acceptor limited respiration versus methanogenesis to toluene biodegradation and to study the impact of freezing and thawing on methanogenic toluene biodegradation. Soil was homogenized by wet sieving through a 2 mm sieve using ultrapure deionized water. Homogenized soil was transferred to an anaerobic chamber (Coy Laboratory Products, 100% N_2 atmosphere)

where 200 g was added to 500 mL glass jars (Bernardin Golden Harvest Mason with a modified lid containing a grey rubber septa for gas sampling) and 100% saturated, mixed with artificial porewater (APW) solution leaving ~300 mL of headspace gas volume in the sealed jars and a soil surface area of ~ 50 cm^2 estimated based on the jar geometry. The APW solution was prepared to closely match the pH, electrical conductivity, and ionic composition of groundwater from the field site containing $NaHCO_3$ (1.00 mM) and $CaCl_2$ (0.80 mM), $KHCO_3$ (1.00 mM) and $MgCl_2$ (0.15 mM) in ultrapure deionized water. In addition, 10 mL L^{-1} of both Wolfe's Trace Mineral Solution and Wolfe's Vitamin Solution were added to prevent nutrient limitation. The APW was further amended to account for the additions/absence of an external electron donor (lactate) and/or a methanogenic inhibitor (*i.e.*, 2-bromoethanesulfonate (BES)). The final APWs consisted of: 1) original APW (*i.e.*, no lactate added (NL)); 2) lactate amended (LA); and 3) 2-bromoethanesulfonate (BES) and lactate amended. Each treatment and time point, except for the time point at day 0, which had only single jars for each treatment, consisted of triplicates giving a total of 93 jars. The LA and BES treatments contained 0.5 mM lactate and the BES treatment contained 40 mM BES. On day 88, an additional 1 mM of lactate was added to the LA and BES treatments to consume the SO_4^{2-} remaining in the soil and thus to stimulate methanogenic conditions. We prepared a series of parallel jars in the same way for each of the three treatments in triplicate (9 jars in total) which we used to monitor the headspace gas concentrations for CH_4 using a LICOR 7810 instrument to determine when the other jars being used for the sacrificial batch experiment had become methanogenic.

2.2.1.3 Experimental conditions

At the start of the experiment, the soil and APW solution were added together to all the 102 incubation jars, stirred together, and placed, uncapped, in an anaerobic chamber (Coy Laboratory Products) for six days to equilibrate with the anoxic atmosphere. Following the six days incubation in the anoxic atmosphere, the samples were sealed and placed in an environmental chamber incubator (Percival I-41NL XC9) set to 10 °C for 60 days to allow for methanogenic conditions to develop (as determined by monitoring CH_4 concentrations in the headspace of the series of parallel jars) before the FTC temperature regime was imposed. Five consecutive cycles of 2-week freezing at -10°C and 2-week thawing periods at 15°C were imposed between day 60 and day 215.

On day 113, following the first freeze thaw cycle and second freezing period, during the 2 week thawing period, a subset of the remaining batch soil jars from each of the three initial treatments (NL, LA, BES) were amended with toluene. For amendment with toluene, the soil and porewater from the subset of jars were opened in an anaerobic chamber and divided into two 250 mL jars equipped with Teflon septa (250 mL Clear Certified Wide Mouth Septa Jar with 58,400 PP Cap with PTFE/Silicone Septum, Thermo Fisher Scientific), and 10 mL of concentrated aqueous toluene solution was added to reach a toluene concentration of around ~15 mg L^{-1}. For the jars where no toluene was added at any point, they are given the no toluene (NT) label. Thus, in total, there were 6 treatments: no-lactate no-toluene (NL-NT), no-lactate toluene amended (NL-TA), lactate-amended no-toluene (LA-NT), lactate-amended toluene-amended (LA-TA), BES-amended no toluene (BES-NT), and BES-amended toluene amended (BES-TA) treatments.

The jars were then sealed and transferred back to the environmental chamber incubator at 15°C for 4 days. During the freezing periods, some jars' glass was broken by the freezing and subsequent water expansion. During the thawing periods, we transferred the soil and porewater in these jars once they were thawed to new jars. This meant that we reset the jars' headspace gas concentrations. The initial headspace concentrations were measured each time the headspace was reset. These measurements were used along with the measurements at the sacrificial time points to calculate the cumulative headspace gas concentrations, whose determination method is described below in section *2.2.1.4*, that would have built up in the jars' headspace if not for the need to transfer the soil to different jars when jars were broken. None of the toluene-amended soil treatments had their headspace reset (*i.e.*, none were transferred to new jars). In total, 38 jars were broken and replaced during the experiment.

Triplicate jars of each treatment were sacrificially sampled for gas and porewater analyses at the end of each 2-week freeze-cycle (-10°C) and 2-week thaw-cycle (15°C). The temperature regime with freezing and thawing cycle (FTC) for 215 days of the batch experiment is illustrated in Figure 2-2b. In total, sacrificial sampling occurred for a total of 6 time points in the no toluene-added treatments (NL-NT, LA-NT, and BES-NT), and 3 time points in the toluene-amended treatments (NL-TA, LA-TA, BES-TA).

2.2.1.4 Headspace CO_2 and CH_4 gas analyses

During sampling, jars were transferred to an anaerobic chamber, and gas samples were collected from each jar's headspace using a plastic 50 mL syringe in an anaerobic chamber and analyzed for CH_4, CO_2, and H_2 using a Shimadzu Gas Chromatograph (Model GC-2014) equipped with a flame ionization detector, a methanizer (for CO_2 and CH_4), electron capture detector (for N_2O), and thermal conductivity detector (for O_2).

2.2.1.5 Headspace CO_2 and CH_4 isotope analyses

Headspace gas samples were also analysed for $\delta^{13}C$-CO_2 and $\delta^{13}C$-CH_4 isotope compositions using plastic gas-tight syringes and needle inserted through the Teflon or rubber septa in the jar lid. Gas samples were preserved by injecting 1-10 mL of headspace gas into helium-flushed Exetainer vials. The collected headspace gas samples were analysed for $\delta^{13}C$-CO_2 and $\delta^{13}C$-CH_4 in the Environmental Isotope Laboratory at the University of Waterloo using gas chromatography combustion (GCC) conversion through an Agilent 7890A gas chromatograph coupled to a Thermo Scientific Delta V Plus isotope ratio mass spectrometer via GC Isolink (Thermo Fisher Scientific, Germany) continuous flow isotope ratio mass spectrometer (CFIRMS). Samples were pre-concentrated using a Thermo Scientific PreCon Automated Trace Gas Pre-Concentrator (Thermo Fisher Scientific, Germany).

The fractionation factor between CO_2 and CH_4, α_{CO_2/CH_4} was calculated to quantitatively interpret the isotope results and use the data as an independent tool for quantifying the different contributions of the two methanogenic pathways (hydrogen-based and acetate-based, HBM and ABM) in the experiment. α_{CO_2/CH_4} was calculated according to Eq. 2-1:

$$\alpha_{CO_2/CH_4} = \frac{\delta^{13}C - CO_2 + 1}{\delta^{13}C - CH_4 + 1} \tag{2-1}$$

where $\delta^{13}C - CO_2$ and $\delta^{13}C - CH_4$ were in decimal units (*i.e.*, -0.001 instead of -1 ‰).

The two major methane producing pathways, and the only methanogenic pathways included in our microbial reaction network model (described in section *2.3.1*), acetate-based methanogenesis (ABM) and hydrogen-based methanogenesis (HBM) have distinct values of α_{CO_2/CH_4}: the value for ABM ranges between 1.017 and 1.027 (Chan *et al.*, 2005; Okumura *et al.*, 2016), while the value of HBM ranges between 1.068 and 1.087 (Penning *et al.*, 2006; Vavilin *et al.*, 2018). Hence,

the observed α_{CO_2/CH_4} can be used to calculate the fractions of ABM and HBM occurring in the system. The ABM fraction (f_{ABM}) was calculated using Eq. 2-2:

$$f_{ABM} = \frac{\alpha_{obs} - \alpha_{HBM}}{\alpha_{ABM} - \alpha_{HBM}} \tag{2-2}$$

where α_{obs} is the α_{CO_2/CH_4} value observed during the experiment, α_{HBM} is 1.078, the average value of the α_{CO_2/CH_4} values reported for HBM, and α_{ABM} is 1.022, the average value of the α_{CO_2/CH_4} values reported for ABM. We also estimated upper and lower bounds for the f_{ABM} estimated using the upper and lower bounds on the ranges of α_{ABM} and α_{HBM}. Given the f_{ABM} calculated, the fraction of HBM could then be calculated given that f_{HBM} = 1- f_{ABM}.

2.2.1.6 Porewater chemistry

On sacrificial sampling dates, once headspace gas samples were collected, jars were opened in the anaerobic chamber to collect porewater samples for various analyses. Approximately 50 mL of overlying water and porewater were collected from each jar and filtered through a 0.45 µm pore size membrane filter (nylon membrane syringe filters, VWR Scientific). The pH of the unfiltered porewater samples was measured using a gell-filled pH electrode (Orion™ Economy Series pH Combination Electrode, ThermoScientific). Approximately 1 mL of porewater was filtered through a 0.2 µm pore size membrane filter (Polyethersulfone membrane syringe filters, Thermo Scientific) and frozen at -20°C for later analysis of major anion concentrations including nitrate (NO_3^-), sulfate (SO_4^{2-}), acetate ($C_2H_3O_2^-$) and lactate ($C_3H_6O_3$) using ion chromatography (IC, Dionex ICS-5000 with a capillary IonPac® AS18 column; MDL: 14.7, 6.7, 0.7, and 0.4 µmol L^{-1}, respectively). Concentrations of dissolved organic carbon (DOC), total dissolved nitrogen (TDN), and dissolved inorganic carbon (DIC) in filtered porewater samples were measured using a total organic carbon analyzer (Shimadzu TOC-LCPH/CPN; MDL: 4.6, 2.9, and 2.8 µmol L^{-1}, respectively). For jars amended with toluene, compound-specific $\delta^{13}C$- and $\delta^{2}H$- toluene isotope compositions were determined in the Environmental Isotope Laboratory of the University of Waterloo using a PT-GC- IRMS system. The PT-GC-IRMS system consisted of CDS 7000E/7300/7400/7500, Purge and Trap/Thermal Desorption System (CDS Analytical, Oxford, PA, USA), a Trace GC (Thermo Fisher Scientific, Bremen, Germany), a GC –Combustion III

interface operating at 950°C/1450°C for $\delta^{13}C/\delta^{2}H$ and a Delta plus XP isotope ratio mass spectrometer (Thermo Fisher Scientific, Bremen, Germany).

To evaluate whether there were any changes in DOC composition over the course of the experiment, specific UV absorbance at 254 nm ($SUVA_{254}$) was analyzed by measuring the absorbance at 254 nm of 0.45 µm filtered porewater on a UV-Visible spectrophotometer (Evolution™ 260 Bio UV-Visible Spectrophotometer, Thermo Scientific) after the method first described by Weishaar *et al.* (2003). The UV absorbance measured at 254 nm was then divided by the DOC concentration (in units of mg C L^{-1}), giving units of L mg C^{-1} m^{-1}.

2.2.2 Numerical simulation

2.2.2.1 Governing equations

The mass conservation for one or more chemical species are expressed by the following equation when there are chemical reactions and the prevailing transport mechanism is diffusion:

$$\frac{\partial c_i}{\partial t} + \nabla \cdot J_{d,i} = R_i \tag{2-3}$$

where C_i is the concentration [ML^{-3}] of the specimen i, R_i is reaction rate [$ML^{-3}sec^{-1}$] of substance i, and $J_{d,i}$ is the diffusive flux tensor for each substance and defined by:

$$J_{d,i} = -D_{e,i}\nabla C_i \tag{2-4}$$

where $D_{e,i}$ denotes the effective diffusion coefficient [L^2 sec^{-1}] for substance i in an isotropic diffusion modeling. In a saturated porous medium with the presence of chemical reaction and adsorption process, the Eqs. 2-3 and 2-4 are replaced by the following macroscopic reactive transport equation with no convective transport mechanism:

$$\frac{\partial(\phi_e C_i)}{\partial t} - D_{e,i}\nabla C_i + \frac{\partial\left(\rho_b c_{p,i}\right)}{\partial t} = R_i \tag{2-5}$$

where ϕ_e is effective porosity, ρ_b is bulk density of soil, and $c_{p,i}$ is the Langmuir adsorption isotherm for substance i. $D_{e,i}$ can be correlated to solute diffusivity in bulk solvent, $D_{L,i}$, as (Millington and Quirk, 1961):

$$D_{e,i} = \frac{\theta_l^{-\frac{10}{3}}}{\phi_e^2} D_{L,i} \tag{2-6}$$

where θ_l is the soil water content, which is a function of temperature under saturated conditions as follows (Huang and Rudolph, 2021; Tice *et al.*, 1976) :

$$\theta_l = \begin{cases} \phi_e & T > T_f \\ \phi_e \left[1 - \left(T - T_f\right)^{\alpha}\right] & T \leq T_f \end{cases} \tag{2-7}$$

The third term in Eq. 2-5 models the adsorption/desorption of each chemical species to the solid phase (*i.e.*, the soil matrix) in porous media which accounts for decreasing and increasing in chemical transport flux of species as they attach to (adsorb) and detach from (desorb) the solid phase during traveling through the medium. In this study, Langmuir adsorption model is used to predict the solid concentration ($c_{p,i}$) from the concentration in the liquid phase as:

$$c_{p,i} = c_{pmax,i} \frac{K_{L,i} C_i}{1 + K_{L,i}} \tag{2-8}$$

where $c_{pmax,i}$ is the maximum adsorption capacity and $K_{L,i}$ is the Langmuir constant for substance i. The final term in Eq. 2-5, R_i, represents chemical reactions, most of which are microbially-catalyzed, that account for changes in species concentration per unit volume porous medium per time. In the presence of a network of different reactions, R_i can be defined by:

$$R_i = \sum_j \nu_{i,j} r_j \tag{2-9}$$

where r_j is the rate of jth reaction in a reaction network, and $\nu_{i,j}$ is the stoichiometric coefficient of specimen i in the reaction j. Then the r_j can be calculated using the biomass-implicit formulation for representing microbial reaction rates (Smeaton and Van Cappellen, 2018):

$$r_j = -r_{max,i} \frac{C_{EA}}{K_{EA} + C_{EA}} \frac{C_{ED}}{K_{ED} + C_{ED}} f_{temp} f_{pH} \tag{2-10}$$

where $r_{max,j}$ is the maximum rate constant for reaction j, C_{ED} and C_{EA} are concentrations of electron donors and electron acceptors consumed in the reaction, respectively, both in [M], K_{ED} and K_{EA} are the half saturation constants for the electron donors and electron acceptor, respectively, both in [M], and f_{temp} and f_{pH} are functions representing the temperature (T) and pH dependency of the reactions as follows (Jin and Kirk, 2018; Rosso *et al.,* 1993) :

$$f_{temp} = \frac{(T - T_{max})(T - T_{min})^2}{(T_{opt} - T_{min})[(T_{opt} - T_{min})(T - T_{opt}) - (T_{opt} - T_{max})(T_{opt} + T_{min} - 2T)]} \tag{2-11}$$

where T_{min}, T_{max}, and T_{opt} are the minimum, maximum and optimum temperature values for each reaction, respectively, in units of [°C].

$$f_{pH} = \begin{cases} \dfrac{pH_{opt} - pH}{pH_{opt} - pH_{min}} \ (\text{pH} \leq pH_{opt}) \\ \dfrac{pH_{max} - pH}{pH_{max} - pH_{opt}} (\text{pH} > pH_{opt}) \end{cases} \tag{2-12}$$

where pH_{min} , pH_{max} , and pH_{opt} are minimum, maximum, and optimum values of pH, respectively.

It should be noted that some chemical species act as competitive inhibitors to some reactions who share a substrate, so we incorporated an inhibition term in Eq. 2-10 for the inhibiting effect of sulfate (SO_4^{2-}) on the reactions LF, TF, ABM, HBM, ACET (reactions associated with these reaction short forms are provided in Table 2-1):

$$r_{inh,j} = \frac{K_{inh,i,j}}{K_{inh,i,j} + c_i} \tag{2-13}$$

where $K_{inh,i,j}$ is the inhibition constant for substance i in reaction j and $r_{inh,j}$ is the inhibition factor. Eq. 2-13 was also used to simulate thermodynamic inhibition (*i.e.*, noncompetitive inhibition) of some reactions by the buildup of reaction products (Costello *et al.*, 1991; Mosey,

1983; Siegrist *et al.*, 1993). HBM and ABM were inhibited by CH_4 buildup, MF was inhibited by H_2 buildup, and ACET was inhibited by acetate buildup, giving inhibition constants ($K_{inh,i,j}$) fitting to the experimental data for CH_4, H_2 and acetate (Table 2-3).

Table 2-1: List of reactions included in the microbial reaction network and their reaction rate constants, half saturation constant, and other parameters.

Reaction name	Reaction name shortform	Chemical reaction	Reaction parameters		
			Rate constant, $r_{max,i}$ ($\frac{mol}{m^3.sec}$)	Half saturation constant, K_{ED} ($\frac{mol}{m^3}$)	Half saturation constant, K_{EA} ($\frac{mol}{m^3}$)
Lactate oxidation, sulfate reduction	LOSR	$C_3H_5O_3^- + 0.5SO_4^{2-} \rightarrow C_2H_3O_2^- + HCO_3^- + 0.5HS^- + 0.5H^+$	8.3e-8	0.005	0.025
Lactate fermentation	LF	$C_3H_5O_3^- \rightarrow 1.5\ C_2H_3O_2^- + 0.5H^+$	1.1e-7	0.005	NA
Hydrogen oxidation, sulfate reduction	HOSR	$H_2 + 0.25SO_4^{2-} + .25H^+ \rightarrow 0.25HS^- + H_2O$	4.4e-8	0.001	0.025
DOC (represented by glucose) oxidation, sulfate reduction	DOSR	$C_6H_{12}O_6 + 3SO_4^{2-} \rightarrow 6HCO_3^- + 3HS^- + 3H^+$	4.2e-7	0.004	0.025
DOC (represented by glucose) fermentation	DF	$C_6H_{12}O_6 + 1.714H_2O \rightarrow 0.857\ HCO_3^- + 2.57C_2H_3O_2^- + 1.714H_2 + 3.433\ H^+$	1.6e-6	0.004	NA
Toluene fermentation	TF	$C_7H_8 + 21H_2O \rightarrow 7\ HCO_3^- + 18H_2 + 7H^+$	4.4e-8	0.04	NA
Acetogenesis	ACET	$0.5HCO_3^- + H_2 + .25H^+ \rightarrow 0.25\ C_2H_3O_2^- + H_2O$	8.8e-7	0.001	0.003
Acetate oxidation, sulfate reduction	AOSR	$C_2H_3O_2^- + SO_4^{2-} \rightarrow 2\ HCO_3^- + HS^-$	4.9e-8	0.004	0.025
Acetate-based methanogenesis	ABM	$C_2H_3O_2^- + H_2O \rightarrow HCO_3^- + CH_4$	1.2e-8	0.004	NA

Hydrogen-based methanogenesis-Methane fermentation	HBM MF	$0.25HCO_3^- + H_2 + .25H^+ \rightleftharpoons 0.25CH_4 + 0.75\ H_2O$	2.7e-8 2.9e-8	0.001 0.003	0.003
Non-microbial reactions					
Carbonate equilibrium	CE	$CO_2(aq) + H_2O \rightleftharpoons HCO_3^- + H^+$	$K_{eq} = 10^{-\left[\frac{782.33}{T}+0.0148T-0.73\right]}$		NA
Soil matrix organic carbon release of glucose-DOC	SMOCR	Microbial Biomass C→ $C_6H_{12}O_6$	4.2e-7 (sec^{-1})		NA

Table 2-2: Initial concentrations of each species modeled in the microbial reaction network.

Substance	Initial concentration (mol m^{-3}) in NL treatment	Initial concentration (mol m^{-3}) in LA treatment	Initial concentration (mol m^{-3}) in BES treatment
SO_4^{2-}	0.384	0.350	0.363
HCO_3^-	4.420	4.820	5.007
$C_3H_5O_3^-$	0.086	0.384	0.22
$C_2H_3O_2^-$	0.298	0.465	0.355
$C_6H_{12}O_6$	2.040	3.278	3.039
DOC	12.22	19.67	18.23
DIC	4.42	4.82	5.007
CO_2 (aq)	0.040	0.090	0.084
H_2 (aq)	0		
CH_4 (aq)	0		
C_7H_8	0.155 (at day 113 in TA)		
CO_2 (g), CH_4 (g), H_2 (g)	0		
Soil matrix organic C	1.97 mmol		

Table 2-3: Parameters of flow and reactive transport processes used in the numerical simulations.

Parameters	Values
$T_{min}, T_{opt}, T_{max}$ (K)	263.15, 303.15, 313.15
ϕ_e	0.35

pH_{min}, pH_{opt}, pH_{max}	4.9, 7, 8.9
$c_{pmax,Tol}$ (mol kg^{-1})	20.59
$K_{L,Tol}$(m^3 mol^{-1})	1.872
ρ_b (kg m^{-3})	1220
$K_{H_2}^H$	0.018
$K_{CH_4}^H$	0.034
K_{Tol}^H	0.277
$K_{CO_2}^H$	0.83
D_{Tol}^g	8.7e-6 (m^2 sec^{-1})
D_{Tol}^{aq}	5.6e-10
$D_{CH_4}^g$	1.9e-5
$D_{CH_4}^{aq}$	1.6e-9
$D_{CO_2}^g$	1.1e-5
$D_{CO_2}^{aq}$	1.2e-9
$D_{H_2}^g$	7.5e-5
$D_{H_2}^{aq}$	2.7e-9
D_{Sulf}	6.8e-10
D_{Lac}	6.4e-10
D_{Acet}	6.8e-10
D_{Gluc}	6.14e-10
D_{Bic}	9.2e-10
K_{inh,SO_4}(mol m^{-3})	0.001
$K_{inh,Acet}$(mol m^{-3})	7.25
K_{inh,H_2}(mol m^{-3})	0.0001
K_{inh,CH_4}(mol m^{-3})	0.0004

2.2.2.2 Modeling procedure

The physical model of the soil batch experiment jars is comprised of two cylindrical components (Figure 2-2a). The lower section of the cylinder represents the saturated soil and the upper cylinder represents the headspace. As shown in Figure 2-2a, a zero-concentration gradient ($-n \cdot J_i = 0$) is considered for the upper boundary in the model. Henry's law can be applied to the boundary between the two soil and headspace components of the model as:

$$c_i^{aq} = k_i^h c_g \tag{2-14}$$

where c_i^{aq} and c_g are equilibrium concentrations of substance i in aqueous phase and headspace and k_i^h is the dimensionless Henry's constant of substance i, which is a function of temperature. To investigate the impact of the temperature fluctuations (Figure 2-2b) on biodegradation processes and gas production, a microbial reaction network of 11 microbially-catalyzed chemical reactions is implemented in the numerical simulations. The list of reactions in the reaction network and their reaction rate constants fitted by the model are presented in Table 2-1. The initial concentrations of each chemical simulated in the reaction network are provided in Table 2-2. The parameters of flow and reactive transport processes used in numerical simulations are provided in Table 2-3.

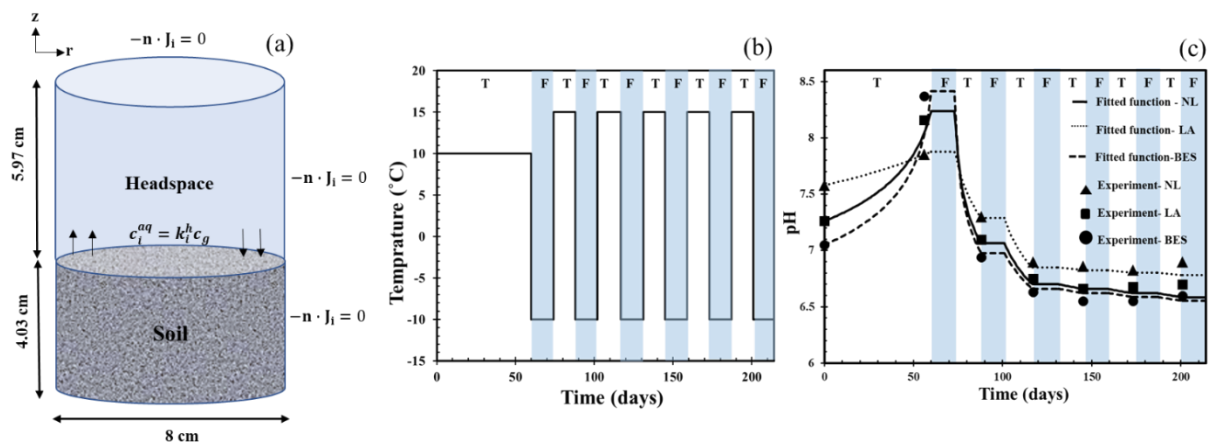

Figure 2-2: (a) Image of three-dimensional model used to simulate the batch experiment composed of saturated soil with porewater and headspace gas zones, (b) temperature fluctuations imposed during 215 days of experiment with freeze (F, at -10°C) and thaw (T, at 15°C) cycles, and (c) pH values measured from the experiment used in the numerical simulation to calculate the pH function.

Two of the reactions provided in Table 2-1 are not microbially-catalyzed reactions and their rates were not modelled using Eq. 2-10: carbonate/bicarbonate equilibrium as a function of pH and "glucose-DOC" production by freezing-induced soil matrix disturbance. The carbonate/bicarbonate equilibrium was modelled as an equilibrium reaction using the equilibrium constant for the dissolved carbon dioxide/bicarbonate system. The glucose-DOC production rate by freezing-induced soil matrix disturbance lysis is represented using a first-order rate where the

rate depends on the concentration of soil organic carbon. We added this DOC production reaction to fit the evolution of total DOC observed in the experiment and based on studies by others which show that freezing causes rapid physical conversion of soil C to DOC (Fuss *et al.*, 2016; Kværnø and Øygarden, 2006). We simulated the reactions that consume this produced DOC by using the chemical formula of glucose to assign reaction stoichiometries to the reactions. The experimental glucose-DOC was calculated as the difference between the measured total DOC and acetate in carbon moles. Given the challenges in modeling pH as a variable that the model simulates (Hofmann *et al.*, 2008; Jourabchi *et al.*, 2005), we imposed the pH values measured during the experiment in the numerical simulation. We fit a continuous function to the discrete experimental pH measurements to impose the pH at any time in the model simulation (Figure 2-2c).

In the numerical simulations used in this study, the transport, adsorption, and biodegradation of species in the soil domain are evaluated by solving Eq. 2-5 alongside corresponding boundary and initial conditions presented in Figure 2-2a and Table 2-2. The reaction rates and solid concentration in the adsorption/reaction term of Eq. 2-5 are evaluated by Eqs. 2-6 and 2-7, respectively. In the headspace, the transport of gaseous species is incorporated by solving Eq. 2-3 with the boundary conditions illustrated in Figure 2-2a. Zero concentrations are set for initial concentration of species in the headspace. Finally, interaction between two domains (soil and headspace) is modeled using Eq. 2-14. These sets of equations are solved using the COMSOL Multiphysics® software (version 5.6) by adopting a 2D axisymmetric geometry.

The simulations were performed for the 6 different experimental treatments: NL-NT, LA-NT, BES-NT, NL-TA, LA-TA, and BES-TA treatments. In addition, we used the model with the parameters that were fit to the experimental data to simulate a no FTC scenario and to compare the effects of FTCs versus no FTCs on CH_4 and CO_2 generation and toluene biodegradation.

2.3 Results

In what follows, we report and discuss the results obtained from the batch experiments and numerical simulations for the 6 different treatments (NL-NT, NL-TA, LA-NT, LA-TA, BES-NT, and BES-TA) which were subjected to 5 consecutive FTCs with the temperature regime presented in Figure 2-2b. We show the time series trends in concentrations measured and simulated (Figures 2-3 to 2-6) and the time series trends in the reaction rates simulated (Figure 2-8). In addition, we present the simulation results of a no FTC scenario (Figure 2-7) in section *3.4*. The microbial

reaction network, initial values, and reaction parameters fitted to the data and applied in the numerical simulations are presented in Figure 2-2 and Tables 2-1 to 2-3. These parameters were applied for all simulation runs.

2.3.1 Porewater chemistry: pH, DIC and, SO_4^{2-}

The pH increased from around 7 to around 8.3 in all three treatments (NL-NT, LA-NT, BES-NT) before the first freeze period. Following the first freezing period, pH decreased by more than 1 pH unit in the treatments, and then decreased by close to 0.5 after the second FTC. Thereafter, for the remaining FTCs, the pH decreased by around 0.1 or less after each FTC, and was around 6.6-6.8 in all three treatments by the end of the experiment on day 202. As mentioned in section *2.3.2*, these measured pH values were then imposed in the model simulations, rather than being treated as a variable to simulate.

The change in DIC concentrations closely matched the change in pH values (Figures A1-1 and 2-2c), which is unsurprising, as the governing carbonate equilibria equations used in the model (Table 2-1) account for the decrease in DIC at low pH whereby dissolved CO_2 decreases due to loss as gaseous CO_2 in the headspace and decrease in CO_2 production rate as a result of electron donors depletion. DIC and pH increased during the first 60 days, dropped sharply after the first and second freezing periods, and then remained relatively constant for the remainder of the experiment. DIC concentrations in the TA treatments (BES-TA, LA-TA, NL-TA) are higher than in the NT treatments because the added toluene increased the total carbon pool in the system, stimulates toluene fermentation (reaction TF), and the acetate produced by TF ultimately increases the cumulative gaseous CO_2 and DIC produced by ABM (Figures 2-3 and 2-4). The model simulations are able to closely match these DIC changes, confirming that the model accurately represents the carbonate equilibrium system and the influence of pH on DIC speciation, as well as the reactions that produce and consume DIC (*e.g.*, ABM, TF, HBM).

SO_4^{2-} was the only electron acceptor that was available in the soils under the imposed anoxic conditions, as nitrate concentrations were very low or not detected. SO_4^{2-} was completely consumed in both the BES and LA treatments by the end of the second thaw period (Figures A1-2) and in the NL treatment by the end of the third thaw period due to the absence of lactate addition, and hence the lower amount of electron donor available to reduce the SO_4^{2-}. It should be noted that

lactate (data not shown) was no longer detected and presumed to be completely consumed in all treatments by day 35 (lactate oxidation rates are shown in Figure A1-2).

2.3.2 Porewater chemistry: DOC and acetate

DOC concentrations decreased prior to the FTCs, in all the treatments (Figure 2-3a) because the DOC was consumed by fermentation (DF) (Figures 2-3a and 2-8) and sulfate reduction (DOSR) reactions (Figure A1-2). Upon the initiation of the FTCs, DOC progressively increased with each FTC because of two reactions: (1) the freezing-induced soil matrix organic carbon release (SMOCR) reaction which is assumed to produce DOC during the freezing periods, and (2) acetogenesis (ACET), which produces acetate from H_2 and CO_2 during the thawing periods (Figure 2-8). The DOC and acetate concentrations plateau in the fourth thaw period because the soil organic carbon DOC release and acetogenesis reaction rates decrease over time in the experiment. The DOC and acetate concentrations are higher in the LA and BES treatments relative to the NL treatments (Figures 2-3b, 2-3c, and 2-8), and are higher in the TA treatments relative to the NT treatments (Figures 2-3a to 2-3c) because of the added carbon in the form of lactate and toluene, respectively. In the model, the reactions driving this transformation of added lactate and toluene to increased acetate concentrations are lactate and toluene fermentation (LF and TF), respectively, which produce H_2. The H_2 produced by these reactions then stimulates acetogenesis.

In initial iterations of the model development, acetogenesis could not explain the FTC-driven rise in total DOC concentrations alone, and we therefore attributed the increase in non-acetate DOC to freezing-induced soil organic carbon release from the soil matrix (*e.g.*, soil aggregates) and/or microbial biomass, as described in section *2.2*. In addition to the carbon balance accounted for by the model, we measured the $SUVA_{254}$ index of the DOC in the porewater. Figures 2-3(g-i) show a considerable decrease in the $SUVA_{254}$ index after each freezing period. The decrease in the $SUVA_{254}$ index following each freezing period for all the soils, regardless of the treatment, indicates a release of soil matrix organic carbon, as microbial dissolved organic matter has a relatively low $SUVA_{254}$ index (McKnight *et al.*, 1994; Vestgarden and Austnes, 2009).

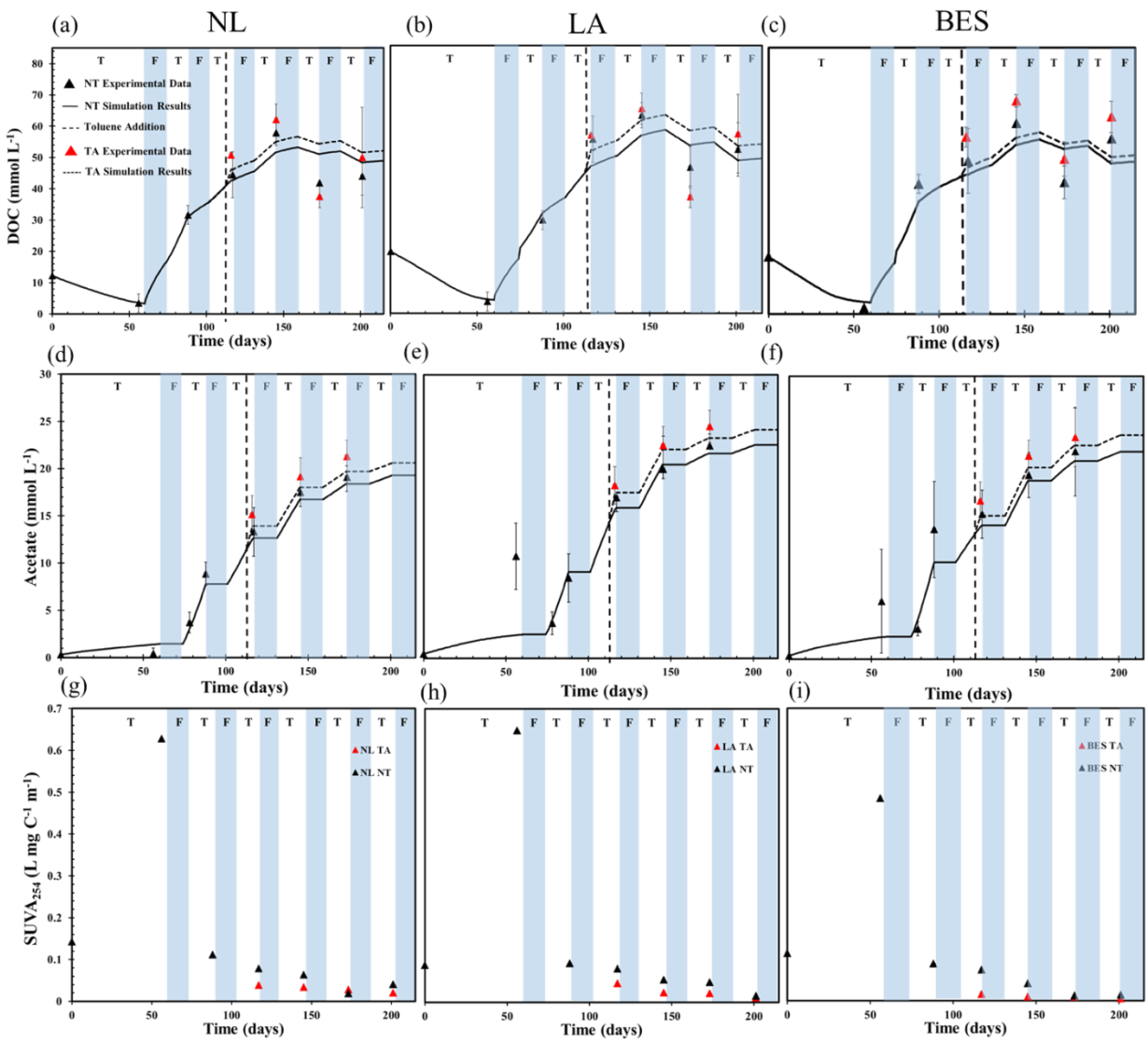

Figure 2-3: Timeseries results of DOC (a-c), Acetate (d-f), and $SUVA_{254}$ index (g-i) for soils with different treatments during 215 days of experiment with freeze (F, at -10°C) and thaw (T, at 15°C) cycles (NL: no lactate added soils, LA: lactate amended treatment, BES: 2-bromoethanesulfonate amended treatment, NT: no toluene added soils, TA: toluene amended treatment).

2.3.3 CO_2 and CH_4 generation

The CO_2 and CH_4 headspace concentrations increase over time across all the treatments, with negligible changes in concentration during the freezing periods (Figures 2-4 and 2-8). Given that we calculated the cumulative CO_2 and CH_4 concentrations for the closed batch systems, these cumulative concentrations also represent the cumulative CO_2 and CH_4 production. The constant

concentrations during the freezing periods are successfully simulated by imposing near-zero rates of the reactions that produce CO_2 and CH_4 during these freezing periods (Figures 2-4 and 2-8). The results of simulation and experiment show the rapid increase in CO_2 and CH_4 production rates after thaw (*i.e.,* when the temperature rapidly switches from -10˚C to 15˚C) because of the accumulation of H_2, CO_2, and acetate (Figures 2-4 and 2-8). The simulated CO_2 and CH_4 production rates after the fourth freezing period are lower than that in the other prior thawing periods as shown in Figure 2-4. This decrease in the net CO_2 and CH_4 production rates is simulated in the model by the lower rates of HBM relative to the earlier thawing phases (Figures 2-5 and 2-8) because of the lower concentrations of H_2 and HCO_3^- (*i.e.,* DIC), and even by the predicted consumption of CH_4 by methane fermentation (MF, which is the reverse reaction of HBM).

Another reason for the decreased CO_2 and CH_4 production rates could be that ABM is inhibited. ABM inhibition has been observed before, and is sometimes attributed to high acetate concentrations being thermodynamically inhibiting (Garg *et al.*, 2017; Nozhevnikova *et al.*, 2007). However, we calculated the Gibbs energies under non-standard state conditions of ABM and found that it was thermodynamically favourable throughout the experiment (Table A1). Toluene addition to the incubations on day 113 increased CO_2 and CH_4 concentrations in all three treatments relative to the NT incubations as shown in Figure 2-4. The cumulative CO_2 and CH_4 generation increased by 136% and 87%, respectively, in the NL-TA treatment (Figures 2-4a and 2-4d), by 117% and 61% in the LA-TA treatment (Figures 2-4b and 2-4e), and by 50% and 33% in the BES-TA treatment (Figures 2-4c and 2-4e), relative to their respective NT treatments.

The NL treatments (NL-NT and NL-TA) had lower cumulative CO_2 and CH_4 concentrations compared to the LA treatments (LA-NT and LA-TA) because of the additional carbon (*i.e.,* lactate) present in the LA incubations as illustrated in Figures 2-4 and 2-8. The BES treatments (BES-NT and BES-TA) had the lowest cumulative CO_2 and CH_4 concentrations despite the addition of lactate to these treatments due to the inhibition of methanogenic pathways by BES (Figures 2-4c, 2-4e, and 2-8f). This inhibition effect on methanogenesis reactions by BES was simulated in the model by adding an additional inhibition factor on top of the inhibition effect by non-zero sulfate concentrations simulated using Eq. 2-13. The best match with the experimental CO_2 and CH_4 concentration data was produced during the first 60 days when BES was assumed to slow down

ABM and HBM by 90% and 50%, respectively. After the first freezing period, the inhibition effect of BES was considerably lower, and the best fitting inhibition factor was 25% for both ABM and HBM (Figures 2-4, 2-5, and 2-8). We attribute the lowered inhibition effect after the first freezing period to BES degradation by microbial degradation or by degradation due to the freezing and thawing. These simulation results on the efficacy of BES as a methanogenesis inhibitor are in agreement with other experimental studies in the literature which also found that BES was not always 100% effective at inhibiting ABM and HBM and found that the inhibition effect of BES declined with time as BES was degraded (Scholten *et al.*, 2000; Zinder *et al.*, 1984).

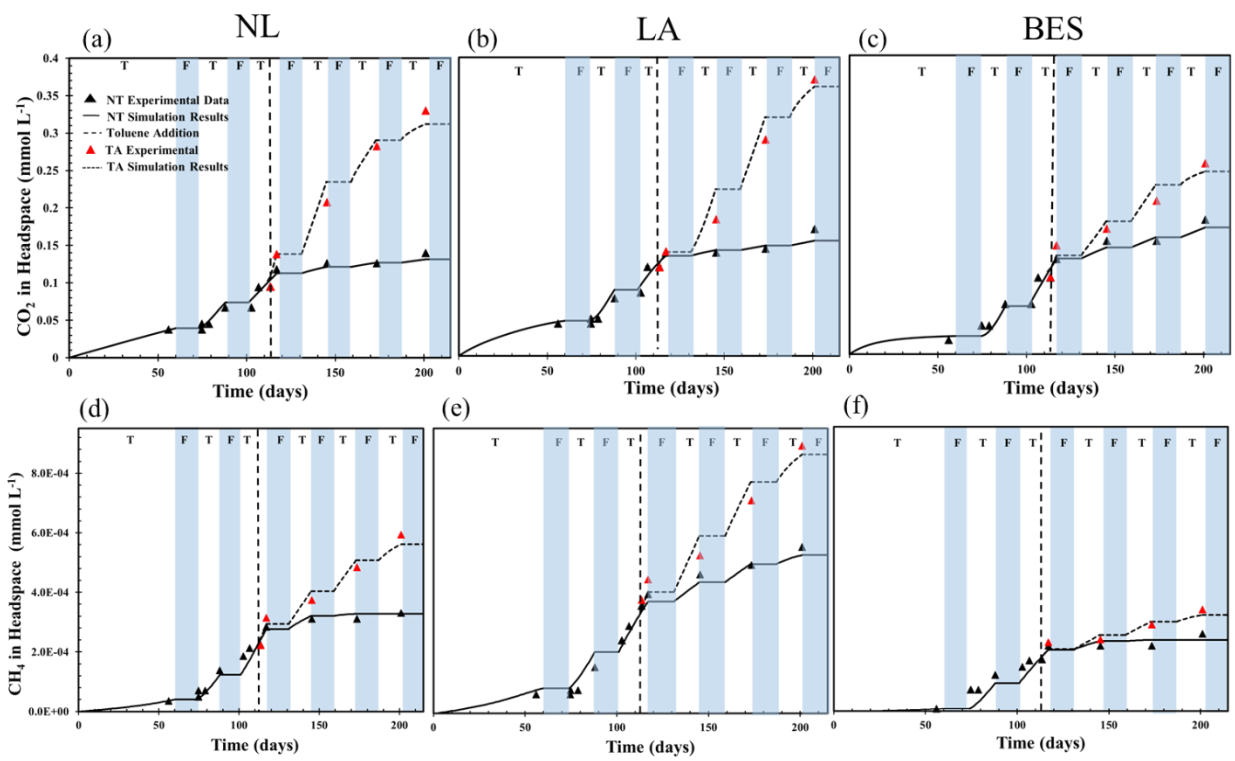

Figure 2-4: Headspace CO_2 concentrations (a-c) and headspace CH_4 concentrations (d-f) in soils with different treatments during 215 days of experiment with freeze (F, at -10°C) and thaw (T, at 15°C) cycles.

2.3.4 Fraction of ABM estimated from α_{CO_2/CH_4} and simulated by model

The fraction of ABM predicted by the model and calculated using the headspace isotope $\delta^{13}C$-CH_4 and $\delta^{13}C$-CO_2 (Figure 2-5) shows that in all three of the NT treatments (NL-NT, LA-NT, BES-NT), α_{CO_2/CH_4} decreases from around 1.05 to around 1.02 between day 145 and 202 (Figure A1-3c), which corresponds to an increase in the proportion of ABM contributing to methane

production from around 0.5 to 0.85. In TA treatments, the average α_{CO_2/CH_4} is higher than that in NT treatments, which corresponds to a moderate increase in the HBM fraction because of increase in the concentrations of H_2 and HCO_3^-. Overall, the model-calculated relative rates of ABM and HBM are generally in agreement with the ABM fraction derived from the α_{CO_2/CH_4} results.

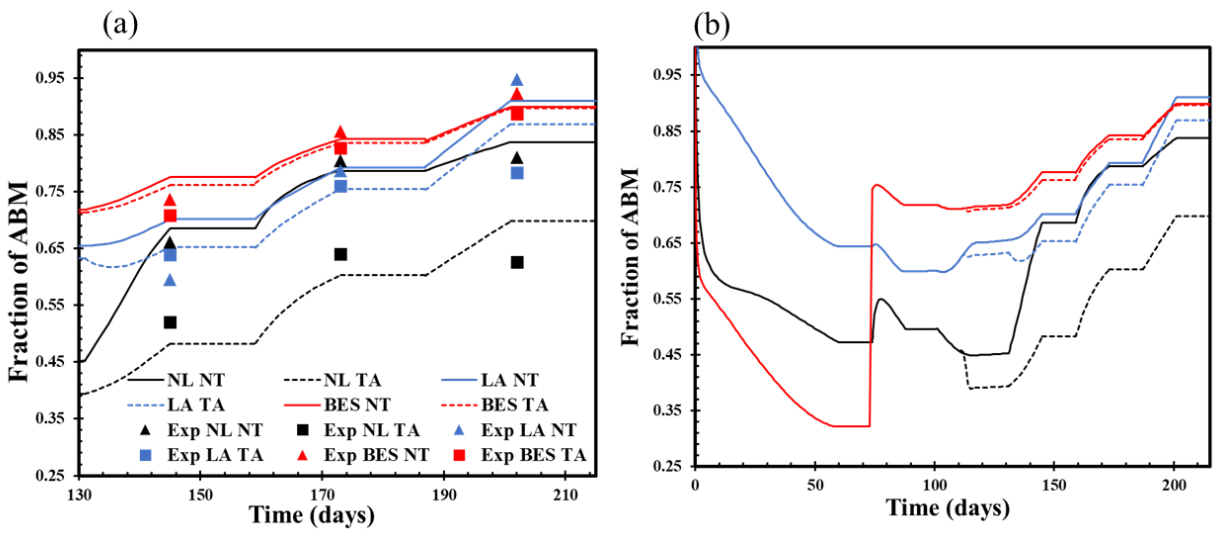

Figure 2-5: (a) Experimental and simulation results of the fraction of methane produced by ABM in soils with different treatments between day 130 and 215, and (b) simulation results of the fraction of ABM in soils with different treatments during 215 days.

2.3.5 Toluene concentrations and δ^{13}C-toluene

Natural attenuation of toluene can be attributed to 1) anaerobic biodegradation; 2) evaporation; and 3) sorption in anoxic, saturated soil. For this reason, all three of these processes are considered in the model. When toluene was added to soil at day 113, the toluene concentration declined sharply between day 113 and 117 (Figure 2-6a). The model predicts that this sharp decline is due to toluene sorption to the soil. The model predicts that after day 117, after the initial toluene attenuation by sorption to the soil, TF is the dominant toluene-consuming reaction. Overall, the model predicts that 74% of the cumulative toluene concentration decrease between days 113 and 202 is due to biodegradation, 15% being attributed to evaporation, and 11% being attributed to sorption. Like all the other microbial reactions, the TF reaction has a near-zero reaction rate during the freezing periods, and thus, no toluene biodegradation is occurring during these periods (Figure

2-8). During the thawing periods, toluene biodegradation via the TF reaction was the dominant toluene attenuation mechanism.

Overall, both the experimental results and model simulations show that toluene is anaerobically biodegraded. In addition, the δ^{13}C-toluene time series trend confirms that toluene was being biodegraded once it was added to the soil batch experiments on day 113. The δ^{13}C-toluene becomes less negative with time, increasing from -28.2 ‰ initially to -27 ‰ by the end of the experiment, which is indicative of microbial biodegradation (Figure 2-6b).

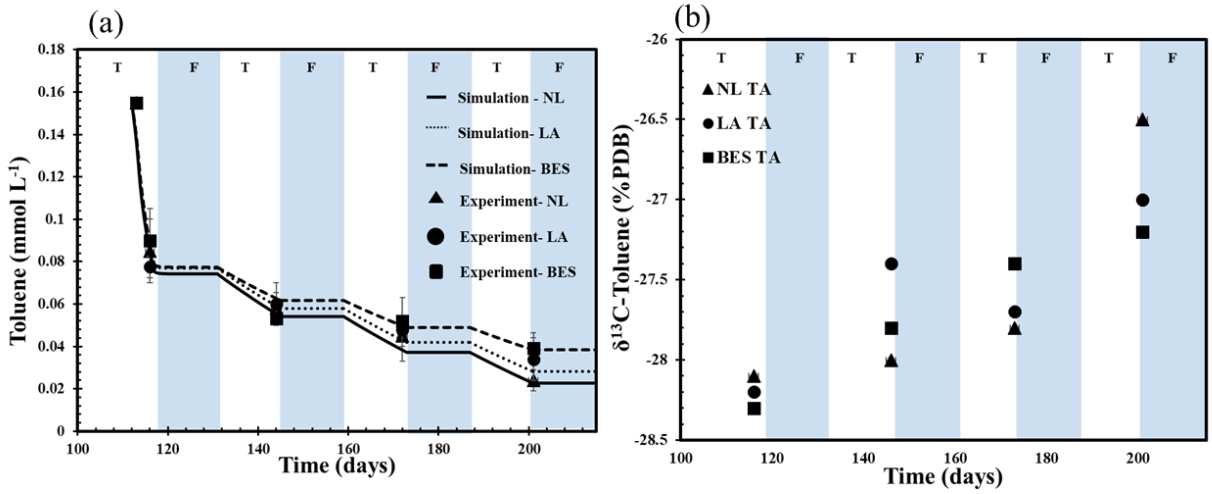

Figure 2-6: Timeseries results for (a) Toluene concentration in NL, LA, and BES soils, and (b) δ^{13}C-toluene in TA soils with NL, LA, and BES treatments during 215 days of experiment with freeze (F, at -10°C) and thaw (T, at 15°C) cycles.

2.3.6 Microbial reaction network: simulated reaction rates

To simulate methanogenic toluene degradation, a network of 13 microbially-mediated reactions were considered, and rate constants and half saturation constants are used as fitting parameters as shown in Table 2-1. Figures 2-8 a-c show the rates of DF, ACET, and SMOCR in the different treatments. The rate of SMOCR decreases over time because of depletion of the leachable soil organic matter pool, while the rates of DF and ACET increase when H_2 and glucose are accumulated in the system. The rates of HBM, ABM, AF, and MF are illustrated in Figures 2-8 d-f. ABM, AF, and MF reactions become the dominant reactions under anoxic, electron-acceptor limited environment, but the rate of HBM decreases when H_2 is consumed or released into the

headspace. The rates of the other reactions are illustrated in Figures A1-2. As shown in these figures, the role of sulfate reduction reactions in biodegradation of DOC becomes less important over time when sulfate is sufficiently depleted in the system.

The fraction of methane produced by ABM relative to the total methane produced (the ABM fraction, f_{ABM}) was calculated using the model simulated reaction rates of ABM and HBM (Figure 2-5). As shown in Figure 2-5b, the ABM fraction is close to 1 at the beginning of the experiment because acetate concentrations are much higher than H_2 concentrations. The predicted ABM fraction was very low in the BES treatment during the first 60 days because the model was predicting considerable inhibition of ABM by BES (Figure 2-5b). After the first freezing period, the predicted ABM fraction increased in all the treatments during the thaw periods because of acetate buildup in the soil porewater and because CO_2 dissolved in the porewater was lost to the headspace by diffusion/degassing. The ABM fraction was predicted to decrease after toluene was added to the soils because toluene fermentation increases porewater dissolved CO_2 and H_2 concentrations. The model predicts that the average cumulative contribution of ABM to methane production is 75% of all the CH_4 produced, whereas HBM contributes 25%. These model-calculated relative rates of ABM and HBM are generally in agreement with the ABM fraction derived from ^{13}C isotopic signatures of CO_2 and CH_4 between days 145-201 as illustrated in Figure 2-5a.

2.3.7 No FTC Model Scenario

Given the successful performance of the diffusion-reaction model in reproducing the experimental results when FTCs were imposed, we used the model to simulate a scenario where no FTCs were imposed. In this model run, the temperature was fixed at 10°C during the first 60 days and 15°C between day 60-215. The input model parameters for this simulation is the same as that used for the simulation of the NL treatment (Tables 2-1 to 2-3). Notwithstanding there are no freezing periods in the no FTC scenario, the rates of CO_2 and CH_4 generation are lower than those in the FTC scenario (Figures 2-7a and 2-7b). The reason for the higher amounts of CO_2 and CH_4 produced in the FTC than in the no FTC scenario is because more DOC and acetate are produced in the FTC scenario by SMOCR and the subsequent higher rates of DOC fermentation and acetogenesis (Figures 2-7d and 2-7e). Figure 2-7f shows that toluene is degraded 23% faster under

no FTC condition compared to the FTC scenario during the thaw periods: in the no FTC scenario, it is consumed by day 160 whereas toluene is still available after day 215 in the FTC scenario (Figure 2-7c). Moreover, the rates of CO_2, CH_4 and DOC production are 1.4-times, 1.35-times, and 5-times higher, respectively, under the FTC scenario than under the no FTC scenario (Figure 2-7f).

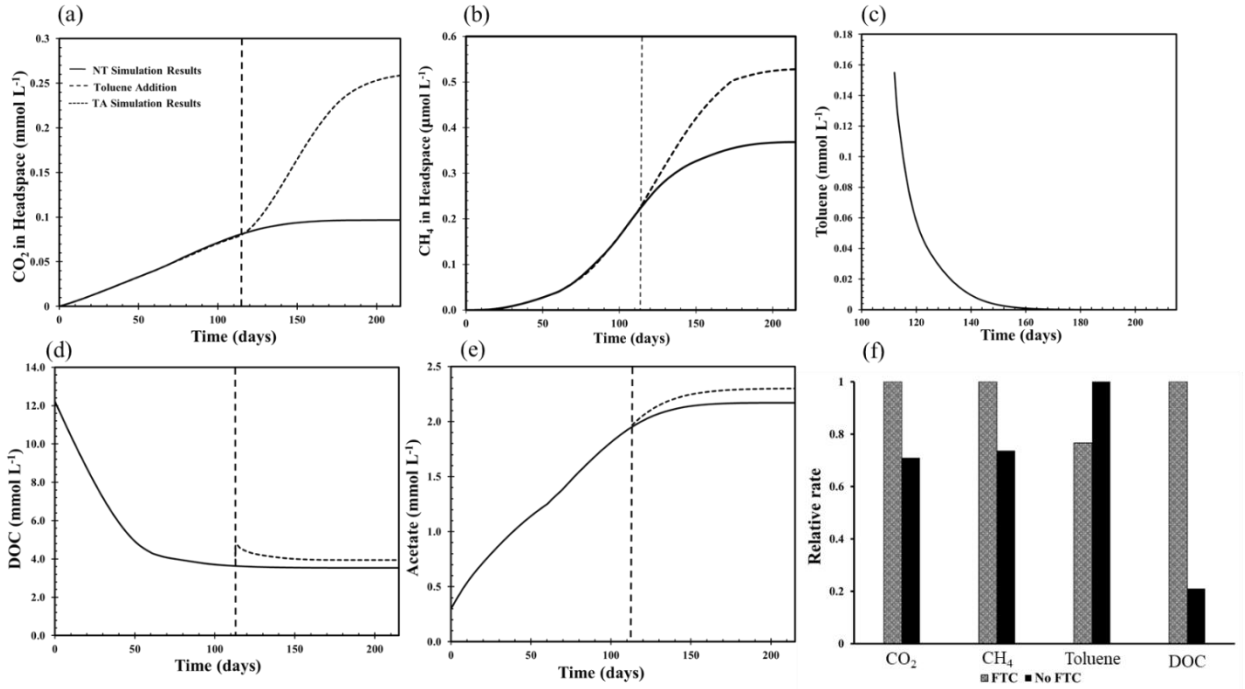

Figure 2-7: Simulation results of control scenario for (a) headspace CO_2 concentration, (b) headspace CH_4 concentration, (c) toluene concentration, (d) DOC, and (e) acetate in sulfate in soil porewater, and (f) relative rates of CO_2 and CH_4 generation, toluene consumption, and DOC production/consumption in FTC and control scenarios.

2.4 Discussion

2.4.1 Reaction pathways and rates

The results show that anaerobic degradation processes are strongly influenced by temperature because the freezing periods significantly reduce the rates of anaerobic reactions and cause freezing-induced soil matrix disturbance and DOC release; however, the rates of the anaerobic reactions increase during thaw periods (Figure 2-8). The dominance of sulfate reduction and methanogenic reactions change over time: sulfate reduction reactions play an important role when an adequate amount of sulfate is available in the system during the first 60 days (Figure A1-2).

However, methanogenic degradation of DOC and toluene becomes dominant in the anoxic, electron acceptor-limited conditions that occur after day 60 (Figure 2-8 d-f).

The changes in the methanogenic pathways HBM and ABM over time during the experiment can be identified using both isotopic analyses and numerical modeling. The model predicts that the rates of the HBM and ACET reactions increase when H_2 accumulates in the system because of DOC fermentation (Figure 2-8 d-f). The HBM rate then starts to decrease after the second thaw period because of H_2 depletion, which occurs when the rate of H_2 consumption is greater than its rate of production. In contrast, the rate of ABM increases over time because acetate concentration increase due to acetogenesis (ACET) and DOC fermentation (DF) of the DOC released by the SCOR reaction. Thus, the model predicts overall that the ABM fraction relative to HBM increases with time in the experiment. As section *3.4* highlighted, the ABM fraction predicted by the model is in good agreement with the ABM fraction calculated using the $\delta^{13}C\text{-}CO_2$ and $\delta^{13}C\text{-}CH_4$ isotope compositions observed. For the soil temperature during the thaw periods of 15°C, the model predictions that: (1) the average ABM fraction is around 75% , and (2) the acetogenesis rate is higher than that of HBM, indicating that it outcompetes HBM for the shared H_2 substrate, are in agreement with previous studies (Conrad, 2020; Conrad and Klose, 1999; Fenchel *et al.*, 2012; Fu *et al.*, 2019; Hoehler *et al.*, 1999; Kotsyurbenko, 2005).

The model's ability to accurately predict the relative rates of ABM and HBM is evidence that the model's microbial reaction network is representing the most important reactions occurring in the soil. Although we did not rely on thermodynamic constraints on methanogenic and fermentation pathways to predict the relative energetic favorability of and competition between the pathways (Jin and Kirk, 2018), the kinetic inhibition factors used to inhibit the fermentation when sulfate was present successfully predicted the competition between sulfate reduction and fermentation/methanogenic pathways. Representing the DOC, lactate and toluene fermentation reactions as separate reactions from methanogenesis, and fitting these reactions' rates to the measured concentrations of the fermentation products and methanogenic precursors acetate and H_2, is very important to the reaction network (Garg *et al.*, 2017; Gieg *et al.*, 2014); it is likely one of the reasons our model was able to predict the ABM versus HBM methanogenic pathways and match the ABM fraction derived from the α_{CO_2/CH_4} results as well as it did, despite not using the

α_{CO_2/CH_4} results to fit the model. Other conceptual microbial reaction networks proposed or used in models have grouped the initial fermentation, HBM and ABM reactions together (*e.g.*, Edwards and Grbić-Galić, 1994, Molins *et al.*, 2010). Our model parameters therefore also provide the rate constants for the fermentation reactions, such as DF, TF, HBM and ABM, which are not often derived and reported. (Table 2-1). According to the simulation results, TF contributes to 74% of the overall toluene natural attenuation, sorption contributes to 11%, and evaporation/volatilization contributes to 15%.

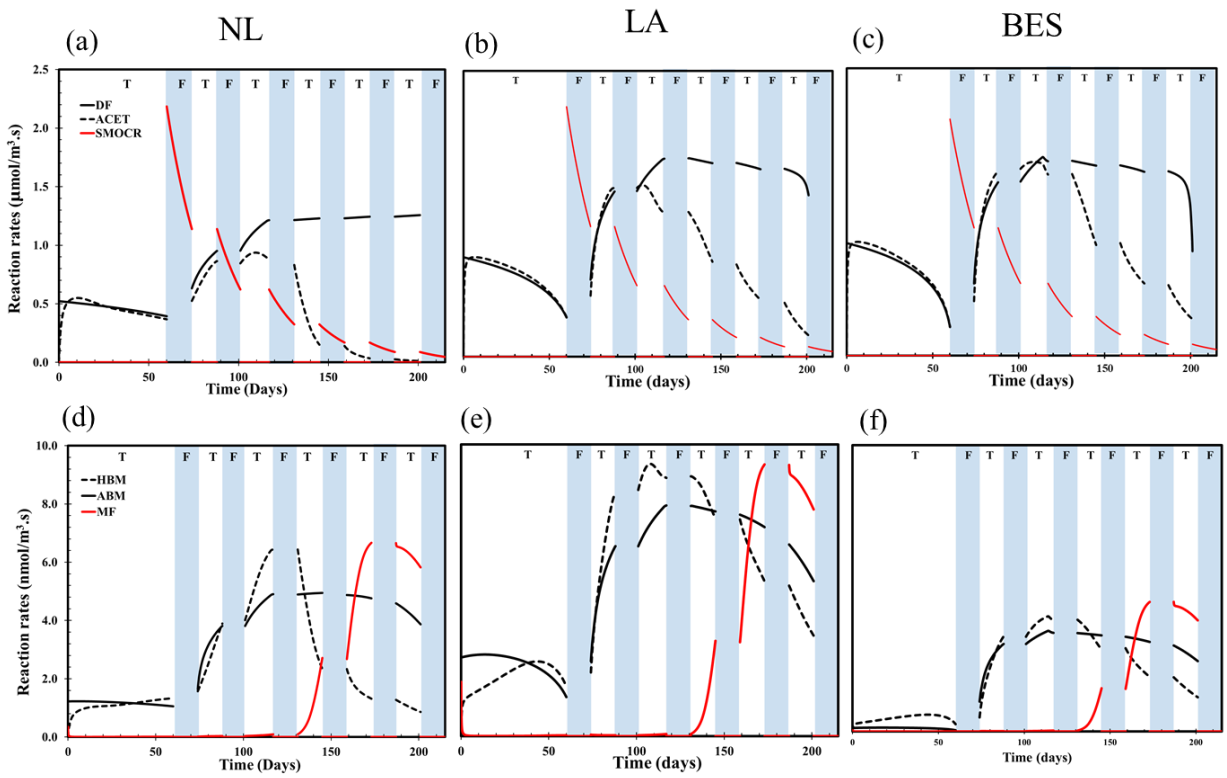

Figure 2-8: Simulation results of the rates of the DF (DOC fermentation), ACET (acetogenesis), and SMOCR (soil matrix organic carbon release) reactions in soils with 3 different treatments (a-c), and the rates of hydrogen-based methanogenesis (HBM), acetate-based methanogenesis (ABM), and methane fermentation/reverse HBM (MF) in soils with different treatments (d-f) during 215 days of experiment with freeze (F, at -10°C) and thaw (T, at 15°C) cycles.

When simulating the FTC experimental results, accurately representing the freezing-induced soil matrix organic carbon release of DOC into solution was a key reaction for predicting the changes

in the total DOC in solution. The observed increases in DOC after freezing and the interpretation that freezing-induced soil matrix disturbances, and thus physical soil organic carbon degradation, is driving this DOC increase is in line with what other studies have observed (Giesler *et al.,* 2007; Matzner and Borken, 2008; Song *et al.,* 2017). Furthermore, a considerable decrease in the $SUVA_{254}$ index following each freezing period for the soils with different treatments supports the interpretation that the DOC increase is due to a release of soil matrix and/or microbial biomass organic carbon, as microbially-derived dissolved organic matter has a relatively low $SUVA_{254}$ index (McKnight *et al.,* 1994; Vestgarden and Austnes, 2009). This freezing-induced release of DOC into soil porewater has been identified as one of the major effects of FTCs on soil biogeochemistry observed when comparing winter and spring seasons with many FTCs with those having more snow cover and less FTCs (Fuss *et al.,* 2016; Koponen and Bååth, 2016).

The equations which account for how temperature modulates microbial reaction rates (Eq. 11) and effective gas diffusion coefficients (Eq. 6) are some of the key functions in the modelling framework which enable the prediction of the impact of FTCs on reaction and transport rates. These temperature functions can also be used to simulate the impact of any temperature fluctuations on PHC NSZD at contaminated sites, regardless of whether they involve fluctuating between freezing (<0°C) and above freezing conditions (>0°C). Accounting for the non-linear impacts of temperature on microbial reaction rates (*e.g.,* Eq. 2-11) and on other processes will be important to account for in modeling frameworks for NSZD going forward. Altogether, the reaction network and diffusion-reaction model framework that we have presented herein, especially the inclusion of these temperature dependency functions, can be used as the basis for modeling methanogenic NSZD at any contaminated site.

2.4.2 Effect of FTCs on toluene biodegradation and CO_2 and CH_4 generation

In the no FTC scenario modelled, toluene is degraded 23% faster compared to the FTC scenario during the thaw periods; however, the cumulative CO_2 and CH_4 generation is 29% and 26% lower, respectively, than in the experimental and modelled FTC scenario results. The predicted increase in cumulative toluene degradation in the no FTC scenario is predicted because of more active days where the reaction rates are not inhibited by below-zero temperatures and more sulfate available in the system under the no FTC scenario. In the FTC scenario, the only reaction whose rate is enhanced by the FTCs is DOC production by soil matrix organic carbon release (SMOCR

reaction). Comparing the predictions of the no FTC model scenario with the FTC scenario highlights the important influence on DOC production by soil organic carbon release during FTCs on the overall CH_4 and CO_2 generation. Without this enhanced DOC production in the FTC scenario relative to the no FTC scenario, less CO_2 and CH_4 would have been produced in the FTC scenario than in the no FTC scenario due to the near-zero reaction rates of all the CO_2 and CH_4 producing reactions during the freezing periods. The no FTC scenario model-predicted results reveal that FTCs produce two outcomes which are less preferred than their alternatives: higher cumulative CO_2 and CH_4 generation and lower cumulative PHC degradation rates. Thus, in areas where snow cover is reduced and soils are exposed to FTCs more often, we can expect to see lower PHC degradation rates and higher CO_2 and CH_4 generation at contaminated sites where methanogenic PHC degradation is the dominant process.

2.5 Summary and Conclusions

We conducted a 215 day-long incubation experiment and reproduced the experimental results using a diffusion-reaction model which included 11 microbial reactions, toluene sorption/desorption, and gas diffusion to better understand how FTCs modulate soil geochemistry, methanogenic toluene biodegradation and CO_2 and CH_4 production. In the batch experiment, we imposed anoxic, saturated conditions and 5 successive freeze-thaw cycles (FTCs) where the temperature fluctuated from -10°C to 15°C. Based on the results obtained in this project, the following conclusions can be drawn:

- The model successfully reproduced the experimental time series trends in porewater chemistry and headspace gas concentrations, indicating that the biogeochemical reaction network captures the most important reactions. This model represented the impacts of temperature on microbial reaction rates and gas diffusion rates and predicted the near-zero rates during the -10°C freezing periods by applying temperature functions to the calculation of the maximum rate constants and effective diffusion coefficients, respectively.

- Toluene addition to the incubations on day 113 increased CO_2 and CH_4 concentrations in all three treatments relative to the NT incubations. The cumulative CO_2 and CH_4 generation increased by 136% and 87%, respectively, in the NL-TA treatment, by 117% and 61%, respectively in the LA-TA treatment, and by 50% and 33% in the BES-TA treatment. We

predicted this in the model by representing toluene fermentation, acetogenesis, hydrogen-based methanogenesis, and acetate-based methanogenesis as separate reactions.

- The average fraction of ABM contributing to methane production in the model was around 75%, and the ABM fraction calculated from the $\delta^{13}C$-CO_2 and -CH_4 results agreed with this. The model confirms that methanogenic toluene degradation is the dominant toluene attenuation mechanism, representing 74% of the attenuation, with sorption contributing to 11%, and evaporation contributing to 15%, which demonstrates that methanogenic toluene biodegradation (in anoxic soil, in the absence of electron acceptors) can contribute to natural toluene attenuation.

- Representing the effects of FTCs on porewater DOC production due to freezing-induced soil matrix disturbance was key for accurately simulating DOC concentrations as well as CO_2 and CH_4 generation. The considerable decrease in the $SUVA_{254}$ index following each freezing period also confirms that post-freezing DOC production can be explained by soil matrix organic carbon being released, as microbially-derived dissolved organic matter has a relatively low $SUVA_{254}$ index.

- In a model simulated scenario with no FTCs imposed, CO_2 and CH_4 generation are 29% and 26% lower, respectively than in the FTC condition because less DOC is produced in the no FTC scenario, whereas toluene biodegradation is 23% faster in the no FTC scenario. Hence, this no FTC scenario showed that FTCs slow down toluene degradation while enhancing CO_2 and CH_4 production, which is a less preferred outcome for contaminated site remediation.

- Overall, our model was able to successfully reproduce the microbial reaction network and gas transport processes controlling methanogenic toluene degradation and CO_2 and CH_4 generation from the soil, and the effect of FTCs on these reaction and process rates.

Impacts of Water Table Fluctuations on Methanogenic Hydrocarbon Degradation

Mehdi Ramezanzadeh[1*], Stephanie Slowinski[1], Fereidoun Rezanezhad[1], Jane Ye[1], Clement Alibert[1], Marianne Vandergriendt[1], David L. Rudolph[2], Neil R. Thomson[3], and Philippe Van Cappellen[1]

[1] Ecohydrology Research Group, Department of Earth and Environmental Sciences and Water Institute, University of Waterloo

[2] Department of Earth and Environmental Sciences, University of Waterloo, Waterloo, Ontario, Canada

[3] Department of Civil and Environmental Engineering, University of Waterloo, Waterloo, Ontario, Canada

[*]Corresponding author: Mehdi Ramezanzadeh

Ecohydrology Research Group, Department of Earth and Environmental Sciences and Water Institute, University of Waterloo
200 University Avenue West, Waterloo, Ontario, Canada N2L 3G1
Phone: (519) 888-4567,
Email: m8ramezanzadeh@uwaterloo.ca

This chapter will be modified for submission to the Journal of *Environmental Science & Technology*:

M. Ramezanzadeh, S. Slowinski, F. Rezanezhad, J. Ye, C. Alibert, M. Vandergriendt, D. L. Rudolph, N. R. Thomson, and P. Van Cappellen. Impacts of Water Table Fluctuations on Methanogenic Hydrocarbon Degradation. To be submitted to *Environmental Science & Technology*.

3 Effects of Water Table Fluctuations on Methanogenic Hydrocarbon Degradation

3.1 Introduction

subsurface contamination by petroleum hydrocarbons (PHCs) is a global environmental issue because some PHCs pose a significant threat to human health due to their toxicity (Gray *et al.*, 2010; Mayer & Hassanizadeh, 2005). Thus, it is important to understand major hydrologic and climatic factors affecting the fate, transport and distribution of PHCs (Ossai *et al.*, 2020). Natural source zone depletion (NSZD) of PHCs due to biodegradation, dissolution, sorption, and volatilization has attracted attention in the last few decades (BenIsrael *et al.*, 2019; Garg *et al.*, 2017; Khasi *et al.*, 2019; Kulkarni *et al.*, 2020; Ramezanzadeh *et al.*, 2022; Shi *et al.*, 2020). In these PHC-contaminated environments, aerobic and anaerobic respiration takes place where the reduction of electron acceptors (EA) such as oxygen (O_2), nitrate (NO_3^-), iron (III) (Fe^{3+}), manganese(IV) (Mn^{4+}), and sulfate (SO_4^{2-}) is coupled to the oxidation of a PHC as an electron donor (ED). These electron acceptors often become scarce in a PHC-contaminated zone because of respiration, or variable hydrological and climatic regimes (Haberer *et al.*, 2012; Karimi Askarani *et al.*, 2018). As a result, fermentative and methanogenic degradation of PHCs under anoxic conditions become the dominant pathways leading to increased methane (CH_4) and carbon dioxide (CO_2) effluxes. While ex-situ treatment methods are known to be sources of greenhouse gases (GHGs) (Ellis & Hadley, 2009), the contribution of NSZD to GHG effluxes is still not clear (Garg *et al.*, 2017). Therefore, comprehending factors modulating degradation pathways and GHG effluxes during NSZD processes and the impact on the climate system is required (Blake *et al.*, 2015; Dean *et al.*, 2018; Jones *et al.*, 2008; Lemming *et al.*, 2012).

Climate change can contribute to extreme drought and precipitation events, causing fluctuations in the water table and influencing soil moisture dynamics (Christiansen *et al.*, 2017; Dinsmore *et al.*, 2009; Easterling *et al.*, 2000; Estop-Aragonés *et al.*, 2013; Fairbairn, 2020). Soil moisture is a major factor controlling the rate of physical, geochemical and microbial processes contributing to NSZD (Henry, 2007; Keiluweit *et al.*, 2016, 2017; Moyano *et al.*, 2013; Pronk *et al.*, 2020; Prowse *et al.*, 2009) by modulating the distribution of EAs, PHCs, natural organic matter, nutrients, and microorganisms (Haberer *et al.*, 2012; Holden & Fierer, 2005; Lin *et al.*, 2012; Rezanezhad *et al.*, 2014; Rühle *et al.*, 2015; Williams & Oostrom, 2000). The rate of GHG effluxes and PHC degradation can potentially be affected by groundwater level fluctuations (Henneberg *et al.*, 2016).

In fact, a higher water level leads to greater effluxes of CH_4 because of aceticlastic methanogenesis and hydrogenotrophic methanogenesis under anoxic conditions (Brewer *et al.*, 2018; Conrad, 2020; Von Fischer & Hedin, 2007; Günther *et al.*, 2020; Sexstone *et al.*, 1985; Sun *et al.*, 2012), while it lowers the rates of hydrocarbon degradation and CO_2 generation (Basiliko *et al.*, 2009; Brewer *et al.*, 2018; Christiansen *et al.*, 2016; Pronk *et al.*, 2020; Sierra *et al.*, 2017; Van De Ven *et al.*, 2021). In contrast, a water table decline usually decreases CH_4 effluxes due to inhibition of methanogenesis or oxidation of CH_4 in the presence of O_2, whereas this decline increases CO_2 emissions and PHC degradation because of faster diffusion in air than in water, and higher aerobic degradation rates (Aurela *et al.*, 2007; Baehr & Corapcioglu, 1987; Berglund & Berglund, 2011; Christiansen *et al.*, 2016; Elberling *et al.*, 2011; Estop-Aragonés *et al.*, 2013; Hogg *et al.*, 1992; Klüpfel *et al.*, 2014; Molins *et al.*, 2010; Pronk *et al.*, 2020; Sihota *et al.*, 2011; Silvola *et al.*, 1996; Van De Ven *et al.*, 2021). Methanogenic degradation of PHCs undergoing water table fluctuations (WTFs) and variable moisture regime has not been investigated in detail. Hence, understanding how NSZD of PHCs responds to large temporal variations in soil moisture during WTFs is vital to predict the fate and transport of PHCs, and the associated CH_4 and CO_2 effluxes (Klüpfel *et al.*, 2014; Moyano *et al.*, 2013).

The Impact of WTFs and soil moisture dynamics on NSZD processes has been investigated in numerous laboratory and field studies (*e.g.*, Dinsmore *et al.*, 2009; Knorr *et al.*, 2009; Moore & Knowles, 1989; Sun *et al.*, 2012; Van De Ven *et al.*, 2021; Xia *et al.*, 2022). Recent years has focused on the influence of soil moisture dynamics on GHG emissions (*e.g.*, Berglund & Berglund, 2011; Günther *et al.*, 2020; Leifeld *et al.*, 2019; Xue *et al.*, 2020). Some field studies have highlighted the importance of drainage and imbibition cycles on GHG emissions, microbial activity, and soil carbon and nitrogen dynamics (Estop-Aragonés *et al.*, 2013; Kettunen *et al.*, 1999; Knorr *et al.*, 2009; Mander *et al.*, 2011; Martikainen *et al.*, 1993; Pronk *et al.*, 2020; Rezanezhad *et al.*, 2014; Säurich *et al.*, 2019; Sun *et al.*, 2012; Tiemeyer *et al.*, 2016; Whittington & Price, 2006; Wiedermann *et al.*, 2017; Xue *et al.*, 2020; Zhong *et al.*, 2017). Recent studies have shown how drained peatlands might exacerbate global warming through continued CO_2 emissions, whereas peatland rewetting is effective for climate change mitigation, despite the increase in CH_4 emission (Franz *et al.*, 2016; Günther *et al.*, 2020; Hahn *et al.*, 2015; Leifeld *et al.*, 2019). In addition to field studies, laboratory experiments have linked GHG emissions, organic carbon

degradation, and microbial activity to water table depth (Berglund & Berglund, 2011; Dinsmore *et al.*, 2009; Dobson *et al.*, 2007; Farnsworth *et al.*, 2012; Henneberg *et al.*, 2016; Legout *et al.*, 2009; Mäkiranta *et al.*, 2009; Moore & Knowles, 1989; Peralta *et al.*, 2014; Prieto-Espinoza *et al.*, 2021; Pronk *et al.*, 2020; Wessolek *et al.*, 2002; Xia *et al.*, 2022), soil moisture dynamics (Brewer *et al.*, 2018; Christiansen *et al.*, 2017; Fairbairn, 2020; Hack *et al.*, 2015; McNicol & Silver, 2014; Sierra *et al.*, 2017), and soil properties (Berglund & Berglund, 2011; Fairbairn, 2020; Ghezzehei *et al.*, 2019; Moyano *et al.*, 2013; Regina *et al.*, 2004; Tang & Riley, 2019). It can be inferred from the studies that CO_2 and N_2O emissions peaked at different drainage depth and moisture content depending on soil type, whereas CH_4 generation peaked when the system was saturated (Dinsmore *et al.*, 2009; Fairbairn, 2020; Moyano *et al.*, 2013). In terms of microbial activity, previous studies have conflicting results. A number of studies showed that the composition of microbial communities changed in the fluctuating water table zone, influencing the rates of CO_2 and CH_4 production (Cruz-Martínez *et al.*, 2012; Fierer & Schimel, 2002; Gupta *et al.*, 2020; Minick *et al.*, 2019; Oertel *et al.*, 2016; Prieto-Espinoza *et al.*, 2021; Rühle *et al.*, 2015; Sheng *et al.*, 2021; Sun *et al.*, 2012; Xia *et al.*, 2022; Xue *et al.*, 2020); while others observed no systematic difference (Pronk *et al.*, 2020; Rezanezhad *et al.*, 2014). Previous studies also suggests that frequent drainage-imbibition cycles might enhance microbial tolerance to dynamic redox conditions. So far, several studies have investigated the impact of WTFs and soil moisture dynamic on carbon turnover, but the long term and short term effects of WTFs on methanogenic degradation of PHCs are still poorly understood. Van De Ven *et al.* (2021) quantified the impact of WTFs on NSZD rates in a biodiesel-contaminated sandtank, and reported that surface effluxes due to the redistribution of contaminants, increased aerobic degradation, and the liberation of anaerobically produced gas accumulated below the water table.

In addition to experimental studies, several biogeochemical reactive transport models have been developed to simulate NSZD processes (Ebrahimi & Or, 2017; Essaid *et al*., 2003; Mayer *et al*., 2002; Molins *et al*., 2010; Molins & Mayer, 2007; Ng *et al*., 2015; Šimůnek & Suarez, 1993; Su *et al*., 2021; Vencelides *et al*., 2007). Mayer *et al*. (2002) and Molins & Mayer (2007) combined a biogeochemical reaction network and physical transport processes into a multiphase multicomponent flow and reactive transport model, called MIN3P, which has been used to simulate the reactive transport of PHCs, CO_2 and CH_4 during NSZD. Later, Molins *et al*. (2010)

simulated a PHC-contaminated site using a similar biogeochemical reactive transport model that incorporates a reaction network, multicomponent gas diffusion and advection, and solute transport. Their results confirmed that methanogenic biodegradation is the dominant PHC degradation pathway at a mature anoxic PHC-contaminated site. A number of studies simulated the effect of WTFs and moisture dynamics on contaminant transport and CO_2 effluxes (Amos & Mayer, 2006; Brookfield et al., 2006; Davidson et al., 2012; Fairbairn, 2020; Ghezzehei et al., 2019; Kettunen, 2003; Legout et al., 2009; Moyano et al., 2013; Rubol et al., 2013). The numerical models showed that the rate of CO_2 production is limited by the diffusion of organic carbon substrates at low soil moisture, while it is limited by availability of O_2 at high soil moisture. However, the rate of anaerobic reactions, such as methanogenesis is predicted to increase with soil moisture as O_2 can inhibit anaerobic reactions during drying (Davidson *et al.*, 2012; Fairbairn, 2020).

Although previous studies have investigated NSZD processes under variable moisture conditions using laboratory experiments, field monitoring, and/or reactive transport, the methanogenic biodegradation of PHCs and the accompanying effluxes of CO_2 and CH_4 under anoxic versus variable redox conditions are still not well understood. Therefore, the specific objective of this study was to delineate the effects of WTFs on geochemistry, methanogenic naphthalene biodegradation, and CH_4 and CO_2 effluxes. Using a combined experimental and modeling approach, we conducted a column experiment in which four soil columns were subjected to cycles of drainage (20 cm bss) and imbibition (0 cm bss), and four soil columns remained saturated. Three of the static and fluctuating soil columns were spiked with naphthalene and/or ethanol, while the remainders were not contaminated by naphthalene. The responses to the imposed WTFs were monitored by measuring CO_2 and CH_4 effluxes, dissolved CO_2 and CH_4, depth-dependent moisture content, and by analyzing the porewater chemistry at the end of each drainage-imbibition cycle. A diffusion-reaction model was developed to simulate the effect of WTFs on physical process rates and (bio)geochemical and geomicrobial reaction rates.

3.2 Materials and Methods

3.2.1 Soil column experiment

3.2.1.1 Soil sampling and analyses

Undisturbed soil cores were collected from a former gasoline storage and refining facility where gasoline and other hydrocarbon compounds were stored. The site was used from the early 1950's to 2001 for storage and distribution of various petroleum products, including two underground storage tanks and one above-ground storage tank which were removed in 2005 (Golder Associates Ltd., 2018). The soil ranges from sandy silt to silty sand with an estimated hydraulic conductivity of 10^{-1} cm s^{-1} or less. The groundwater depth historically ranges from 1.91 to 2.77 m below ground surface (Golder Associates Ltd., 2018). Sampling activities indicate presence of petroleum contamination in the soil and groundwater (Exp Energy Services Ltd., 2015; Golder Associates Ltd., 2018). From these historical surveys, contamination appears to be heterogeneously distributed around the site. A total of 13 soil cores, ~75 cm long, were collected from 1.4- 2.3 m below ground surface, straddling the water table. The soil cores were stored under sealed, nitrogen-flushed, sub-oxic conditions at 4°C until used.

The bulk density and porosity were determined from one the cores using the methods described by Hao *et al*. (2008), assuming the particle density of 2.65 g cm^{-3}. The average bulk density and porosity of 5 samples were 1.53 g cm^{-3} and 0.43, respectively. Particle size distributions were determined at five depths along a single representative soil core by suspending samples in a 4%-w/w sodium metaphosphate solution for several hours on a stir plate, then pipetting suspended samples into a wet dispersion unit feeding to a Analysette 22 Microtec Plus laser diffraction particle size analyzer (Fritsch, Germany). Total carbon, total organic carbon, and total nitrogen in oven-dried (105°C, 2 days) homogenized soil were measured via CHNS analysis using a Carlo-Erba NA-1500 Elemental Analyzer (Carlo-Erba Instruments, Italy). Total organic carbon and total nitrogen were each found to be below the detection limit of 0.01 g/g, while average total carbon was measured as 0.02 g/g.

Sorption tests were conducted to assess the context-specific aqueous/solid partitioning potential of naphthalene. Although naphthalene sorption is known to have dependence on soil organic carbon content (Li *et al.*, 2020; Shi *et al.*, 2020), and a variety of sorption distribution coefficients (K_d) for

this compound have been determined in the literature for a variety of soils (*e.g*., Xing, 1997), it was unknown how the pre-existing hydrocarbons in the soil might affect sorption of naphthalene. To investigate this, we determined context-specific 48-hour isotherms for naphthalene at 25, 50, and 100% of the maximum experimental concentrations (5 mg L^{-1} or 0.039 mM). The sorption tests were performed at room temperature (~24°C) and soil was treated with 1.84 mmol kg^{-1} mercuric (II) chloride as biocide.

3.2.1.2 Soil column system

Eight stainless-steel columns (7.5 cm inner diameter and 60 cm long) were each filled with 45 cm of undisturbed soil cores. In addition, four equilibrium columns (clear acrylic columns, inner diameter: 7.5 cm, length: 60 cm, Soil Measurement Systems, LLC, USA, model CL-021) filled with 45 cm of artificial porewater (APW) and connected to the stainless-steel soil columns to control the water table level in the soil columns. For a more detailed explanation of this soil column setup, the reader is referred to Rezanezhad *et al*. (2014). The APW solution was prepared to closely match the pH, electrical conductivity, and ionic composition of groundwater from the field site, and contained $NaHCO_3$ (1.00 mM) and $CaCl_2$ (0.80 mM), $KHCO_3$ (1.00 mM), and $MgCl_2$ (0.15 mM) in ultrapure deionized water. The APW in the equilibrium columns were sparged continuously with N_2 gas to ensure anoxic conditions. A photo and a schematic diagram of the column experimental setup are shown in Figures 3-1 and 3-2. The soil columns were equipped with sampling ports for moisture content, Eh, temperature, porewater sampling, and gas analyses (see *3.2.1.4*). There were also two ports on top of the columns through which the headspace was flushed with humid air to minimize evaporative loss of water.

Figure 3-1: A photo of the stainless-steel columns equipped with moisture, temperature, and redox sensors, and water and gas samplers.

3.2.1.3 Water table fluctuation regime

The columns were packed under saturated conditions and remained saturated for 140 days. Then, the four fluctuating water table columns were subjected to 3 successive cycles of 6-week drainage-imbibition with water level fluctuating from 0 cm below soil surface (bss) to 20 cm bss. In the remainders, the water table was maintained at 0 cm bss (see Figure 3-2a).

On day 111, 5 ml pure ethanol was injected into one static (SEC) and one fluctuating (FEC) columns, while 5 ml ethanol-naphthalene solution with naphthalene concentration of 15000 mg L^{-1} was injected into two static (SEN1 and SEN2) and two fluctuating (FEN1 and FEN2) columns. In addition, 5 ml APW solution was injected into one static (SWC) and one fluctuating (FWC) columns as control columns to compare the physical effect of injecting 5 ml solution into the columns. The solutions were injected into the soil columns from the port located at 17.5 cm bss. To change the water level by 1.5 cm day^{-1}, the peristaltic pump for the equilibrium column controlling FEN1, FEN2, and FEC was set at a flow rate of 6.4 ml hr^{-1}.

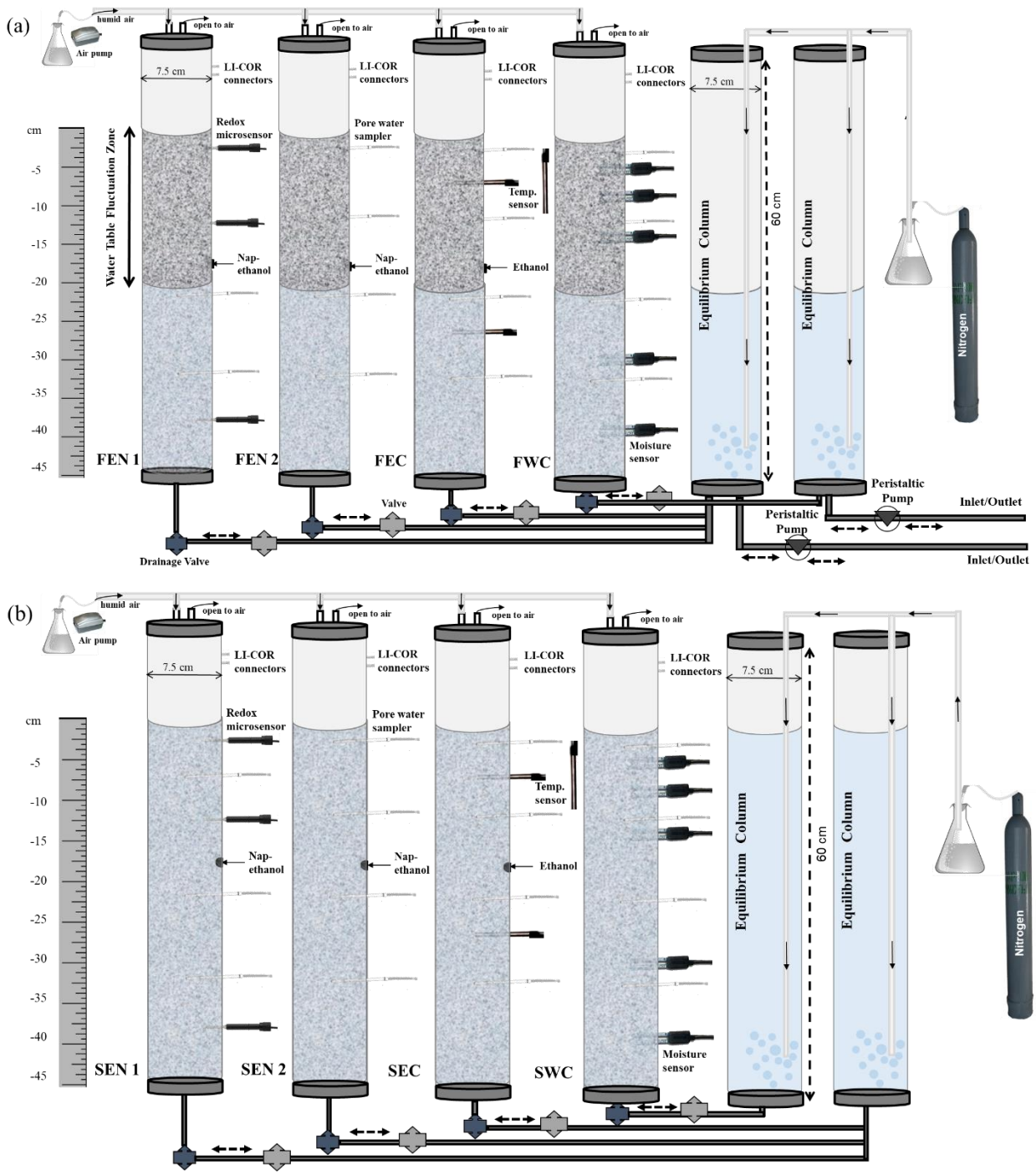

Figure 3-2: Schematic diagrams of the column experimental setup for (a) the fluctuating water table columns and (b) the static water table columns. FEN1 and FEN2 are referred to the fluctuating nap-ethanol (naphthalene-ethanol) amended columns, SEN1 and SEN2 are the static ethanol-naphthalene amended columns, FEC is the fluctuating ethanol control column, SEC is the static ethanol control column, FWC is the fluctuating water control column, and SWC is the static water control column.

3.2.1.4 Instrumentation

The columns were equipped with airtight lateral ports regularly spaced every 5 cm. As illustrated in Figure 3-2, stainless-steel porewater samplers (5 cm length, 2.5 mm diameter, with a filter pore size of 180 µm) were installed at 7.5, 22.5, and 32.5 cm bss in FEN1 and SEN1 and at 2.5, 12.5, 22.5, and 32.5 cm bss in other columns. Up to 5 mL aqueous samples for chemical analysis are collected every 3 weeks.

Five high-resolution redox potential (Eh) microelectrodes with 10 µm glass tip (Unisense, Denmark) was installed at 2.5, 12.5, and 37.5 cm bss in FEN1 column and at 2.5 and 37.5 cm bss in SEN1 column (Figure 3-2). Each pair of Eh microelectrode was combined with an external, micro-size reference electrode (open-ended Ag–AgCl electrode with gel-stabilized electrolyte, Unisense), which was in contact with the bottom outflow/inflow of the soil column. Electrode readings were recorded by a high-impedance millivolt- meter (Unisense), which in turn was connected to the control computer. Three temperature sensors (DaqLink Fourier Systems Ltd., #DBSA720) were installed at 7.5 and 27.5 cm bss in the FEN2 column (Figure 3-2) and one outside the column setup. In the FWC and SWC columns, 5 ECH2O EC-5 soil moisture sensors (Decagon, Devices, Inc, USA) occupied ports at 5, 10, 15, 30, and 40 cm bss. The Eh, temperature, and moisture content were recorded every 10 sec, 15 sec, and 15 min, respectively.

3.2.1.5 Headspace gas fluxes

CO_2 and CH_4 fluxes were measured three times a week by connecting the headspace ports to an automated multiplexed CO_2 flux analyzer (Li-8100, Li-COR Biosciences, Lincoln, NE, USA) and a CH_4/CO_2/H_2O gas analyzer (Li-7810, Li-COR Biosciences, Lincoln, NE, USA) (see Figure 3-2). During the measurements, the upper ports of the columns were closed for 10 min, and air circulated in a closed loop through LI-8100, LI-7810, and the headspace. The CO_2 and CH_4 fluxes were measured from the rate of gas accumulation within the headspace, according to the method of Davidson *et al*. (2002) (for more details about the flux calculations using this setup see Rezanezhad *et al.*, 2014 and Pronk *et al.*, 2020).

3.2.1.6 Porewater and gas analyses

Porewater samples were collected every three weeks for analysis of dissolved naphthalene, dissolved organic carbon (DOC), dissolved inorganic carbon (DIC), major anions, pH, electrical conductivity (EC), dissolved gas, and ^{13}C isotope compositions of CH_4 and CO_2.

Dissolved naphthalene concentration was determined using a solvent micro-extraction technique. 2 mL porewater sample and 1 mL of dichloromethane solvent extractant spiked with metafluorotoluene tracer were added to a 4 mL glass vial. The vial was shaken for 20 min at 350 rpm and then left inverted for 15 min. The dichloromethane extractant was then removed from the vial using a 1 mL gas-tight glass syringe and transferred into a 2 mL glass vial. The extractant was then injected to an Agilent 7890A Gas Chromatograph (Agilent Technologies, China) at 275°C through a capillary column and naphthalene concentration was measured using a flame ionization detector (detection limit of 5 µg L^{-1}).

For analysis of DOC and DIC, 1.5 mL of each porewater sample was filtered through a ChoiceTM 0.45 µm nylon filter and then placed into a total organic carbon (TOC) glass tube prefilled with 6 mL ultrapure Milli-Q water (*i.e.*, 1:7 dilution). DOC samples were acidified to pH <3 using 3 drops of 1 M HCl. DIC and DOC samples were then analyzed on a TOC analyzer (Shimadzu TOC-LCPH/CPN; MDL: 3 and 6 µmol L^{-1}, respectively).

Approximately 0.5 mL of undiluted porewater sample was filtered through a 0.2 µm pore size membrane filter (Thermo Scientific Polysulfone filter) into a glass vial, preserved with 10 mg L^{-1} chromate, and then frozen at -20°C for later analysis of major anion concentrations including chloride anion (Cl^-), nitrate (NO_3^-), sulfate (SO_4^{2-}), acetate ($C_2H_3O_2^-$) and lactate ($C_3H_6O_3$) using ion chromatography (IC, Dionex ICS-5000 with a capillary IonPac® AS18 column; ± 3.0% error and ± 1.6% precision; MDL: 0.076, 14.7, 6.7, 0.7, and 0.4 µmol L^{-1}, respectively). pH and electrical conductivity (EC) were measured using LAQUAtwin pH and EC meters (LAQUA Twin meters, model Horiba B-213), requiring ~0.2 mL of unfiltered sample.

The headspace equilibration technique proposed by McAullife (1971) was used to measure dissolved CO_2, CH_4, and O_2 concentrations at different depths in the soil columns. Approximately 1 mL of each porewater sample was injected into a gas-tight plastic syringe prefilled with 40 mL

helium (He). The dissolved gas components in the porewater samples transferred to the He headspace during equilibration time, which was later measured using a Shimadzu Gas Chromatograph (Model GC-2014) equipped with a flame ionization detector and methanizer (for CO_2 and CH_4) and thermal conductivity detector (for H_2 and O_2) (Magen *et al.*, 2014).

The headspace equilibration technique was also used for $\delta^{13}C$ isotope analyses of dissolved CO_2 and CH_4. The gas samples obtained from the headspace equilibration technique were injected into He-filled Exetainer vials to analyze $\delta^{13}C$- CO_2 and $\delta^{13}C$- CH_4 via gas chromatography combustion (GCC) conversion through a Agilent 7890A gas chromatograph coupled to a Thermo Scientific Delta V Plus isotope ratio mass spectrometer via GC Isolink (Thermo Fisher Scientific, Germany) continuous flow isotope ratio mass spectrometer (CFIRMS) by the Environmental Isotope Laboratory at the University of Waterloo.

3.2.2 Simulation

The mass conservation equation for solute transport describing advection and diffusion of a sorbing, volatilizing, and decaying solute in a variably saturated porous medium can be described as:

$$\frac{\partial(\theta_l c_i)}{\partial t} + \frac{\partial(\rho_b c_{p,i})}{\partial t} + \frac{\partial(\theta_g c_{G,i})}{\partial t} + \nabla.[-(D_{el,i} + D_{eg,i}\mathrm{k_{G,i}})]\nabla c_i + u.\nabla c_i = R_i \qquad (3\text{-}1)$$

where θ_l and θ_g are the volume fraction of liquid phase and gas phase for substance i, c_i is the concentration [ML^{-3}] of the specimen i, u is darcy velocity [LT^{-1}], R_i is reaction rate [$ML^{-3}sec^{-1}$] of substance i, $c_{G,i}$ is the concentration [ML^{-3}] of specimen i in gas phase, ρ_b is bulk density [ML^{-3}] of soil, $c_{p,i}$ is the linear adsorption isotherm [MM^{-1}] for substance i.,and $k_{G,i}$ is the volatilization rate constant [1] of substance i. $D_{el,i}$ and $D_{eg,i}$ are the effective diffusion coefficients [$L^2\,T^{-1}$] for substance i in the aqueous phase and gas phase, respectively, that can be correlated to solute diffusivity in bulk solvent as follows (Millington & Quirk, 1961):

$$D_{el,i} = \frac{\theta_l^{\frac{10}{3}}}{\phi_e^2} D_{L,i} \qquad (3\text{-}2)$$

$$D_{eg,i} = \frac{\theta_g^{\frac{10}{3}}}{\phi_e^2} D_{G,i} \qquad (3\text{-}3)$$

where ϕ_e is effective porosity, and $D_{L,i}$ and $D_{G,i}$ are the solute diffusion coefficients [$L^2 T^{-1}$] for substance i in bulk solvent in the aqueous phase and gas phase, respectively.

In the first term of Eq. 3-1, θ_l can be obtained from the Richards' equation (Eq. 3-4). In this equation, the specific moisture capacity C_m and the effective saturation S_{ew} are taken from the van Genuchten retention model (Van Genuchten, 1980):

$$\left(\frac{C_m}{\rho g} + S_{ew}S\right)\frac{\partial H_p}{\partial t} + \nabla\left[-\frac{k}{\mu}(\nabla H_p + \rho g z)\right] = 0 \tag{3-4}$$

where S is storage coefficient (L^{-1}), H_p is pressure head (L). In this equation, a sinusoidal function can be imposed to mimic the water table regime in this experiment:

$$H = 0.45 + 0.1\left[\sin\left(\pi\frac{t+10.5}{21}\right) - 1\right] \tag{3-5}$$

where H is hydraulic head and t is time (days).

The second term in Eq. 3-1 models the adsorption/desorption of each chemical species to the solid phase (*i.e.*, the soil matrix) in porous media which accounts for decreasing and increasing in chemical transport flux of species as they attach to (adsorb) and detach from (desorb) the solid phase during traveling through the medium. In this study, the linear adsorption model is used to predict the solid concentration ($c_{p,i}$) from the concentration in the liquid phase as:

$$c_{p,i} = K_{d,i}C_{eq,i} \tag{3-6}$$

where $C_{eq,i}$ [ML^{-3}] is the concentration of aqueous substance i after equilibrium was reached, and $K_{d,i}$ [L^3M^{-1}] is the distribution coefficient for the linear model.

The final term in Eq. 3-1, R_i, represents chemical reactions, most of which are microbially-catalyzed, that account for changes in species concentration per unit volume porous medium per time. In the presence of a network of different reactions, R_i can be defined by:

$$R_i = \sum_j \nu_{i,j} r_j \tag{3-7}$$

where r_j is the rate of jth reaction in a reaction network, and $\nu_{i,j}$ is the stoichiometric coefficient of specimen i in the reaction j. Then the r_j can be calculated as follow:

$$r_j = k_j\, c_{EA}\, c_{ED} \tag{3-8}$$

where r_j is the rate constant for reaction j, and C_{ED} and C_{EA} are concentrations of electron donors and electron acceptors consumed in the reaction, respectively, both in [mol. L^{-1}].

It should be noted that some chemical species act as competitive inhibitors to some reactions who share a substrate, so an inhibition term in Eq. 3-10 for the inhibiting effect of O_2 on anaerobic reactions was incorporated:

$$r_{inh,j} = \frac{K_{inh,i,j}}{K_{inh,i,j} + c_i} \tag{3-9}$$

where $K_{inh,i,j}$ is inhibition constant for substance i in reaction j and $r_{inh,j}$ is the inhibition factor.

In this model, Henry's law can be applied to the boundary between the headspace and soil:

$$c_i^{aq} = \mathrm{k_{G,i}} c_g \tag{3-10}$$

where c_i^{aq} and c_g are equilibrium concentrations of substance i in aqueous phase and headspace. To investigate the impact of WTFs on biodegradation processes and gas emissions, a microbial reaction network of 12 microbially-catalyzed chemical reactions was implemented. The list of the chemical reactions and the associated fitting parameters are presented in Table 3-1. The initial concentrations of each chemical simulated in the reaction network are provided in Table 3-2.

In the numerical simulations used in this study, the transport, adsorption, and biodegradation of species in the soil domain are evaluated by solving Eq. 3-1, and 3-4 alongside corresponding boundary and initial conditions presented in Eq. 3-10 and Table 3-2. The reaction rates and solid concentration in the adsorption/reaction term of Eq. 3-1 are evaluated by Eqs. 3-6 and 3-7, respectively. Atmospheric concentrations are set for initial concentration of species in the headspace. Finally, interaction between two domains (soil and headspace) is modeled using Eq. 10. These sets of equations are solved using the COMSOL Multiphysics® software (version 5.6). We ran the simulations for 2 different experimental treatments: FEN and SEN.

Table 3-1: List of reactions included in the microbial reaction network and their reaction rate constants.

Reaction name	Chemical reaction	Rate constant (sec^{-1})
Naphthalene oxidation	$C_{10}H_8 + 12O_2 \rightarrow 10CO_2 + 4H_2O$	2.0e-7
Naphthalene fermentation	$C_{10}H_8 + 20H_2O \rightarrow 10\ CO_2 + 24H_2$	2.1e-8

Ethanol oxidation	$C_2H_6O + 3O_2 \rightarrow 2CO_2 + 3H_2O$	2.5e-5
Ethanol fermentation	$C_2H_6O + CO_2 \rightarrow 1.5C_2H_3O_2^- + 1.5H^+$	5e-7
Hydrogen-based methanogenesis/ Methane fermentation	$0.25CO_2 + H_2 \rightleftharpoons 0.25CH_4 + 0.5\ H_2O$	5.5e-7 / 8.1e-8
Acetate-based methanogenesis	$C_2H_3O_2^- + H^+ \rightarrow CO_2 + CH_4$	2.2e-8
Methane oxidation	$CH_4 + 2O_2 \rightarrow CO_2 + 2H_2O$	2.0e-7
Acetogenesis/ Acetate fermentation	$0.5CO_2 + H_2 \rightleftharpoons 0.25C_2H_3O_2^- + 0.75H_2O + 0.25H^+$	8.0e-6 / 5.1e-7
Acetate oxidation	$C_2H_3O_2^- + 2O_2 + H^+ \rightarrow CO_2 + 2H_2O$	5.2e-7
Glucose fermentation	$C_6H_{12}O_6 + 0.857H_2O \rightarrow 0.857\ CO_2 + 2.57C_2H_3O_2^- + 1.714H_2 + 2.576\ H^+$	1.5e-8
Glucose aerobic oxidation	$C_6H_{12}O_6 + 6O_2 \rightarrow 6CO_2 + 6H_2O$	9.5e-8

Table 3-2: Initial concentrations of each species modeled in the microbial reaction network.

Substance	Initial concentration (mol m^{-3})
SO_4^{2-}	0.250
$C_{10}H_8$	0
$O_2\ (aq)$	0.117
$C_2H_3O_2^-$	0.017
$C_6H_{12}O_6$	1.733
DOC	1.75
DIC	5.987
CO_2 (aq)	5.987
H_2 (aq)	1e-6
CH_4 (aq)	0.005
C_2H_6O	0
CO_2 (g), CH_4 (g), H_2 (g)	0

Table 3-3: Model parameters used in the numerical simulation of FEN and SEN columns.

Parameters	Values
T (K)	295.15
ϕ_e	0.425
pH	7.2
$K_{H_2}^H$	0.018
$K_{CH_4}^H$	0.034
$K_{O_2}^H$	0.032
$K_{CO_2}^H$	0.83
$D_{O_2}^g$	2.1e-9
$D_{O_2}^{aq}$	1.59e-5
$D_{CH_4}^g$	1.9e-5
$D_{CH_4}^{aq}$	1.6e-9
$D_{CO_2}^g$	1.1e-5
$D_{CO_2}^{aq}$	1.2e-9
$D_{H_2}^g$	7.5e-5
$D_{H_2}^{aq}$	2.7e-9
D_{Sulf}	6.8e-10
D_{Nap}	1.8e-10
D_{Acet}	6.8e-10
D_{Gluc}	6.14e-10
$D_{ethanol}$	1.23e-9
K_{inh,SO_4}(mol m^{-3})	0.001
$K_{inh,Acet}$(mol m^{-3})	25
K_{inh,H_2}(mol m^{-3})	0.0001
K_{inh,CH_4}(mol m^{-3})	0.25
K_{inh,O_2}(mol m^{-3})	0.016

3.3 Results

3.3.1 Porewater geochemistry

Figure 3-3a shows how moisture content changed in the fluctuating water table columns at 5 different depths (5, 10, 15, 30, and 40 cm bss): the moisture was highest at 40 cm bss and decreased with increasing proximity to the soil surface (between 40 cm and 5 cm bss). The imposed water

table regime (Figure 3-3b) controlled the soil moisture profile in the fluctuating columns. The redox microsensors at 2 depths (2.5 and 12.5 cm) in SEN1 recorded almost constant redox potentials on the order of 200 and -900 mV, respectively, while the microsensors installed at 3 depths (2.5, 12.5, and-37.5 cm) in FEN1 showed redox potentials oscillating between 700 mV and -600 mV.

Time series data of dissolved naphthalene concentrations for these columns are presented in Figure 3-4 (samples were taken from depths 7.5 cm in FEN1 and SEN1, and at -12.5 cm in FEN2 and SEN2) and Figure A2-1 (samples were taken from depth 22.5 cm bss). The dissolved naphthalene concentration in the two static ethanol/naphthalene columns (SEN1 and SEN2) decreased from 203 μM to 99 μM between days 131 and 280, whereas it dropped from 196 μM to 40 μM in the fluctuating zones in FEN1 and FEN2 (Figure 3-4). These results suggest that naphthalene was degraded faster in the fluctuating columns compared to the static columns because naphthalene fermentation is the dominant naphthalene attenuation mechanism under saturated, anoxic soil conditions, while aerobic degradation increases the rate of naphthalene consumption under oxic soil conditions. However, the increase in naphthalene concentrations in the FEN1 and SEN2 at depth 22.5 cm bss (Figure A2-1) indicates the downward transport of naphthalene in the column. As presented in Figure A2-1, naphthalene concentration in FEN1 is higher than that in SEN2 because WTFs result in naphthalene redistribution in the fluctuating water table soil columns.

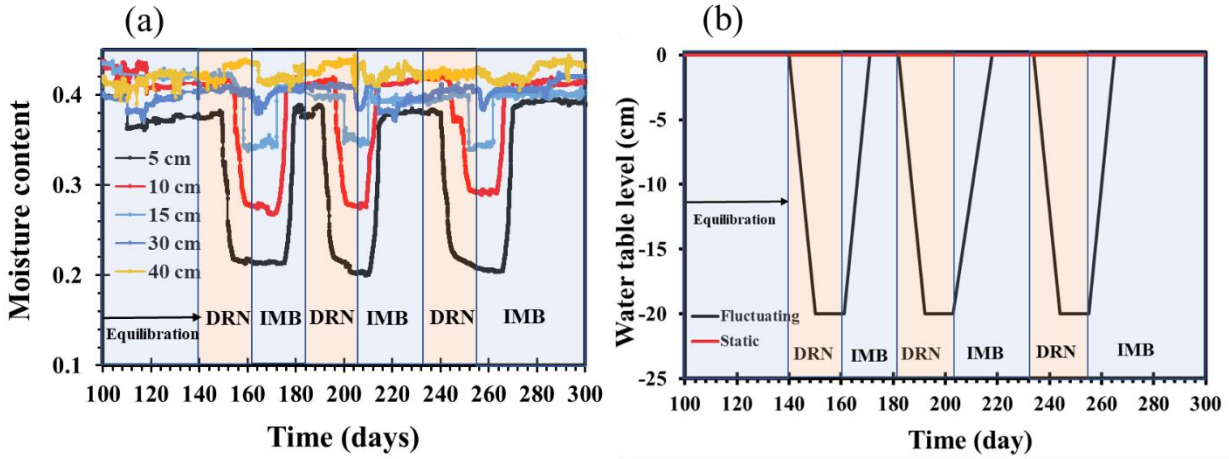

Figure 3-3: (a) Time series data of moisture content at 5 different depths in the fluctuating columns and (b) schematic diagram of the water table levels imposed in the static and fluctuating columns. The blue area shows the imbibition period (IMB) and the pink area represents the drainage period (DRN).

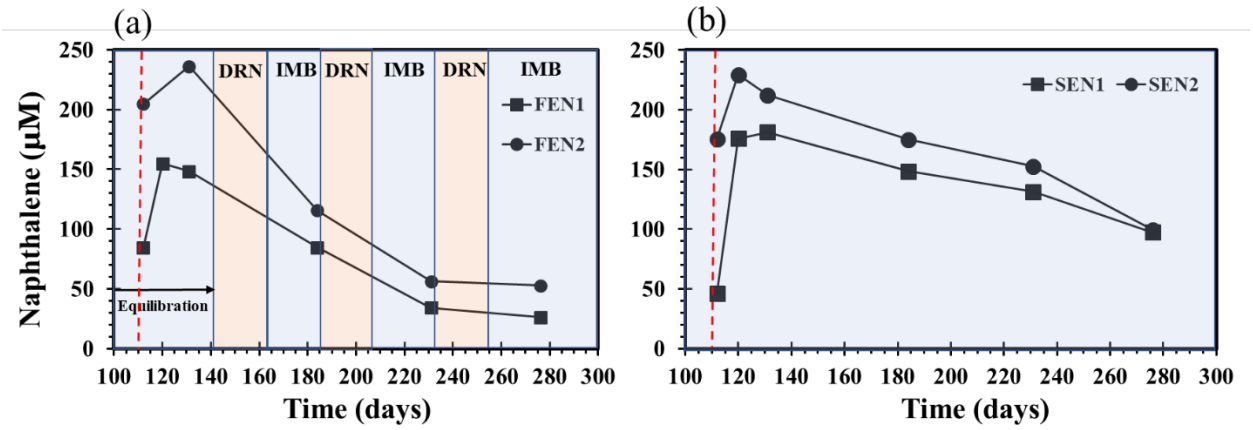

Figure 3-4: Naphthalene concentrations measured at depths 7.5 and 12.5 cm bss in the fluctuating zone (a) FEN1 and FEN2 columns, and (b) SEN1 and SEN2 columns. The red dash-line represents the time at which naphthalene-ethanol solution was injected.

The average DOC concentrations in all soil columns decreased from 2.0 mM to 0.8 mM during the first 111 days because the DOC was consumed by fermentation and sulfate reduction reactions. Following naphthalene/ethanol addition on Day 111, the average DOC concentrations in the naphthalene/ethanol-contaminated soils increased by up to 573 mM due to the presence of ethanol/naphthalene (see Figures 3-5a and 3-5b). Approximately 170 days after the injection, the average DOC concentrations in the fluctuating and static ethanol/naphthalene-contaminated soil columns decreased to 31 mM and 143 mM, respectively (Figures 3-5a and 3-5b). Three main mechanisms explain the higher rate of DOC consumption in the fluctuating water table columns compared to the static water table columns: (1) both anaerobic and aerobic degradation of DOC occur in the fluctuating water table columns, while fermentation reactions are the dominant reactions consuming both ethanol and naphthalene in the static water table columns, (2) the rate of ethanol evaporation in the fluctuating columns is higher than in the static water table columns, which are anoxic, fully saturated, and (3) the rate of acetate production under anoxic condition in the static water table columns is higher than in the fluctuating water table columns.

Following naphthalene/ethanol injection on Day 111, the average DIC concentration in the fluctuating and static soil columns decreased from 6 to 3 mM on Day 140 because CO_2 was probably consumed alongside H_2 for methanogenesis (*i.e.*, for the HBM reaction) after H_2 production was increased by the fermentation of the added naphthalene and ethanol (Figures 3-5c and 3-5d). After Day 140, DIC concentrations increased in the fluctuating columns but did not

increase considerably in the static columns (Figure 3-5c) due to limited O_2 availability and lower CO_2 production. The timeseries data of porewater pH measured in the fluctuating and static water table columns (Figure A2-3a) closely matched the DIC time series trends in the corresponding soil columns, which is unsurprising, as changes in dissolved CO_2 affect both DIC and pH in soils. pH in FEN1, FEN2, and FEC increased following ethanol-naphthalene addition because of CO_2 consumption, while it significantly decreased after lowering the water level due to the increase in dissolved CO_2 (Figure A2-3a). The naphthalene/ethanol injection also affected the soil porewater EC. The timeseries data of EC in the fluctuating and static water table columns are provided in Figure A2-3b.

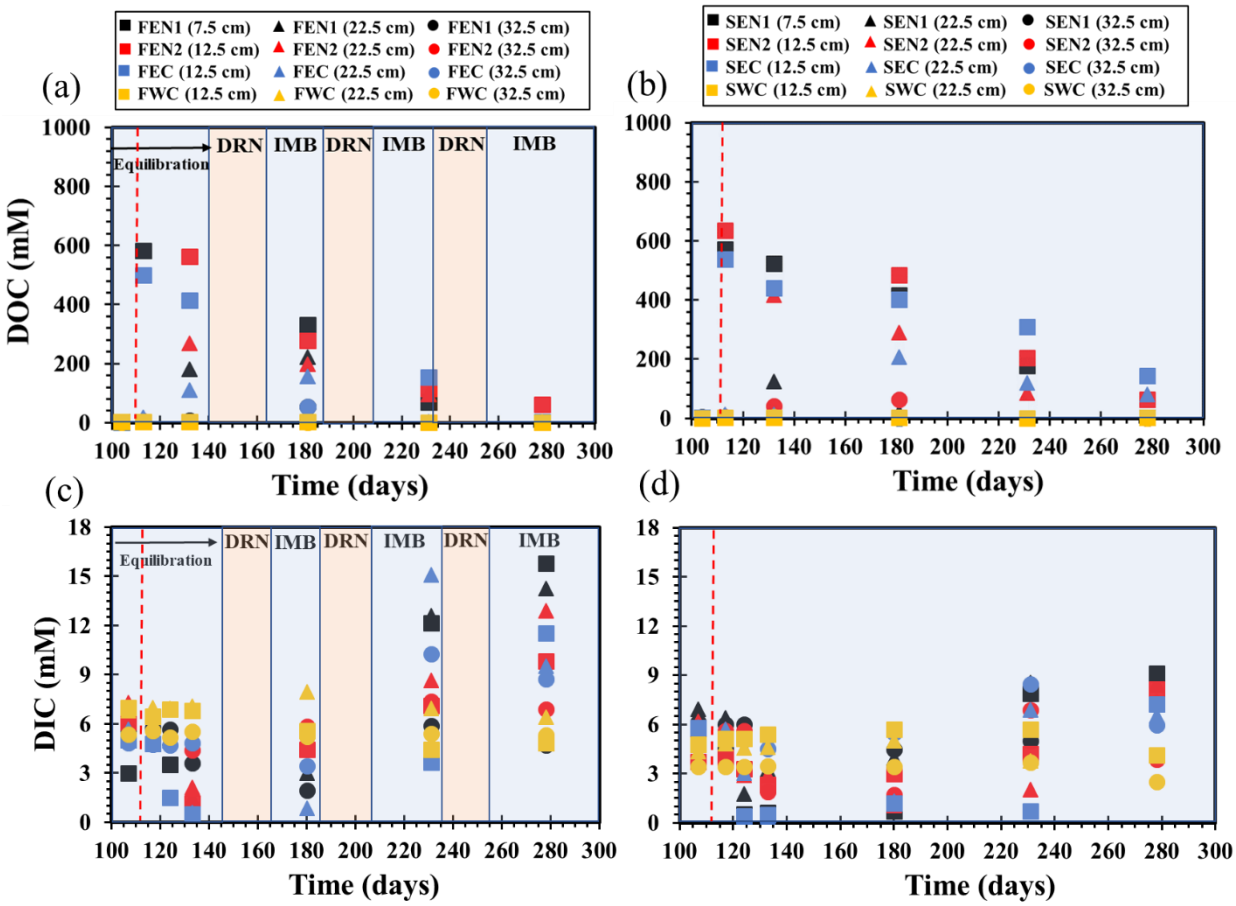

Figure 3-5: Porewater DOC and DIC concentrations measured at depths 2.5, 12.5, 22.5, and 32.5 cm bss in the fluctuating water table columns (a and c) and in the static water table soil columns (b and d). The red dash-line represents the time at which naphthalene-ethanol solution was injected.

The average acetate concentration in the static and fluctuating water table columns decreased from 0.059 mM to 0.006 mM during the first 111 days because acetate was consumed by acetate fermentation, acetate-based methanogenesis (ABM), and acetate oxidation-sulfate reduction reactions in the saturated soil columns (Figure 3-6). Following naphthalene/ethanol addition at Day 111, the average acetate concentration in the static and fluctuating water table columns increased from 0.006 mM to 66 mM and 88 mM, respectively (Figure 3-6). The acetate concentrations in the static water table columns was higher than in the fluctuating water table columns because O_2 acts as a competitive inhibitor to acetogenesis and to the other (fermentation) reactions which produce acetate.

SO_4^{2-} was the only electron acceptor that was available as the other electron acceptors, such as NO_3^- concentrations were very low or not detected. SO_4^{2-} was completely consumed in the ethanol/naphthalene-contaminated soil columns during the first 120 days (Figure A2-2). However, SO_4^{2-} concentration in FWC remained above 0.5 mM at depth 12.5 cm bss because of the limited organic carbon substrate.

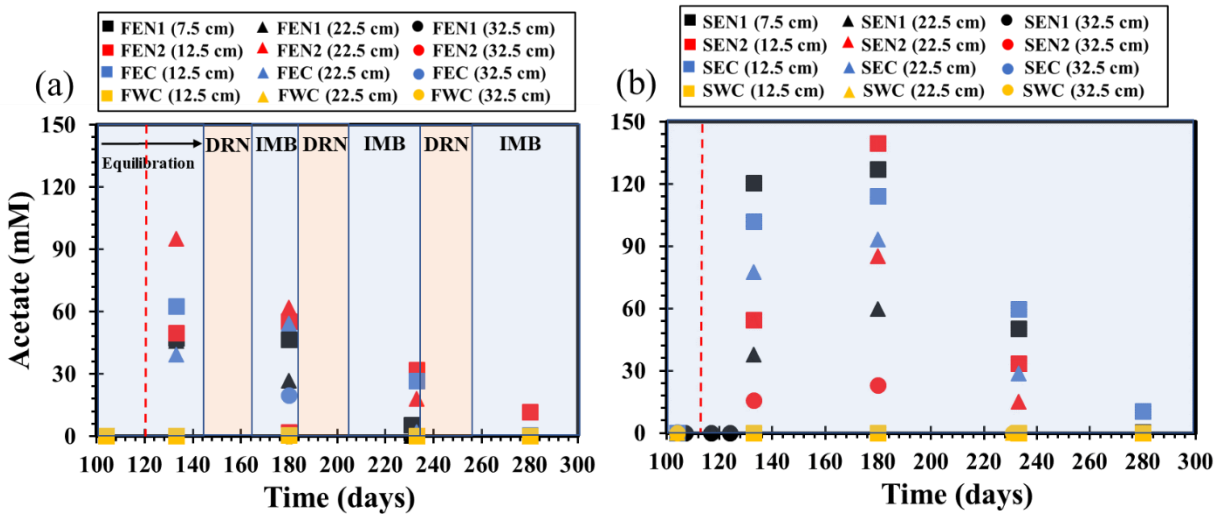

Figure 3-6: Porewater acetate concentrations measured at depths 2.5, 12.5, 22.5, and 32.5 cm bss in the fluctuating water table columns (a), and in the static water table soil columns (b). The red dash-line represents the time at which naphthalene-ethanol solution was injected.

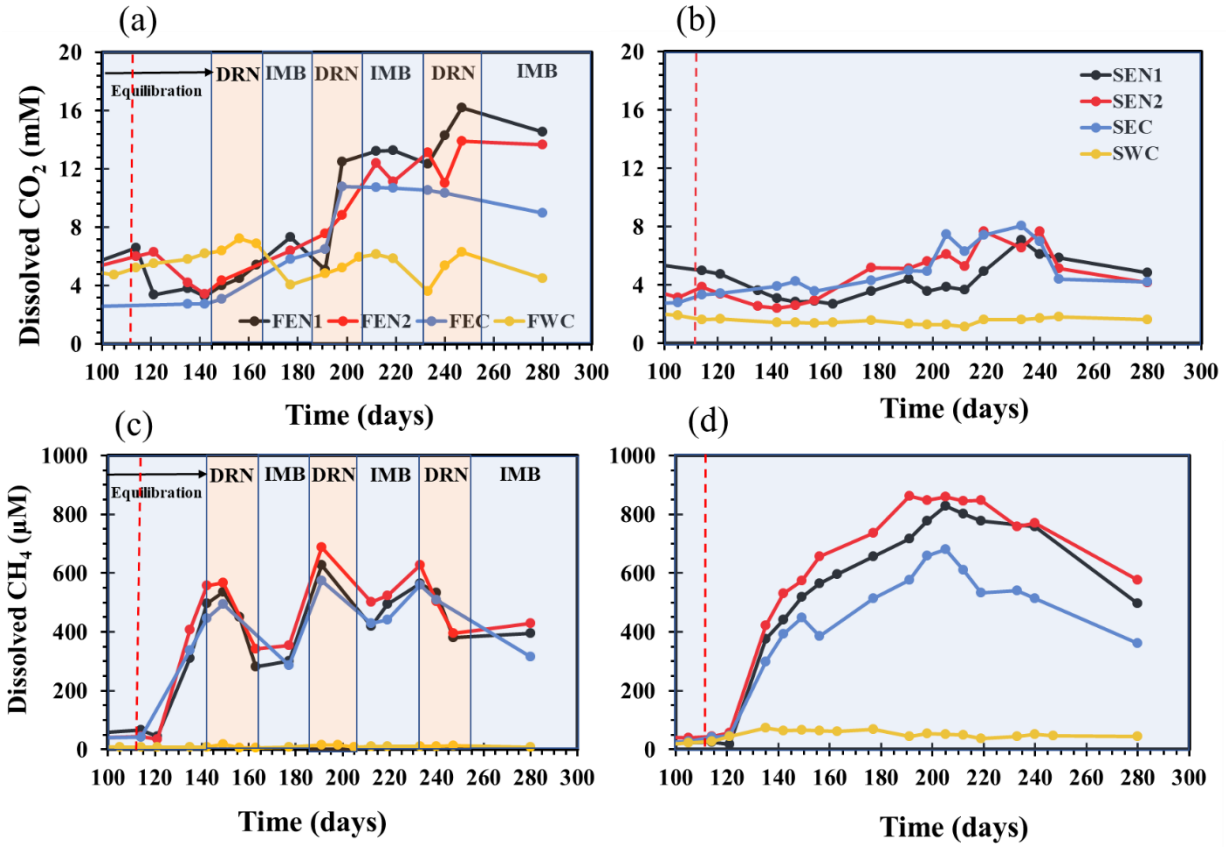

Figure 3-7: Concentrations of dissolved CO_2 and CH_4 measured at depth 22.5 cm bss in the fluctuating water table columns (a and c) and in the static water table soil columns (b and d). The red dash-line represents the time at which naphthalene-ethanol solution was injected.

Dissolved CO_2 and CH_4 concentrations at the depth 22.5 cm bss were measured using the headspace equilibration technique. As shown in Figures 3-7a and 3-7b, the average dissolved CO_2 in the ethanol/naphthalene-contaminated soil columns decreased from 6.3 to 3.4 mM, 30 days after naphthalene/ethanol injection (days 110 to 140), while the dissolved CO_2 in FWC and SWC did not decrease following the naphthalene/ethanol injection. As presented in Figures 3-7c and 3-7d, the average dissolved CH_4 in the ethanol/naphthalene-contaminated soil columns increased to 323 µM between days 110 to 140, while the dissolved CH_4 in FWC and SWC remained less than 10 µM. The observed decrease in CO_2 and simultaneous increase in dissolved CH_4 in the naphthalene/ethanol contaminated soil columns indicate that HBM is probably the prevailing CH_4-producing reaction following the precursor naphthalene and ethanol fermentation reactions. After day 140, the fluctuating water table columns are subjected to 3 successive 6-week cycles of drainage and imbibition. During the lowering of the water table in the first, second, and third

drainage periods, dissolved CO_2 increased by 2.1 mM, 5.9 mM, and 3.1 mM (Figure 3-7a), respectively due to the oxidation of DOC and CH_4. Meanwhile, dissolved CH_4 decreased by 123.1 µM, 244.7 µM, and 139.6 µM, respectively, during the first three drainage periods, because of the release of the dissolved CH_4 during the drainage, the onset of aerobic CH_4 oxidation, and inhibition of methanogenesis in the presence of O_2. However, during the imbibition periods, dissolved CO_2 concentrations decreased (Figures 3-7a and 3-7b), while CH_4 started to accumulate in the saturated soils (Figures 3-7a and 3-7b) because of the increase in the rates of methanogenesis and other anaerobic degradation reactions and the considerable decrease in O_2 concertation.

3.3.2 CO_2 and CH_4 effluxes

The average CH_4 efflux rates in the ethanol/naphthalene contaminated soil columns increased from 0.3 to 71.4 nmol m^{-2} s^{-1} (Figures 3-8c and 3-8d) following naphthalene/ethanol injection, which was matched by 300 µM increase in the dissolved CH_4 concentrations measured at the depth of -22.5 cm (Figures 3-7c and 3-7d). Simultaneously, the average CO_2 fluxes stayed relatively constant at around 0.06 µmol m^{-2} s^{-1} in both the static and fluctuating columns (Figures 3-8a and 3-8b). The observed decrease in CO_2 fluxes and the simultaneous increase in the CH_4 fluxes and dissolved CH_4 concentrations indicate that HBM, which consumes CO2 and produces CH4, is the prevailing methanogenic pathway before day 140. The average CH_4 fluxes in FEN1, FEN2, and FEC during the lowering of the water table in the first, second, and third drainage periods increased to 733, 1249, and 1141 nmol m^{-2} s^{-1}, respectively, due to the release of the accumulated CH_4 (Figure 3-8c). As presented in these figures, CH_4 fluxes started decreasing about two weeks after the start of the drainage periods. Although the water table level remained constant (at a depth of 20 cm bss) in all the fluctuating columns for 2 weeks, the decrease in CH_4 flux is possibly explained by CH_4 oxidation and the inhibition of methanogenesis by O_2. Figure 3-8a shows a continuous increase in CO_2 fluxes during the first, second, and third drainage periods from 0.06 µmol m^{-2} s^{-1} to 0.65, 1.23, and 1.54 µmol m^{-2} s^{-1}, respectively because of the release of accumulated dissolved CO_2 and the aerobic degradation of DOC and CH_4.

During the first, second, and third imbibition periods, the average CH_4 flux in FEN1, FEN2, and FEC (Figure 3-8c) decreased to 208, 115, and 77 nmol m^{-2} s^{-1}, respectively due to limited upward diffusion during the raising of the water table. Following the end of the imbition period, the CH_4

flux then statrted increasing (following the end of all 3 imbibition periods) because of the higher rate of methanogenesis in the saturated conditions compared to the unsaturated conditions. The average CO_2 fluxes in the fluctuating columns during the first, second, and third imbibition periods decreased to 0.25, 0.30, and 0.19 µmol m^{-2} s^{-1} (Figure 3-9a) because the most available carbon substrate has already been degraded in the first drainage-imbibition period. CO_2 and CH_4 fluxes reached higher peaks in the second drainage period (Figures 3-8a and 3-8c) because of higher accumulated dissolved CO_2 and CH_4 concentrations in the second drainage compared to the first drainage period.

It should be noted that CH_4 efflux rates in the SWC column did not change considerably because this soil column was always fully saturated and there was no ethanol/naphthalene added. CO_2 and CH_4 fluxes in SEN1, SEN2, and SEC have an upward trend after day 140 (Figures 3-9b and 3-9d) because of anaerobic degradation of ethanol/naphthalene, and consequent CO_2 and CH_4 production in the anoxic, saturated soils. Compared with the gas effluxes for the fluctuating columns, the CO_2 and CH_4 effluxes measured in the static, ethanol/naphthalene spiked soil columns changed at a slower pace over the course of the experiment. Because methanogenesis was the dominant biodegradation pathway for naphthalene (and ethanol) in these columns, CH_4 effluxes increased monotonically between days 110 and 180. CO_2 and CH_4 fluxes remained lower than 0.45 µmol m^{-2} s^{-1} and 250 nmol m^{-2} s^{-1}, respectively because of limited upward diffusion in the saturated soils (Figures 3-8b and 3-8d).

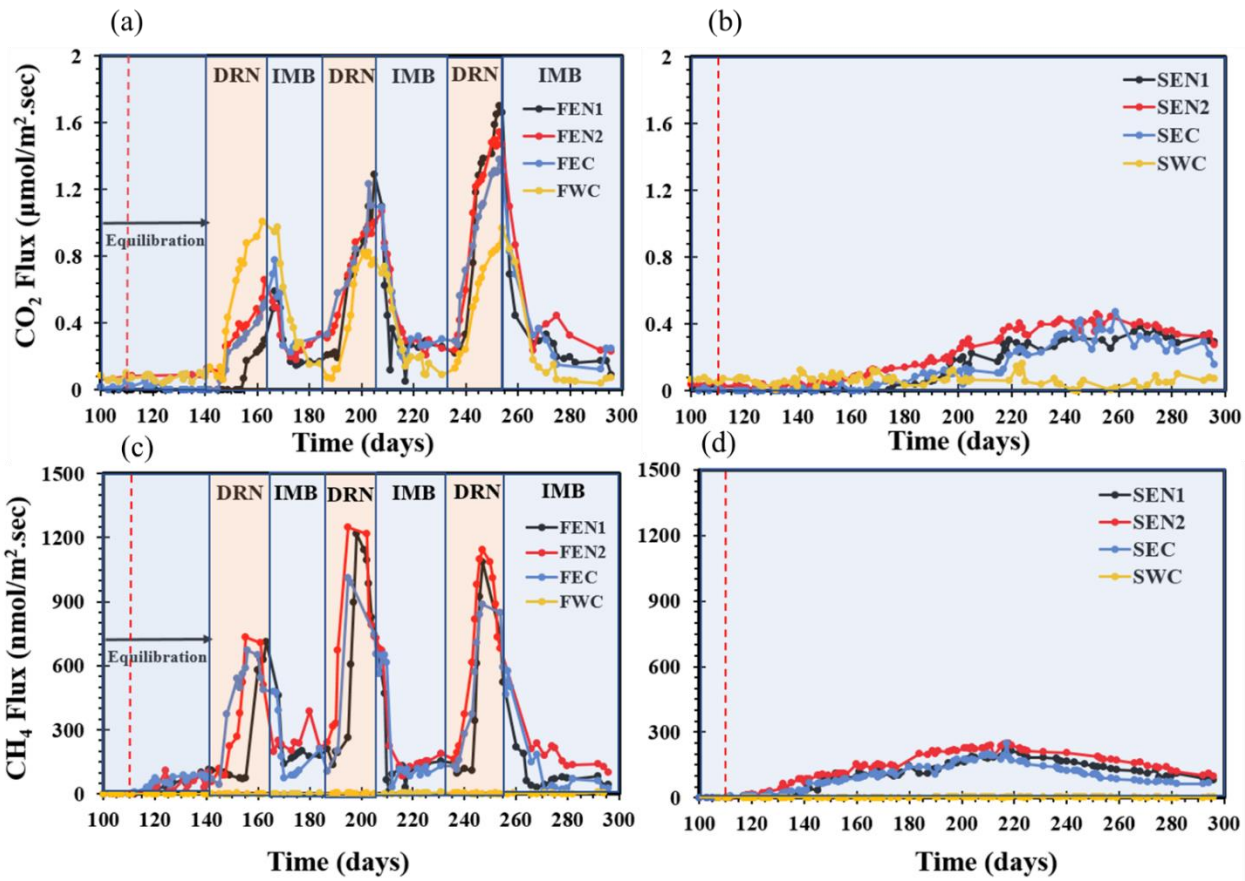

Figure 3-8: Soil surface CO_2 and CH_4 effluxes from the fluctuating water table columns (a and c) and the static water table soil columns (b and d). The red dash-line represents the time at which naphthalene-ethanol solution was injected.

3.3.3 Methanogenic pathways

To visualize and differentiate between the metabolic pathways controlling the production and/or consumption of dissolved CH_4 (and CO_2) concentrations, $\delta^{13}C$ - CO_2 was plotted against $\delta^{13}C$ - CH_4 (Figures 3-9a, 3-9b, and 3-9c) following the approach of Whiticar (2020). In these figures, the blue and green areas represent the HBM and ABM metabolic domains, respectively, and the pink area represents the CH_4 oxidation metabolic domain. HBM is the prevailing methanogenic pathway in the ethanol/naphthalene contaminated soil columns before day 130 (Figures 3-9a and 3-9b). Then, the dominant methanogenic pathway shifted to ABM due to the increase in acetate and decrease in the dissolved CO_2. CH_4 oxidation in the fluctuating columns became the prevailing metabolic pathway contributing to the $\delta^{13}C$-CH_4 isotope composition after the first drainage period

(*i.e.*, after day 165) (Figures 3-9a and 3-9c), whereas ABM was the dominant metabolic pathway controlling dissolved CH_4 concentration in the static columns after day 130.

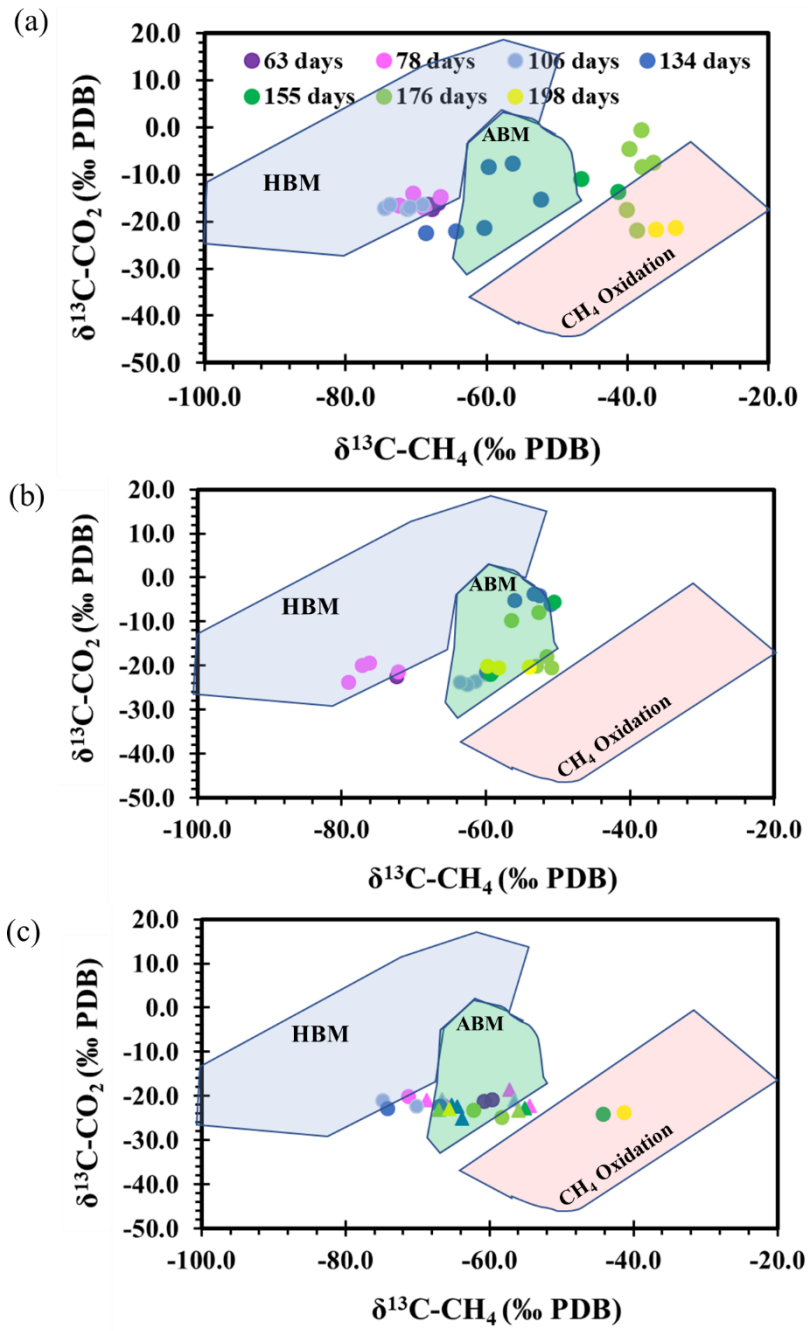

Figure 3-9: $\delta^{13}C$-CO_2 versus $\delta^{13}C$-CH_4 in (a) FEN1, FEN2, and FEC, (b) SEN1, SEN2, and SEC, and (c) FWC and SWC.

3.3.4 Simulation

Simulation were performed for the FEN1, FEN2, SEN1, and SEN2 columns only. Figure 3-10 shows soil moisture content obtained by the model and the experiment in the fluctuating columns. As shown in these figures, the model is able to mimic the variations in moisture content during WTFs. In this model, the variations in moisture content affect the CO_2 and CH_4 effluxes (Figure 3-11a) because the ability of gas components (*e.g.*, CH_4, CO_2, and O_2) to transport within the pore spaces is a function of moisture content according to Eqs. 3-1 to 3-3.

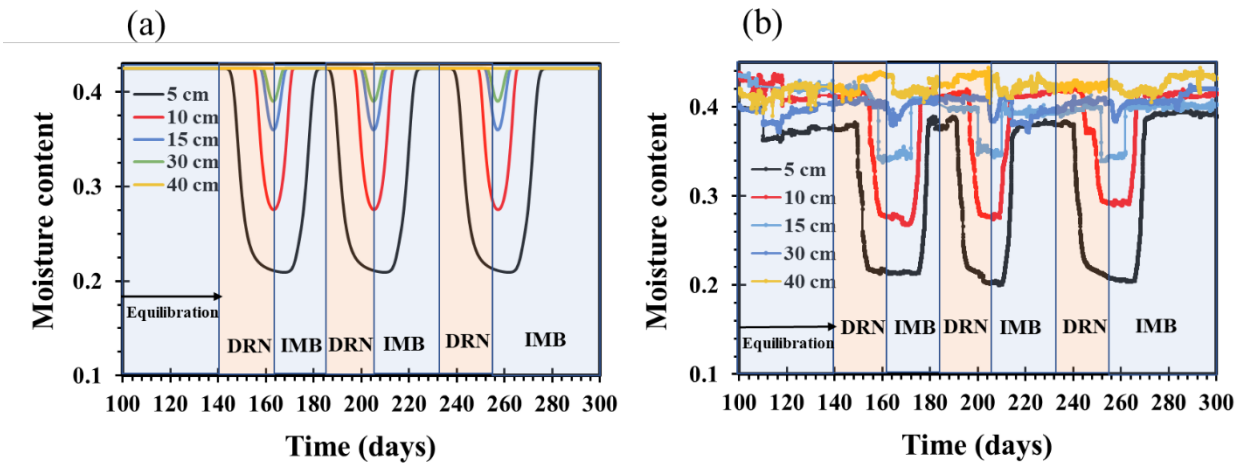

Figure 3-10: Moisture contents at 5 different depths (a) simulated, (b) measured in the column experiment.

The simulated CO_2 and CH_4 fluxes for the FEN and SEN columns are in agreement with the fluxes measured in the experiment (Figure 3-11). The variations in moisture content and relative permeability of gas components affect soil surface effluxes and the dissolved concentrations of CO_2 and CH_4 (Figure 3-12) because of three main mechanisms in this model: (1) O_2 can act as an inhibitor for the anaerobic reactions according to Eq. 3-9, (2) O_2 increases the rates of aerobic reactions producing dissolved CO_2 according to the reaction network used in this model (Table 3-1), (3) dissolved CO_2 and CH_4 concentrations decrease with CO_2 and CH_4 effluxes in this model. As shown in Figure 3-12, the model-predicted dissolved CO_2 and CH_4 agrees with that obtained from the experiment.

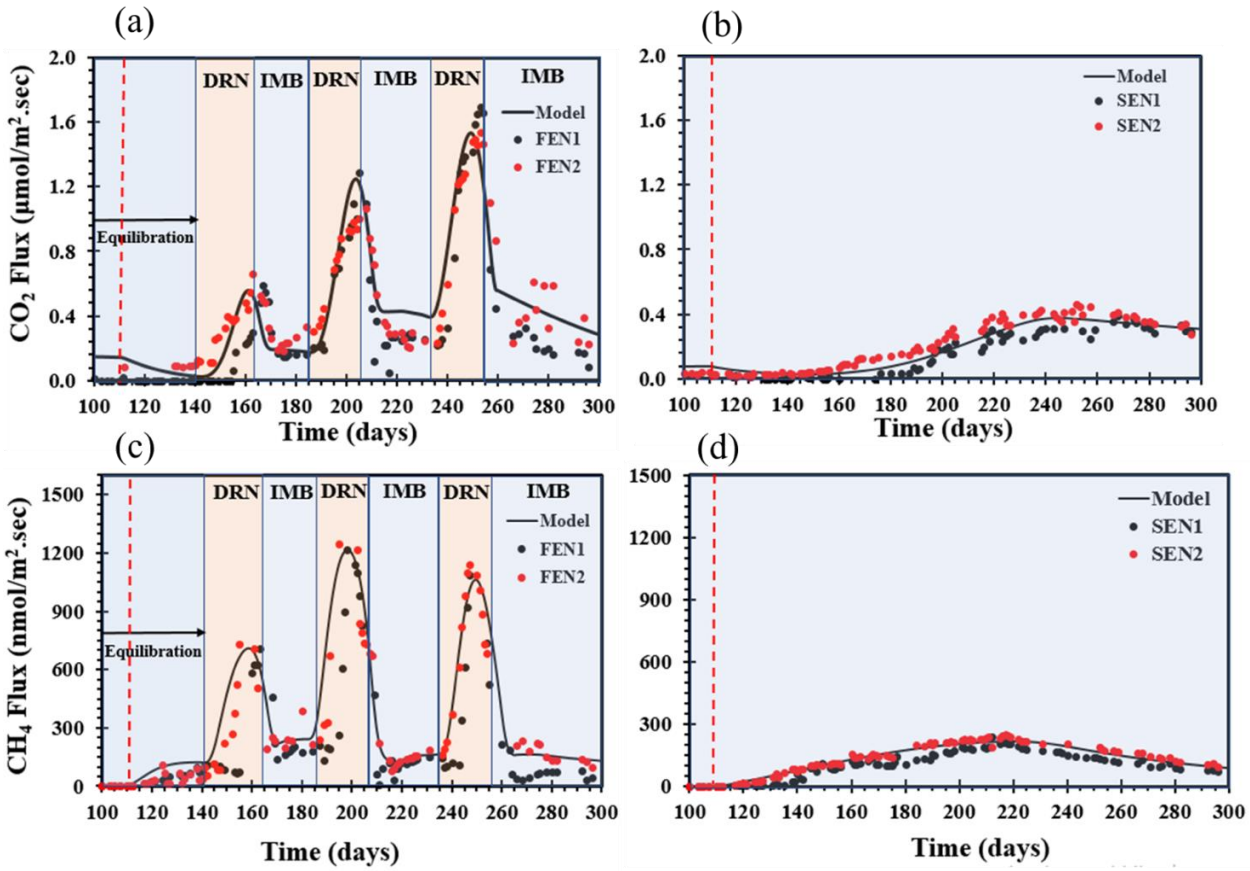

Figure 3-11: Experimental (points) and simulation (lines) results of soil surface CO_2 and CH_4 effluxes for the fluctuating water table columns FEN1 and FEN2 (a and c) and the static water table columns SEN1 and SEN2 (b and d). The red dash-line represents the time at which naphthalene-ethanol solution was injected.

The model was able to closely match the DIC changes in both the FEN and SEN columns (Figures 3-13a and 3-13b), confirming that the reaction network used in the simulations represents the reactions that produce and consume DIC (*e.g.*, ABM, HBM, ethanol/naphthalene oxidation). Also, Figures 3-13c and 3-13d shows that the simulation results of DOC in FEN and SEN agrees with experimental data because the main components and chemical reactions determining DOC concentrations were considered in this model (*i.e.*, DOC includes glucose, acetate, ethanol, and naphthalene as presented in Table 3-1). Naphthalene is one of the DOC components consumed due to naphthalene fermentation and aerobic oxidation reactions. The model successfully simulated the impact of moisture dynamics on naphthalene concentrations (Figure 3-14). Acetate is another component of DOC that produced/consumed because of acetogenesis, ABM, and other

fermentation reactions in this model (Table 3-1). Figure 3-15 shows the model can successfully predict the changes in acetate concentration after naphthalene/ethanol injection in the FEN and SEN soil columns.

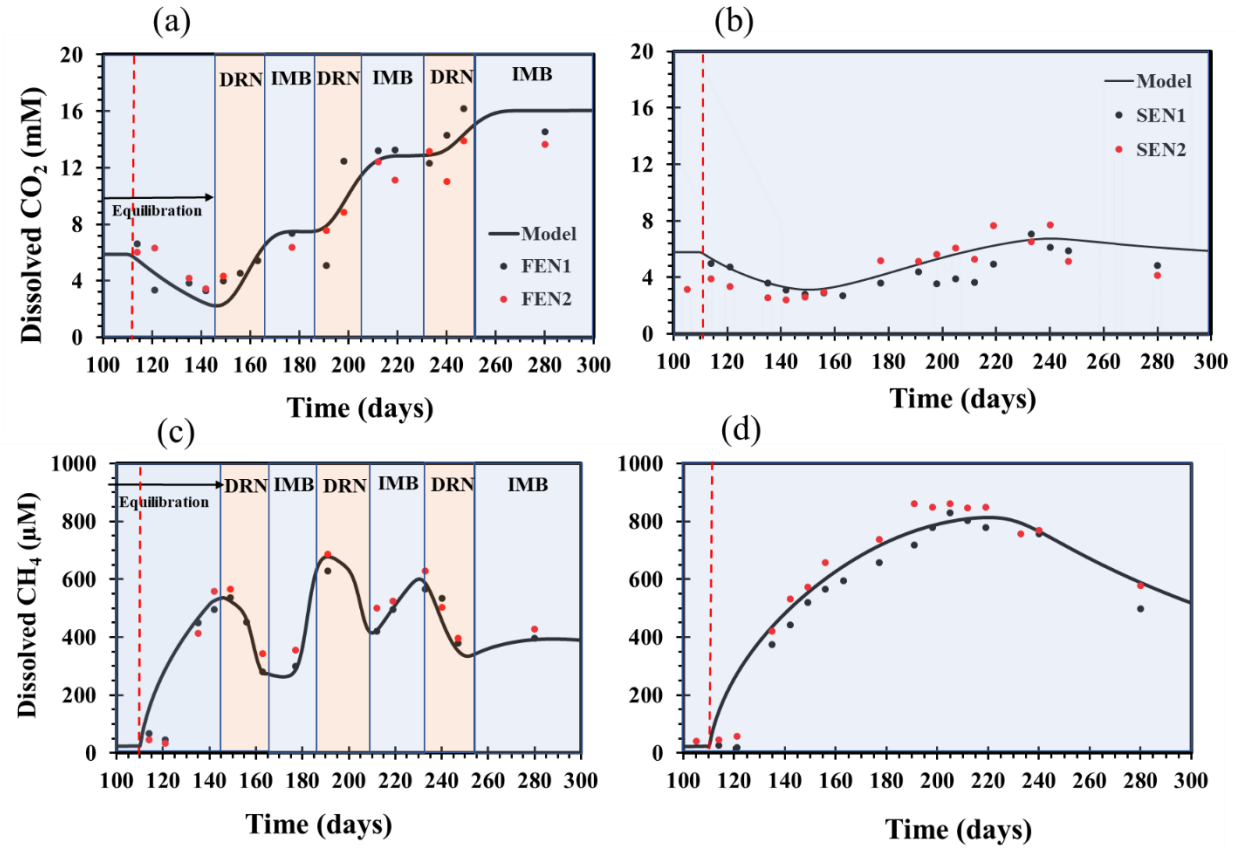

Figure 3-12: Experimental (points) and simulation (lines) results of dissolved CO_2 and CH_4 concentrations for the fluctuating water table columns FEN1 and FEN2 (a and c), and the static water table soil columns SEN1 and SEN2 (b and d). The red dash-line represents the time at which naphthalene-ethanol solution was injected.

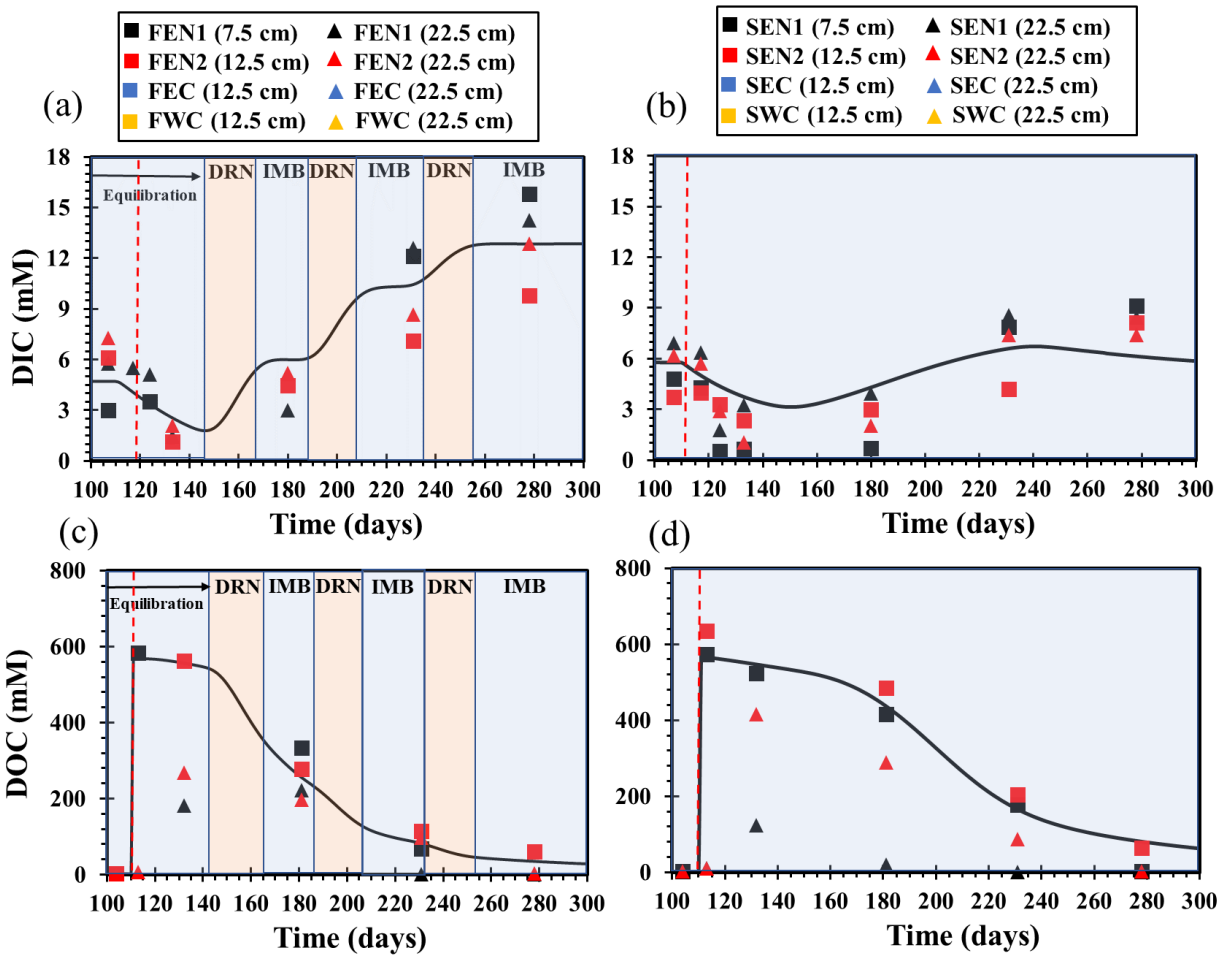

Figure 3-13: Experimental and simulation results of DIC and DOC concentrations in the fluctuating water table columns FEN1 and FEN2 (a and c) and the static water table soil columns SEN1 and SEN2 (b and d). The red dash-line represents the time at which naphthalene-ethanol solution was injected.

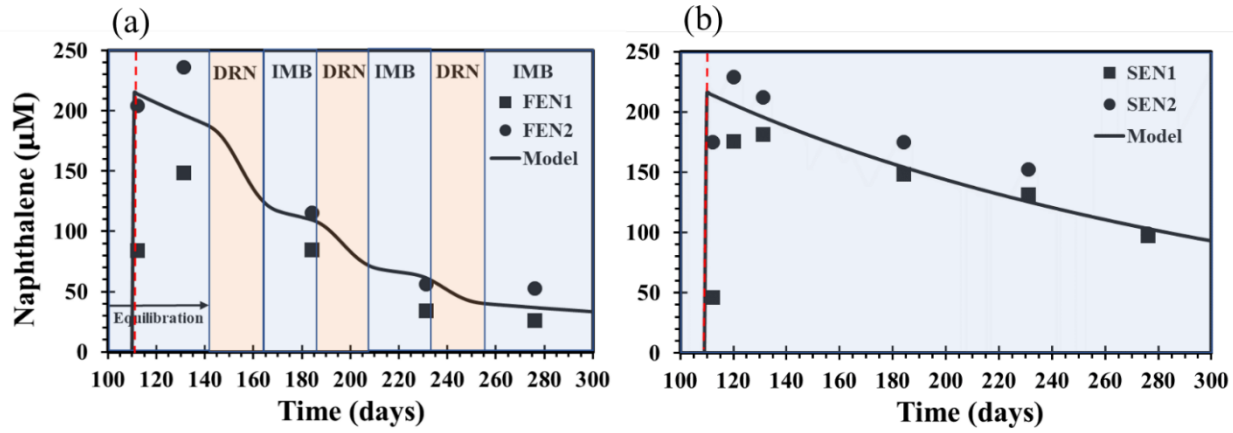

Figure 3-14: Experimental and simulation results of naphthalene concentrations in (a) the fluctuating columns FEN1 and FEN2, (b) and the static columns SEN1 and SEN2 (b). The red dash-line represents the time at which naphthalene-ethanol solution was injected.

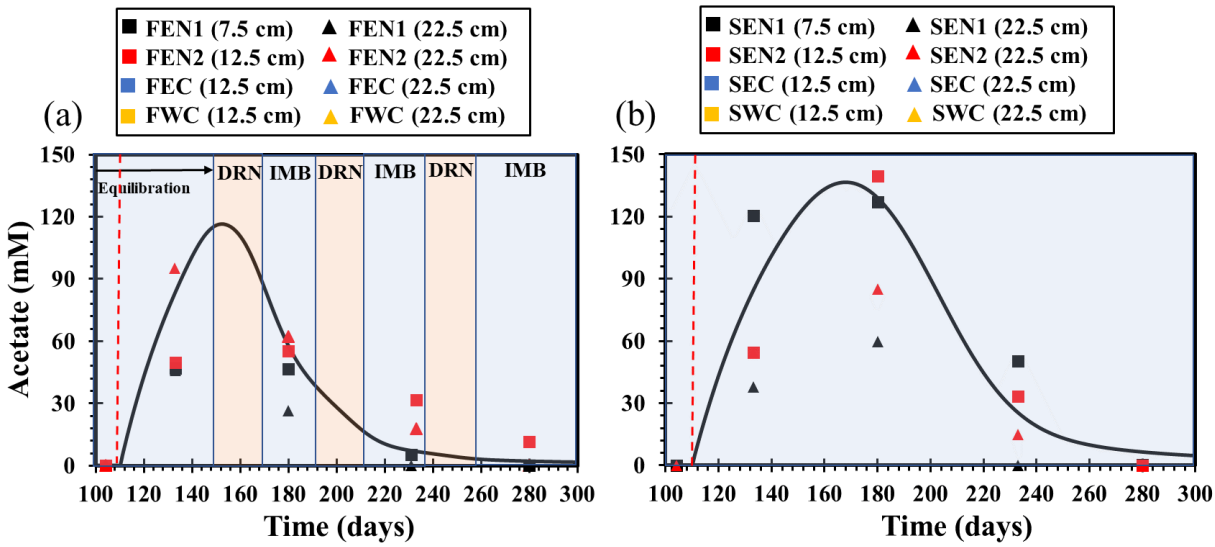

Figure 3-15: Experimental and simulation results of acetate concentrations in (a) the fluctuatinc columns FEN1 and FEN2, and (b) the static columns SEN1 and SEN2. The red dash-line represents the time at which naphthalene-ethanol solution was injected. The red dash-line represents the time at which naphthalene-ethanol solution was injected.

3.4 Discussion

The results show that naphthalene degradation and CO_2 and CH_4 effluxes are strongly influenced by moisture content. The imposed water table fluctuations in the soil column caused variations in moisture content, dissolved CO_2 and CH_4, the relative rates of aerobic and anaerobic biodegradation reactions as well as gas transport processes in soils.

3.4.1 Impact of WTFs on naphthalene degradation

The average naphthalene concentrations in the 22.5 cm bss (*i.e.*, the zone of water table fluctuation in the fluctuating columns) decreased 1.5-times more in the fluctuating (FEN1 and FEN2) than in the static (SEN1 and SEN2) columns (Figure 3-4) because aerobic degradation increases the rate of net naphthalene degradation in the fluctuating columns compared to the static columns, where the much slower naphthalene fermentation is the dominant degradation pathway (Figure 3-16). The increase in dissolved naphthalene concentrations in the saturated zone (32.5 cm bss) by 15 μM in FEN1 (Figure A2-1) indicate that WTFs also cause downward transport and the redistribution of naphthalene in the column. As presented in Figure A2-1, naphthalene concentration in FEN1 is higher than that in SEN2 because WTFs result in the redistribution of naphthalene in the fluctuating water table columns.

The average DOC concentrations in the fluctuating and static ethanol/naphthalene-contaminated soil columns decreased by 95% and 75%, respectively (Figures 3-5a and 3-5b) because evaporation and aerobic degradation of DOC components, especially ethanol and naphthalene increase the rate of DOC consumption in the fluctuating columns (Figure 3-16). The other reason is that the average acetate concentration in the static columns is higher than in the fluctuating columns (Figure 3-6) because O_2 acts as a competitive inhibitor and reduces the rate of acetogenesis and other fermentation reactions producing acetate in the soil columns (Figure 3-16). The rate of acetate production also depends on the concentration of dissolved H_2, which is a by-product of some anaerobic degradation reactions.

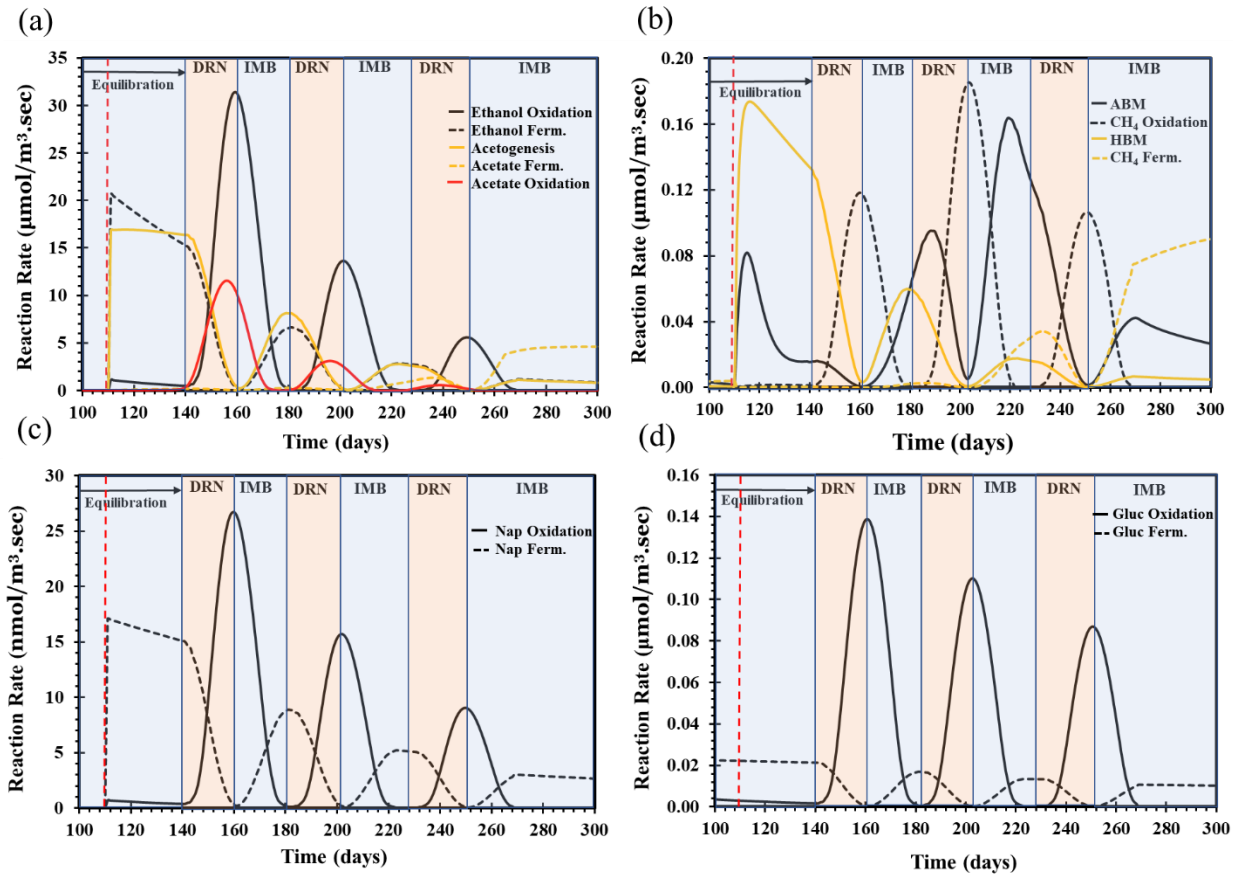

Figure 3-16: Simulation results of the rates of (a) ethanol oxidation, ethanol ferm (ethanol fermentation), Acetogenesis, acetate fermentation, and acetate oxidation, (b) the rates of acetate-based methanogenesis (ABM), hydrogen-based methanogenesis (HBM), methane fermentation, and methane oxidation, and (c) the rates of naphthalene oxidation and fermentation, and (d) the rates of glucose oxidation and fermentation reactions.

3.4.2 Impact of WTFs on CO_2 and CH_4 effluxes

The average dissolved CO_2 in the fluctuating and static ethanol/naphthalene-spiked columns decreased by 46%, 30 days after naphthalene/ethanol injection, while the dissolved CO_2 in FWC column increased by 19% (Figures 3-7a and 3-7b). Simultaneously, the average dissolved CH_4 increased by 323 µM, while the dissolved CH_4 in FWC and SWC columns remained less than 10 µM (Figures 3-7c and 3-7d). The observed decrease in CO_2 and simultaneous increase in dissolved CH_4 in the naphthalene/ethanol contaminated soil columns (days 110 to 140) indicate that HBM is probably the prevailing CH_4-producing reaction following the precursor naphthalene and ethanol fermentation reactions. During water table lowering, the average dissolved CO_2 increases by 105% (Figure 3-7a) due to the oxidation of DOC and CH_4, while dissolved CH_4 decreases by 29% (Figure 3-7c) because of CH_4 oxidation and inhibition of methanogenesis in the presence of O_2. However, during imbibition, dissolved CO_2 concentration is reduced (Figure 3-7a), while CH_4 is accumulated because of the increase in the rates of methanogenesis and other anaerobic degradation reactions and the decrease in the rates of aerobic degradation (Figure 3-16). The changes in dissolved CO_2 controlled DIC and pH in the soil columns, and hence pH and DIC closely matched CO_2 trends in the corresponding soil columns.

The average CH_4 fluxes in the ethanol/naphthalene spiked soil columns increased by 71.1 nmol m^{-2} s^{-1} about one month after naphthalene/ethanol injection (see Figures 3-8c and 3-8d), which corresponded to an increase in the dissolved CH_4 concentration at 22.5 cm bss (Figures 3-7c and 3-7d). The observed increase in CH_4 fluxes and dissolved CH_4 concentrations and simultaneous decrease in dissolved CO_2 (Figures 3-8a and 3-8b) indicate that HBM is the prevailing methanogenic pathway before the start of drainage-imbibition cycles. During the lowering of the water table, the average CH_4 and CO_2 fluxes increased by up to 10 times (Figure 3-8) due to the release of the accumulated dissolved CH_4 and CO_2. When the water level remained constant at 20 cm bss, CH_4 fluxes started to decrease because of aerobic CH_4 oxidation, while CO_2 fluxes continuously increased because of the release of the dissolved CO_2 and the aerobic degradation of DOC and CH_4. During imbibition periods, the average CH_4 and CO_2 fluxes returned to baseline conditions (Figures 3-8a and 3-8c) due to limited upward diffusion, and then CH_4 started increasing because of the higher rates of methanogenic reactions in the saturated, largely anoxic, soil compared to the unsaturated, largely oxic, soil during the drainage periods. CO_2 and CH_4

fluxes reached higher peaks in the second drainage period (Figures 3-8a and 3-8c) because of higher dissolved CO_2 and CH_4 in the second drainage compared to the first drainage period.

3.4.3 Impact of WTFs on methanogenic pathway

As discussed above, the results of CO_2 and CH_4 indicated that HBM is probably the prevailing CH_4-producing reaction during the first 140 days of the experiment, and the methanogenic pathway shifted to ABM and CH_4 oxidation after day 140. The changes in the methanogenic pathways HBM and ABM over time during the experiment were identified using isotopic analyses. The results of $\delta^{13}C$ compositions of dissolved CO_2 and CH_4 (Figure 3-9) confirms that HBM is the prevailing methanogenic pathway in the ethanol/naphthalene spiked soil columns before day 130 because H_2 and CO_2 as byproducts of DOC fermentation accumulate in the system. Then, the dominant methanogenic pathway shifted to ABM between days 130-180 due to CO_2 consumption and H_2 depletion, which occurs when the rate of H_2 consumption is greater than its rate of production. In contrast, the rate of ABM increases over time because acetate concentration increases due to acetogenesis and DOC fermentation. After day 180, $\delta^{13}C$-CH_4 became less negative, and CH_4 oxidation and ABM became the prevailing pathways in the fluctuating columns because of the microbial oxidation of CH_4 that can take place due to O_2 availability. The model also successfully predict the switch from HBM to ABM in the fluctuating columns as presented in Figure 3-16 b.

3.4.4 Model performance

The model's successful simulation of the experimental time series trends in porewater chemistry and surface gas effluxes indicates that the biogeochemical reaction network captures the most important reactions and that the transport component of the model successfully simulates the impact of water table fluctuations on soil moisture content, and then, in turn, the effect of soil moisture content on gas effective diffusion coefficients. Although the effect of soil moisture content on reaction rates is not represented explicitly using a soil moisture function, like in Ghezzehei *et al*. (2019) and Moyano *et al*. (2013), the effect of soil moisture on O_2 ingression into the porewater is represented, and the O_2 concentration then regulates the competition between aerobic and anaerobic pathways via inhibition terms. This modeling framework can also be used

to simulate the impact of any water table fluctuations or moisture content variations on PHC NSZD processes at contaminated sites.

3.5 Summary and Conclusions

A ten month-long soil column experiment and simulated the experimental results using a diffusion-reaction model including 12 microbial reactions and multicomponent solute transport to better understand how WTFs modulate soil geochemistry, methanogenic naphthalene biodegradation and CO_2 and CH_4 effluxes in PHC-contaminated soils. In the column experiment, 4 soil columns were subjected to 3 successive 3-week cycles of drainage (20 cm bss) and imbibition (0 cm bss), whereas in 4 static columns, the soil cores remained saturated. Based on the results obtained in this study, the following conclusions can be drawn:

- The observed decrease in CO_2 concentrations and simultaneous increase in dissolved CH_4 in the saturated naphthalene/ethanol contaminated soil columns indicated that HBM is probably the prevailing CH_4-producing reaction following the precursor naphthalene and ethanol fermentation reactions.
- During drainage periods, the average dissolved CO_2 increased by 105% due to the aerobic oxidation of DOC and CH_4, while the average dissolved CH_4 decreased by 29% because of CH_4 oxidation and inhibition of methanogenesis in the presence of O_2.
- Rewetting following drainage reduced dissolved CO_2 and increased accumulated CH_4 because of the increase in the rates of methanogenesis and other anaerobic degradation reactions and the decrease in the rates of aerobic degradation in saturated soils.
- During drainage periods, the average CH_4 and CO_2 fluxes increased up to 10 times in the ethanol/naphthalene spiked soils due to the release of the accumulated CH_4 and CO_2, and then CH_4 fluxes started to decrease because of aerobic CH_4 oxidation, while CO_2 fluxes continuously increased due to the aerobic degradation of DOC and CH_4. However, the average CH_4 and CO_2 fluxes dropped considerably due to limited upward gas diffusion during imbibition.
- The average porewater DOC in the fluctuating and static ethanol/naphthalene-contaminated soil columns decreased by 95% and 75%, respectively because evaporation

and aerobic degradation of DOC components, especially ethanol and naphthalene, increased the rate of DOC consumption in the fluctuating columns.

- The average naphthalene concentrations dropped by 80% and 51% in the fluctuating and static soil columns, respectively. Also, the increase in naphthalene concentration below the water level in the fluctuating columns indicated that drainage-imbibition cycles also cause downward transport of naphthalene in the column.
- The results of $\delta^{13}C$ compositions of dissolved CO_2 and CH_4 confirmed that HBM is the prevailing methanogenic pathway in the saturated ethanol/naphthalene spiked soil columns because H_2 and CO_2 as by-products of DOC fermentation accumulate in the system. Then, the dominant methanogenic pathway shifted to ABM due to CO_2 consumption, H_2 depletion, and acetate production. After one drainage-imbibition cycle, $\delta^{13}C$-CH_4 became less negative, and CH_4 oxidation became the prevailing pathway in the fluctuating columns because of aerobic microbial CH_4 oxidation.
- The model successfully reproduced the experimental time series trends in porewater chemistry and surface gas effluxes, indicating that the model captured the most important processes.

4 Conclusions and Future Research

4.1 Summary of key findings

The overall objective of this thesis was to advance understanding of how freeze-thaw cycles (FTCs) and water table fluctuations (WTFs) control methanogenic petroleum hydrocarbon (PHC) biodegradation and CO_2 and CH_4 fluxes in soils contaminated by petroleum products. In Chapter 2, I aimed to delineate the effects of FTCs on methanogenic toluene biodegradation and CH_4 and CO_2 generation. In Chapter 3, the main objective was to investigate the effects of WTFs on soil geochemistry, naphthalene biodegradation, and CH_4 and CO_2 soil efflux rates.

In Chapter 2, a 215 day-long incubation experiment was conducted and the experimental results were simulated using a diffusion-reaction model which included 11 microbial reactions, toluene sorption/desorption, and gas diffusion to better understand how FTCs modulate soil geochemistry, methanogenic toluene biodegradation, and CO_2 and CH_4 production. In the batch experiment, we imposed anoxic, saturated conditions and 5 successive FTCs where the temperature fluctuated from -10°C to +15°C. I also developed a biogeochemical model representing the impacts of temperature on microbial reaction rates and gas diffusion rates.

The experimental results showed that toluene addition to the incubations increased CO_2 and CH_4 concentrations in all three treatments relative to the NT (no lactate added) incubations. The cumulative CO_2 and CH_4 generation increased by 136% and 87%, respectively, in the NL-TA (no lactate added-toluene amended) treatment, by 117% and 61%, respectively in the LA-TA (lactate amended-toluene amended) treatment, and by 50% and 33% in the BES-TA (2-bromoethanesulfonate (BES) amended-toluene amended) treatment. We predicted this in the model by representing toluene fermentation, acetogenesis, hydrogen-based methanogenesis, and acetate-based methanogenesis as separate reactions.

Moreover, the results of this experiment demonstrate that the average fraction of ABM (Acetate based methanogenesis) contributing to methane production in the model was around 75%, and the ABM fraction calculated from the $\delta^{13}C$-CO_2 and -CH_4 results agreed with this. The model confirmed that methanogenic toluene degradation is the dominant toluene attenuation mechanism, representing 74% of the attenuation, with sorption contributing to 11%, and evaporation

contributing to 15%, which demonstrates that methanogenic toluene biodegradation (in anoxic soil, in the absence of electron acceptors) can contribute to natural toluene attenuation.

In the modeling component of this study, the biogeochemical model represented the impacts of temperature on microbial reaction rates and gas diffusion rates and predicted the near-zero rates during the -10°C freezing periods by applying temperature functions to the calculation of the maximum rate constants and effective diffusion coefficients, respectively. The model successfully reproduced the experimental time series trends in porewater chemistry and headspace gas concentrations, indicating that the biogeochemical reaction network captures the most important reactions. Moreover, representing the effects of FTCs on porewater dissolved organic carbon (DOC) production due to freezing-induced soil matrix disturbance was key for accurately simulating DOC concentrations as well as CO_2 and CH_4 generation. In addition to the FTC scenario, I simulated a scenario with no FTCs imposed. The results of this model showed that CO_2 and CH_4 generation are 29% and 26% lower, respectively than in the FTC condition because less DOC is produced in the no FTC scenario, whereas toluene biodegradation is 23% faster in the no FTC scenario. Hence, the no FTC scenario showed that FTCs slow down toluene degradation while enhancing CO_2 and CH_4 production, which is a less preferred outcome for contaminated site remediation.

In Chapter 3, a ten month-long column experiment was conducted and the experimental results were simulated using a diffusion-reaction model which included 12 microbial reactions and multicomponent solute transport to better understand how WTFs modulate soil porewater geochemistry, methanogenic naphthalene biodegradation and CO_2 and CH_4 effluxes. In the column experiment, 4 soil columns were subjected to 3 successive 3-week cycles of drainage (20 cm bss) and imbibition (0 cm bss), whereas in 4 static columns, the soil cores remained saturated.

The experimental results demonstrated that the observed decrease in CO_2 concentration and simultaneous increase in dissolved CH_4 in the saturated ethanol/naphthalene contaminated soil columns indicate that HBM (Hydrogen based methanogenesis) is probably the prevailing CH_4-producing reaction following the precursor naphthalene and ethanol fermentation reactions. Also, during lowering the water table, the average dissolved CO_2 increases by 105% due to the oxidation of DOC and CH_4, while the average dissolved CH_4 decreases by 29% because of CH_4 oxidation

and inhibition of methanogenesis in the presence of O_2. The results also showed that rewetting contaminated soils reduces dissolved CO_2 and increase accumulated CH_4 in soil because of the increase in the rates of methanogenesis and other anaerobic degradation reactions and the decrease in the rates of aerobic degradation in saturated soils. During the lowering of the water table, the average CH_4 and CO_2 fluxes increased up to 10 times in the ethanol/naphthalene spiked soils due to the release of the accumulated CH_4 and CO_2, and then CH_4 fluxes started decreasing because of aerobic CH_4 oxidation, while CO_2 fluxes continuously increased due to the aerobic degradation of DOC and CH_4. However, the average CH_4 and CO_2 fluxes dropped considerably due to limited upward diffusion during the imbibition periods.

The results of the soil water chemistry analysis showed that the average porewater DOC in the fluctuating and static ethanol/naphthalene-contaminated soil columns decreased by 95% and 75%, respectively, because of the combination of evaporation and aerobic degradation of ethanol and naphthalene, both of which were higher in the fluctuating columns, which increased the rate of DOC loss. The depth-averaged naphthalene concentrations dropped by 80% and 51% in the fluctuating and static soil columns, respectively, over eleven months, confirming the hypothesis that naphthalene is attenuated more efficiently in the fluctuating conditions. Also, the increase in naphthalene concentration below the water level in the fluctuating columns indicates drainage-imbibition cycles also cause downward transport of naphthalene in the column.

The model-predicted relative rates of HBM and ABM combined with the trends in the $\delta^{13}C$ isotope compositions of dissolved CO_2 and CH_4 indicate that HBM is the prevailing methanogenic pathway in the saturated ethanol/naphthalene spiked soil columns because H_2 and CO_2, produced by DOC fermentation, accumulate in the porewater. Then, the dominant methanogenic pathway shifted to ABM due to CO_2 consumption, H_2 depletion, and acetate production. After one drainage-imbibition cycle, $\delta^{13}C$-CH_4 became less negative, and CH_4 oxidation became the prevailing pathway controlling the $\delta^{13}C$-CH_4, and therefore the CH_4 efflux rates, in the fluctuating columns because of aerobic microbial CH_4 oxidation that can take place due to O_2 availability.

The model's ability to reproduce the experimental time series trends in porewater chemistry and surface gas effluxes indicates that the biogeochemical reaction network captures the most important reactions. Also, the model can successfully predict the impact of water table fluctuations

on gas effluxes and soil chemistry by defining chemical reaction rates and effective diffusion coefficients as a function of moisture content. The equations, which account for how moisture content modulates microbial reaction rates and effective gas diffusion coefficients, are some of the key functions in the modelling framework which enable the prediction of the impact of WTFs on reaction and transport rates. These functions can also be used to simulate the impact of any water table fluctuation regimes or moisture content variations on PHC NSZD at contaminated sites. Altogether, the reaction network and diffusion-reaction model framework that I have presented herein can be used as the basis for modeling methanogenic NSZD at any contaminated site.

The experiments and the numerical simulations presented in Chapters 2 and 3 are novel investigations into the impacts of FTCs and WTFs in contaminated soils. To the best of our knowledge, this is the first time the impact of FTCs and WTFs on methanogenic PHC biodegradation have been investigated. In the FTC experiment, we designed a batch experiment under anoxic, saturated condition to better understand methanogenic pathways in anoxic soils under FTCs, while previous studies have investigated FTCs under oxic conditions. The numerical simulation and the batch experiment showed that freezing-induced soil matrix disturbance is a potential mechanism for DOC increase during FTCs. As a result, this mechanism was considered in the model for the first time to accurately simulate DOC during FTCs. This mechanism was considered. While the effect of WTFs on soil surface gas effluxes and microbial communities has been studied extensively in the past, very few studies have investigated the impact of WTFs on methanogenic pathways in PHC-contaminated subsurface environments. In the WTFs experiment, $\delta^{13}C$-CO_2 and -CH_4 and dissolved CH_4 and CO_2 were measured to examine methanogenic biodegradation rates and pathways in anoxic, saturated soils and soils under WTFs. The WTFs experiment and model successfully showed how drained PHC contaminated sites can exacerbate global warming, whereas contaminated sites rewetting is effective for climate change mitigation.

4.2 Recommendations for future research

The FTCs batch experiment and model successfully simulated methanogenic PHC biodegradation in anoxic, saturated soils imposed to FTCs, although improvements to the methodology are needed for future works. The future research can focus on the impact of FTCs on microbial community composition and microbial activity in anoxic, saturated soils. In addition, column experiment could be conducted under FTCs to examine how variations in temperature and moisture profile affect methanogenic PHC biodegradation. $\delta^{13}C$-CO_2 and -CH_4, redox potential, DOC, and dissolved CH_4 and CO_2 at different depths could be measured to better understand how FTCs cause dynamic redox conditiosn and changes in methanogenic pathways and rates. In this thesis, I hypothesized that freezing-induced soil matrix disturbance is the main mechanism for DOC increase during FTCs. Future studies could find evidence for this hypothesis using microbial analysis on soil samples subjected to FTCs. Field observations and sampling for microbial and porewater analysis are another way to find evidence for DOC increases during freezing-induced soil matrix disturbances. In the FTCs modeling part of the project, I developed a 1D model representing the impact of FTCs on methanogenic degradation, but future studies can improve this model by developing a 3D model and upscale the model for field-scale simulation of FTCs processes.

The WTFs column experiment and model presented in Chapter 3 accurately simulated methanogenic PHC biodegradation in anoxic, saturated soils and soils imposed to WTFs, although future work could improve the methodology. By including the microbial community composition and microbial activity analyses, the impact of WTFs on microbial populations changes of PHC NSZD at contaminated sites can be the future studies. Field observations and sampling for microbial and porewater analysis, $\delta^{13}C$ compositions of dissolved CO_2 and CH_4, redox potential, DOC, and dissolved CH_4 and CO_2 at different depths could be conducted to better understand how WTFs modulate methanogenic PHC pathways and rates in contaminated sites under more environmentally-relevant conditions. In the WTFs model, I developed a 1D model representing the impact of WTFs on methanogenic degradation, but future studies can improve this model by developing a 3D model and upscale the model for field-scale simulation of WTFs.

References

Akbari, A., & Ghoshal, S. (2015). Effects of diurnal temperature variation on microbial community and petroleum hydrocarbon biodegradation in contaminated soils from a sub-A rctic site. *Environmental Microbiology*, *17*(12), 4916–4928.

Amos, R. T., & Mayer, K. U. (2006). Investigating the role of gas bubble formation and entrapment in contaminated aquifers: Reactive transport modelling. *Journal of Contaminant Hydrology*, *87*(1–2), 123–154.

Amos, R. T., Mayer, K. U., Bekins, B. A., Delin, G. N., & Williams, R. L. (2005). Use of dissolved and vapor-phase gases to investigate methanogenic degradation of petroleum hydrocarbon contamination in the subsurface. *Water Resources Research*, *41*(2).

Aurela, M., Riutta, T., Laurila, T., Tuovinen, J.-P., Vesala, T., Tuittila, E.-S., et al. (2007). CO2 exchange of a sedge fen in southern Finland-The impact of a drought period. *Tellus B: Chemical and Physical Meteorology*, *59*(5), 826–837.

Baehr, A. L., & Corapcioglu, M. Y. (1987). A compositional multiphase model for groundwater contamination by petroleum products: 2. Numerical solution. *Water Resources Research*, *23*(1), 201–213.

Basiliko, N., Khan, A., Prescott, C. E., Roy, R., & Grayston, S. J. (2009). Soil greenhouse gas and nutrient dynamics in fertilized western Canadian plantation forests. *Canadian Journal of Forest Research*, *39*(6), 1220–1235.

Bekins, B. A., Hostettler, F. D., Herkelrath, W. N., Delin, G. N., Warren, E., & Essaid, H. I. (2005). Progression of methanogenic degradation of crude oil in the subsurface. *Environmental Geosciences*, *12*(2), 139–152.

BenIsrael, M., Wanner, P., Aravena, R., Parker, B. L., Haack, E. A., Tsao, D. T., & Dunfield, K. E. (2019). Toluene biodegradation in the vadose zone of a poplar phytoremediation system identified using metagenomics and toluene-specific stable carbon isotope analysis. *International Journal of Phytoremediation*, *21*(1), 60–69.

Berglund, Ö., & Berglund, K. (2011). Influence of water table level and soil properties on emissions of greenhouse gases from cultivated peat soil. *Soil Biology and Biochemistry*, *43*(5), 923–931.

Blake, L. I., Tveit, A., Øvreås, L., Head, I. M., & Gray, N. D. (2015). Response of methanogens in Arctic sediments to temperature and methanogenic substrate availability. *PLoS One*, *10*(6), e0129733.

Brewer, P. E., Calderón, F., Vigil, M., & Von Fischer, J. C. (2018). Impacts of moisture, soil respiration, and agricultural practices on methanogenesis in upland soils as measured with stable isotope pool dilution. *Soil Biology and Biochemistry*, *127*, 239–251.

Brookfield, A. E., Blowes, D. W., & Mayer, K. U. (2006). Integration of field measurements and reactive transport modelling to evaluate contaminant transport at a sulfide mine tailings impoundment. *Journal of Contaminant Hydrology*, *88*(1–2), 1–22.

Byun, E., Rezanezhad, F., Fairbairn, L., Slowinski, S., Basiliko, N., Price, J. S., et al. (2021). Temperature, moisture and freeze–thaw controls on CO2 production in soil incubations from northern peatlands. *Scientific Reports*, *11*(1), 1–15.

Chan, O. C., Claus, P., Casper, P., Ulrich, A., Lueders, T., & Conrad, R. (2005). Vertical distribution of structure and function of the methanogenic archaeal community in Lake Dagow sediment. *Environmental Microbiology*, *7*(8), 1139–1149.

Chang, W., Klemm, S., Beaulieu, C., Hawari, J., Whyte, L., & Ghoshal, S. (2011). Petroleum hydrocarbon biodegradation under seasonal freeze− thaw soil temperature regimes in

contaminated soils from a Sub-Arctic Site. *Environmental Science & Technology*, *45*(3), 1061–1066.

Christiansen, J. R., Levy-Booth, D., Prescott, C. E., & Grayston, S. J. (2016). Microbial and environmental controls of methane fluxes along a soil moisture gradient in a Pacific coastal temperate rainforest. *Ecosystems*, *19*(7), 1255–1270.

Christiansen, J. R., Levy-Booth, D., Prescott, C. E., & Grayston, S. J. (2017). Different soil moisture control of net methane oxidation and production in organic upland and wet forest soils of the Pacific coastal rainforest in Canada. *Canadian Journal of Forest Research*, *47*(5), 628–635.

Conrad, R. (2020). Importance of hydrogenotrophic, aceticlastic and methylotrophic methanogenesis for methane production in terrestrial, aquatic and other anoxic environments: a mini review. *Pedosphere*, *30*(1), 25–39.

Conrad, R., & Klose, M. (1999). Anaerobic conversion of carbon dioxide to methane, acetate and propionate on washed rice roots. *FEMS Microbiology Ecology*, *30*(2), 147–155.

Costello, D. J., Greenfield, P. F., & Lee, P. L. (1991). Dynamic modelling of a single-stage high-rate anaerobic reactor—I. Model derivation. *Water Research*, *25*(7), 847–858.

Cruz-Martínez, K., Rosling, A., Zhang, Y., Song, M., Andersen, G. L., & Banfield, J. F. (2012). Effect of rainfall-induced soil geochemistry dynamics on grassland soil microbial communities. *Applied and Environmental Microbiology*, *78*(21), 7587–7595.

Davidson, E. A., Samanta, S., Caramori, S. S., & Savage, K. (2012). The D ual A rrhenius and M ichaelis–M enten kinetics model for decomposition of soil organic matter at hourly to seasonal time scales. *Global Change Biology*, *18*(1), 371–384.

Dean, J. F., Middelburg, J. J., Röckmann, T., Aerts, R., Blauw, L. G., Egger, M., et al. (2018). Methane feedbacks to the global climate system in a warmer world. *Reviews of Geophysics*, *56*(1), 207–250.

Ding, B., Rezanezhad, F., Gharedaghloo, B., Van Cappellen, P., & Passeport, E. (2019). Bioretention cells under cold climate conditions: Effects of freezing and thawing on water infiltration, soil structure, and nutrient removal. *Science of the Total Environment*, *649*, 749–759.

Dinsmore, K. J., Skiba, U. M., Billett, M. F., & Rees, R. M. (2009). Effect of water table on greenhouse gas emissions from peatland mesocosms. *Plant and Soil*, *318*(1), 229–242.

Dobson, R., Schroth, M. H., & Zeyer, J. (2007). Effect of water-table fluctuation on dissolution and biodegradation of a multi-component, light nonaqueous-phase liquid. *Journal of Contaminant Hydrology*, *94*(3–4), 235–248.

Easterling, D. R., Meehl, G. A., Parmesan, C., Changnon, S. A., Karl, T. R., & Mearns, L. O. (2000). Climate extremes: observations, modeling, and impacts. *Science*, *289*(5487), 2068–2074.

Ebrahimi, A., & Or, D. (2017). Mechanistic modeling of microbial interactions at pore to profile scale resolve methane emission dynamics from permafrost soil. *Journal of Geophysical Research: Biogeosciences*, *122*(5), 1216–1238.

Edwards, E. A., & Grbić-Galić, D. (1994). Anaerobic degradation of toluene and o-xylene by a methanogenic consortium. *Applied and Environmental Microbiology*, *60*(1), 313–322.

Elberling, B., Askaer, L., Jørgensen, C. J., Joensen, H. P., Kühl, M., Glud, R. N., & Lauritsen, F. R. (2011). Linking soil O2, CO2, and CH4 concentrations in a wetland soil: implications for CO2 and CH4 fluxes. *Environmental Science & Technology*, *45*(8), 3393–3399.

Ellis, D. E., & Hadley, P. W. (2009). Sustainable remediation white paper—Integrating

sustainable principles, practices, and metrics into remediation projects. *Remediation Journal*, *19*(3), 5–114.

Eriksson, M., Ka, J.-O., & Mohn, W. W. (2001). Effects of low temperature and freeze-thaw cycles on hydrocarbon biodegradation in Arctic tundra soil. *Applied and Environmental Microbiology*, *67*(11), 5107–5112.

Essaid, H. I., Cozzarelli, I. M., Eganhouse, R. P., Herkelrath, W. N., Bekins, B. A., & Delin, G. N. (2003). Inverse modeling of BTEX dissolution and biodegradation at the Bemidji, MN crude-oil spill site. *Journal of Contaminant Hydrology*, *67*(1–4), 269–299.

Essaid, H. I., Bekins, B. A., & Cozzarelli, I. M. (2015). Organic contaminant transport and fate in the subsurface: Evolution of knowledge and understanding. *Water Resources Research*, *51*(7), 4861–4902.

Estop-Aragonés, C., Knorr, K. H., & Blodau, C. (2013). Belowground in situ redox dynamics and methanogenesis recovery in a degraded fen during dry-wet cycles and flooding. *Biogeosciences*, *10*(1), 421–436.

Fairbairn, L. G. (2020). Linking soil moisture content and carbon dioxide fluxes: From batch experiments to process-based modelling. University of Waterloo.

Farnsworth, C. E., Voegelin, A., & Hering, J. G. (2012). Manganese oxidation induced by water table fluctuations in a sand column. *Environmental Science & Technology*, *46*(1), 277–284.

Fenchel, T., Blackburn, H., King, G. M., & Blackburn, T. H. (2012). *Bacterial biogeochemistry: the ecophysiology of mineral cycling*. Academic press.

Ferrick, M. G., & Gatto, L. W. (2005). Quantifying the effect of a freeze–thaw cycle on soil erosion: laboratory experiments. *Earth Surface Processes and Landforms: The Journal of the British Geomorphological Research Group*, *30*(10), 1305–1326.

Fierer, N., & Schimel, J. P. (2002). Effects of drying–rewetting frequency on soil carbon and nitrogen transformations. *Soil Biology and Biochemistry*, *34*(6), 777–787.

Von Fischer, J. C., & Hedin, L. O. (2007). Controls on soil methane fluxes: Tests of biophysical mechanisms using stable isotope tracers. *Global Biogeochemical Cycles*, *21*(2).

Franz, D., Koebsch, F., Larmanou, E., Augustin, J., & Sachs, T. (2016). High net CO 2 and CH 4 release at a eutrophic shallow lake on a formerly drained fen. *Biogeosciences*, *13*(10), 3051–3070.

Fu, B., Jin, X., Conrad, R., Liu, H., & Liu, H. (2019). Competition between chemolithotrophic acetogenesis and hydrogenotrophic methanogenesis for exogenous H2/CO2 in anaerobically digested sludge: impact of temperature. *Frontiers in Microbiology*, 2418.

Fuss, C. B., Driscoll, C. T., Groffman, P. M., Campbell, J. L., Christenson, L. M., Fahey, T. J., et al. (2016). Nitrate and dissolved organic carbon mobilization in response to soil freezing variability. *Biogeochemistry*, *131*(1), 35–47.

Garg, S., Newell, C. J., Kulkarni, P. R., King, D. C., Adamson, D. T., Renno, M. I., & Sale, T. (2017). Overview of natural source zone depletion: processes, controlling factors, and composition change. *Groundwater Monitoring & Remediation*, *37*(3), 62–81.

Van Genuchten, M. T. (1980). A closed-form equation for predicting the hydraulic conductivity of unsaturated soils. *Soil Science Society of America Journal*, *44*(5), 892–898.

Ghezzehei, T.A., Sulman, B., Arnold, C. L., Bogie, N. A., & Berhe, A. A. (2019). On the role of soil water retention characteristic on aerobic microbial respiration. *Biogeosciences*, *16*, 1187–1209. https://doi.org/10.5194/bg-2018-265

Ghezzehei, T. A., Sulman, B., Arnold, C. L., Bogie, N. A., & Berhe, A. A. (2019). On the role of soil water retention characteristic on aerobic microbial respiration. *Biogeosciences*, *16*(6),

1187–1209.
Gieg, L. M., Fowler, S. J., & Berdugo-Clavijo, C. (2014). Syntrophic biodegradation of hydrocarbon contaminants. *Current Opinion in Biotechnology*, *27*, 21–29.
Giesler, R., Högberg, M. N., Strobel, B. W., Richter, A., Nordgren, A., & Högberg, P. (2007). Production of dissolved organic carbon and low-molecular weight organic acids in soil solution driven by recent tree photosynthate. *Biogeochemistry*, *84*(1), 1–12.
Gray, N. D., Sherry, A., Hubert, C., Dolfing, J., & Head, I. M. (2010). Methanogenic degradation of petroleum hydrocarbons in subsurface environments: remediation, heavy oil formation, and energy recovery. *Advances in Applied Microbiology*, *72*, 137–161.
Green, D., Rezanezhad, F., Wagner-Riddle, C., Jordan, S., Henry, H., & Van Cappellen, P. (2022). Effects of Winter Pulsed Warming and Snowmelt on Soil Nitrogen Cycling in an Agroecosystem: A Lysimeter Study. In *2022 Goldschmidt Conference*. GOLDSCHMIDT.
Günther, A., Barthelmes, A., Huth, V., Joosten, H., Jurasinski, G., Koebsch, F., & Couwenberg, J. (2020). Prompt rewetting of drained peatlands reduces climate warming despite methane emissions. *Nature Communications*, *11*(1), 1–5.
Gupta, P. K., Gharedaghloo, B., Lynch, M., Cheng, J., Strack, M., Charles, T. C., & Price, J. S. (2020). Dynamics of microbial populations and diversity in NAPL contaminated peat soil under varying water table conditions. *Environmental Research*, *191*, 110167.
Haberer, C. M., Rolle, M., Cirpka, O. A., & Grathwohl, P. (2012). Oxygen transfer in a fluctuating capillary fringe. *Vadose Zone Journal*, *11*(3).
Hack, N., Reinwand, C., Abbt-Braun, G., Horn, H., & Frimmel, F. H. (2015). Biodegradation of phenol, salicylic acid, benzenesulfonic acid, and iomeprol by Pseudomonas fluorescens in the capillary fringe. *Journal of Contaminant Hydrology*, *183*, 40–54.
Hahn, J., Köhler, S., Glatzel, S., & Jurasinski, G. (2015). Methane exchange in a coastal fen in the first year after flooding-a systems shift. *PloS One*, *10*(10), e0140657.
Henneberg, A., Brix, H., & Sorrell, B. K. (2016). The interactive effect of Juncus effusus and water table position on mesocosm methanogenesis and methane emissions. *Plant and Soil*, *400*(1), 45–54.
Henry, H. A. L. (2007). Soil freeze–thaw cycle experiments: trends, methodological weaknesses and suggested improvements. *Soil Biology and Biochemistry*, *39*(5), 977–986.
Hodgkins, S. B., Tfaily, M. M., McCalley, C. K., Logan, T. A., Crill, P. M., Saleska, S. R., et al. (2014). Changes in peat chemistry associated with permafrost thaw increase greenhouse gas production. *Proceedings of the National Academy of Sciences*, *111*(16), 5819–5824.
Hoehler, T. M., Albert, D. B., Alperin, M. J., & Martens, C. S. (1999). Acetogenesis from CO2 in an anoxic marine sediment. *Limnology and Oceanography*, *44*(3), 662–667.
Hofmann, A. F., Meysman, F. J. R., Soetaert, K., & Middelburg, J. J. (2008). A step-by-step procedure for pH model construction in aquatic systems. *Biogeosciences*, *5*(1), 227–251.
Hogg, E. H., Lieffers, V. J., & Wein, R. W. (1992). Potential carbon losses from peat profiles: effects of temperature, drought cycles, and fire. *Ecological Applications*, *2*(3), 298–306.
Holden, P. A., & Fierer, N. (2005). Microbial processes in the vadose zone. *Vadose Zone Journal*, *4*(1), 1–21.
Huang, X., & Rudolph, D. L. (2021). Coupled model for water, vapour, heat, stress and strain fields in variably saturated freezing soils. *Advances in Water Resources*, *154*, 103945.
Irianni-Renno, M., Akhbari, D., Olson, M. R., Byrne, A. P., Lefèvre, E., Zimbron, J., et al. (2016). Comparison of bacterial and archaeal communities in depth-resolved zones in an LNAPL body. *Applied Microbiology and Biotechnology*, *100*(7), 3347–3360.

Jin, Q., & Kirk, M. F. (2018). pH as a primary control in environmental microbiology: 2. Kinetic perspective. *Frontiers in Environmental Science*, 101.

Jones, D. M., Head, I. M., Gray, N. D., Adams, J. J., Rowan, A. K., Aitken, C. M., et al. (2008). Crude-oil biodegradation via methanogenesis in subsurface petroleum reservoirs. *Nature*, *451*(7175), 176–180.

Jourabchi, P., Van Cappellen, P., & Regnier, P. (2005). Quantitative interpretation of pH distributions in aquatic sediments: A reaction-transport modeling approach. *American Journal of Science*, *305*(9), 919–956.

Karimi Askarani, K., Stockwell, E. B., Piontek, K. R., & Sale, T. C. (2018). Thermal monitoring of natural source zone depletion. *Groundwater Monitoring & Remediation*, *38*(3), 43–52.

Keiluweit, M., Nico, P. S., Kleber, M., & Fendorf, S. (2016). Are oxygen limitations under recognized regulators of organic carbon turnover in upland soils? *Biogeochemistry*, *127*(2), 157–171.

Keiluweit, M., Wanzek, T., Kleber, M., Nico, P., & Fendorf, S. (2017). Anaerobic microsites have an unaccounted role in soil carbon stabilization. *Nature Communications*, *8*(1), 1–10.

Kettunen, A. (2003). Connecting methane fluxes to vegetation cover and water table fluctuations at microsite level: a modeling study. *Global Biogeochemical Cycles*, *17*(2).

Kettunen, A., Kaitala, V., Lehtinen, A., Lohila, A., Alm, J., Silvola, J., & Martikainen, P. J. (1999). Methane production and oxidation potentials in relation to water table fluctuations in two boreal mires. *Soil Biology and Biochemistry*, *31*(12), 1741–1749.

Khasi, S., Ramezanzadeh, M., & Ghazanfari, M. H. (2019). Experimentally based pore network modeling of NAPL dissolution process in heterogeneous porous media. *Journal of Contaminant Hydrology*, 103565. https://doi.org/10.1016/J.JCONHYD.2019.103565

Khasi, S., Fayazi, A., & Kantzas, A. (2021). A Pore-Scale Model for Dispersion and Mass Transfer during Acoustically Assisted Miscible Displacements in Porous Media. *Industrial & Engineering Chemistry Research*, *60*(4), 1884–1900.

Klüpfel, L., Piepenbrock, A., Kappler, A., & Sander, M. (2014). Humic substances as fully regenerable electron acceptors in recurrently anoxic environments. *Nature Geoscience*, *7*(3), 195–200.

Knorr, K. H., Glaser, B., & Blodau, C. (2008). Fluxes and 13 C isotopic composition of dissolved carbon and pathways of methanogenesis in a fen soil exposed to experimental drought. *Biogeosciences*, *5*(5), 1457–1473.

Knorr, K. H., Lischeid, G., & Blodau, C. (2009). Dynamics of redox processes in a minerotrophic fen exposed to a water table manipulation. *Geoderma*, *153*(3), 379–392. https://doi.org/https://doi.org/10.1016/j.geoderma.2009.08.023

Koenigk, T., Brodeau, L., Graversen, R. G., Karlsson, J., Svensson, G., Tjernström, M., et al. (2013). Arctic climate change in 21st century CMIP5 simulations with EC-Earth. *Climate Dynamics*, *40*(11), 2719–2743.

Koponen, H. T., & Bååth, E. (2016). Soil bacterial growth after a freezing/thawing event. *Soil Biology and Biochemistry*, *100*, 229–232.

Kotsyurbenko, O. R. (2005). Trophic interactions in the methanogenic microbial community of low-temperature terrestrial ecosystems. *FEMS Microbiology Ecology*, *53*(1), 3–13.

Kraev, G., Schulze, E.-D., Yurova, A., Kholodov, A., Chuvilin, E., & Rivkina, E. (2017). Cryogenic displacement and accumulation of biogenic methane in frozen soils. *Atmosphere*, *8*(6), 105.

Krogstad, K. (2021). Impact of Winter Soil Processes on Nutrient Leaching in Cold Region

Agroecosystems. University of Waterloo.
Kulkarni, P. R., Newell, C. J., King, D. C., Molofsky, L. J., & Garg, S. (2020). Application of four measurement techniques to understand natural source zone depletion processes at an LNAPL site. *Groundwater Monitoring & Remediation*, *40*(3), 75–88.
Kværnø, S. H., & Øygarden, L. (2006). The influence of freeze–thaw cycles and soil moisture on aggregate stability of three soils in Norway. *Catena*, *67*(3), 175–182.
Legout, C., Molenat, J., & Hamon, Y. (2009). Experimental and modeling investigation of unsaturated solute transport with water-table fluctuation. *Vadose Zone Journal*, *8*(1), 21–31.
Leifeld, J., Wüst-Galley, C., & Page, S. (2019). Intact and managed peatland soils as a source and sink of GHGs from 1850 to 2100. *Nature Climate Change*, *9*(12), 945–947. https://doi.org/10.1038/s41558-019-0615-5
Lemming, G., Chambon, J. C., Binning, P. J., & Bjerg, P. L. (2012). Is there an environmental benefit from remediation of a contaminated site? Combined assessments of the risk reduction and life cycle impact of remediation. *Journal of Environmental Management*, *112*, 392–403.
Lin, X., McKinley, J., Resch, C. T., Kaluzny, R., Lauber, C. L., Fredrickson, J., et al. (2012). Spatial and temporal dynamics of the microbial community in the Hanford unconfined aquifer. *The ISME Journal*, *6*(9), 1665–1676.
Magen, C., Lapham, L. L., Pohlman, J. W., Marshall, K., Bosman, S., Casso, M., & Chanton, J. P. (2014). A simple headspace equilibration method for measuring dissolved methane. *Limnology and Oceanography: Methods*, *12*(9), 637–650.
Mäkiranta, P., Laiho, R., Fritze, H., Hytönen, J., Laine, J., & Minkkinen, K. (2009). Indirect regulation of heterotrophic peat soil respiration by water level via microbial community structure and temperature sensitivity. *Soil Biology and Biochemistry*, *41*(4), 695–703.
Mander, Ü., Maddison, M., Soosaar, K., & Karabelnik, K. (2011). The impact of pulsing hydrology and fluctuating water table on greenhouse gas emissions from constructed wetlands. *Wetlands*, *31*(6), 1023–1032.
Martikainen, P. J., Nykänen, H., Crill, P., & Silvola, J. (1993). Effect of a lowered water table on nitrous oxide fluxes from northern peatlands. *Nature*, *366*(6450), 51–53.
Matzner, E., & Borken, W. (2008). Do freeze-thaw events enhance C and N losses from soils of different ecosystems? A review. *European Journal of Soil Science*, *59*(2), 274–284.
Mayer, A. S., & Hassanizadeh, S. M. (2005). *Soil and Groundwater Contamination: Nonaqueous Phase Liquids–Principles and Observations*. American Geophysical Union. https://doi.org/10.1029/WM017
Mayer, K. U., Frind, E. O., & Blowes, D. W. (2002). Multicomponent reactive transport modeling in variably saturated porous media using a generalized formulation for kinetically controlled reactions. *Water Resources Research*, *38*(9), 11–13.
McCarter, C. P. R., Rezanezhad, F., Quinton, W. L., Gharedaghloo, B., Lennartz, B., Price, J., et al. (2020). Pore-scale controls on hydrological and geochemical processes in peat: Implications on interacting processes. *Earth-Science Reviews*, *207*, 103227.
McKnight, D. M., Andrews, E. D., Spaulding, S. A., & Aiken, G. R. (1994). Aquatic fulvic acids in algal-rich Antarctic ponds. *Limnology and Oceanography*, *39*(8), 1972–1979.
McNicol, G., & Silver, W. L. (2014). Separate effects of flooding and anaerobiosis on soil greenhouse gas emissions and redox sensitive biogeochemistry. *Journal of Geophysical Research: Biogeosciences*, *119*(4), 557–566.
Millington, R. J., & Quirk, J. P. (1961). Permeability of porous solids. *Transactions of the*

Faraday Society, *57*, 1200–1207.
Minick, K. J., Mitra, B., Li, X., Noormets, A., & King, J. S. (2019). Water table drawdown alters soil and microbial carbon pool size and isotope composition in coastal freshwater forested wetlands. *Frontiers in Forests and Global Change*, *2*, 7.
Molins, S., & Mayer, K. U. (2007). Coupling between geochemical reactions and multicomponent gas and solute transport in unsaturated media: A reactive transport modeling study. *Water Resources Research*, *43*(5).
Molins, S., Mayer, K. U., Amos, R. T., & Bekins, B. A. (2010). Vadose zone attenuation of organic compounds at a crude oil spill site—Interactions between biogeochemical reactions and multicomponent gas transport. *Journal of Contaminant Hydrology*, *112*(1–4), 15–29.
Moore, T. R., & Knowles, R. (1989). The influence of water table levels on methane and carbon dioxide emissions from peatland soils. *Canadian Journal of Soil Science*, *69*(1), 33–38.
Mosey, F. E. (1983). Mathematical modelling of the anaerobic digestion process: regulatory mechanisms for the formation of short-chain volatile acids from glucose. *Water Science and Technology*, *15*(8–9), 209–232.
Moyano, F. E., Manzoni, S., & Chenu, C. (2013). Responses of soil heterotrophic respiration to moisture availability: An exploration of processes and models. *Soil Biology and Biochemistry*, *59*, 72–85.
Natali, S. M., Watts, J. D., Rogers, B. M., Potter, S., Ludwig, S. M., Selbmann, A.-K., et al. (2019). Large loss of CO2 in winter observed across the northern permafrost region. *Nature Climate Change*, *9*(11), 852–857.
Ng, G. C., Bekins, B. A., Cozzarelli, I. M., Baedecker, M. J., Bennett, P. C., Amos, R. T., & Herkelrath, W. N. (2015). Reactive transport modeling of geochemical controls on secondary water quality impacts at a crude oil spill site near Bemidji, MN. *Water Resources Research*, *51*(6), 4156–4183.
Nozhevnikova, A. N., Nekrasova, V., Ammann, A., Zehnder, A. J. B., Wehrli, B., & Holliger, C. (2007). Influence of temperature and high acetate concentrations on methanogenensis in lake sediment slurries. *FEMS Microbiology Ecology*, *62*(3), 336–344.
Oertel, C., Matschullat, J., Zurba, K., Zimmermann, F., & Erasmi, S. (2016). Greenhouse gas emissions from soils—A review. *Geochemistry*, *76*(3), 327–352.
Okumura, T., Kawagucci, S., Saito, Y., Matsui, Y., Takai, K., & Imachi, H. (2016). Hydrogen and carbon isotope systematics in hydrogenotrophic methanogenesis under H 2-limited and H 2-enriched conditions: implications for the origin of methane and its isotopic diagnosis. *Progress in Earth and Planetary Science*, *3*(1), 1–19.
Öquist, M. G., Nilsson, M., Sörensson, F., Kasimir-Klemedtsson, Å., Persson, T., Weslien, P., & Klemedtsson, L. (2004). Nitrous oxide production in a forest soil at low temperatures–processes and environmental controls. *FEMS Microbiology Ecology*, *49*(3), 371–378.
Ossai, I. C., Ahmed, A., Hassan, A., & Hamid, F. S. (2020). Remediation of soil and water contaminated with petroleum hydrocarbon: A review. *Environmental Technology & Innovation*, *17*, 100526.
Penning, H., Claus, P., Casper, P., & Conrad, R. (2006). Carbon isotope fractionation during acetoclastic methanogenesis by Methanosaeta concilii in culture and a lake sediment. *Applied and Environmental Microbiology*, *72*(8), 5648–5652.
Peralta, A. L., Ludmer, S., Matthews, J. W., & Kent, A. D. (2014). Bacterial community response to changes in soil redox potential along a moisture gradient in restored wetlands. *Ecological Engineering*, *73*, 246–253.

Prieto-Espinoza, M., Weill, S., Belfort, B., Muller, E. E. L., Masbou, J., Lehmann, F., et al. (2021). Water table fluctuations affect dichloromethane biodegradation in lab-scale aquifers contaminated with organohalides. *Water Research*, *203*, 117530.

Pronk, G. J., Mellage, A., Milojevic, T., Smeaton, C. M., Engel, K., Neufeld, J. D., et al. (2020). Carbon turnover and microbial activity in an artificial soil under imposed cyclic drainage and imbibition. *Vadose Zone Journal*, *19*(1), e20021.

Prowse, T. D., Furgal, C., Wrona, F. J., & Reist, J. D. (2009). Implications of climate change for northern Canada: freshwater, marine, and terrestrial ecosystems. *Ambio*, 282–289.

Rafat, A., Rezanezhad, F., Quinton, W. L., Humphreys, E. R., Webster, K., & Van Cappellen, P. (2021). Non-growing season carbon emissions in a northern peatland are projected to increase under global warming. *Communications Earth & Environment*, *2*(1), 1–12.

Ramezanzadeh, M., Aminnaji, M., Rezanezhad, F., Ghazanfari, M. H., & Babaei, M. (2022). Dissolution and remobilization of NAPL in surfactant-enhanced aquifer remediation from microscopic scale simulations. *Chemosphere*, *289*, 133177.

Regina, K., Syväsalo, E., Hannukkala, A., & Esala, M. (2004). Fluxes of N2O from farmed peat soils in Finland. *European Journal of Soil Science*, *55*(3), 591–599.

Rezanezhad, F., Couture, R.-M., Kovac, R., O'Connell, D., & Van Cappellen, P. (2014). Water table fluctuations and soil biogeochemistry: An experimental approach using an automated soil column system. *Journal of Hydrology*, *509*, 245–256.

Rosso, L., Lobry, J. R., & Flandrois, J.-P. (1993). An unexpected correlation between cardinal temperatures of microbial growth highlighted by a new model. *Journal of Theoretical Biology*, *162*(4), 447–463.

Rubol, S., Manzoni, S., Bellin, A., & Porporato, A. (2013). Modeling soil moisture and oxygen effects on soil biogeochemical cycles including dissimilatory nitrate reduction to ammonium (DNRA). *Advances in Water Resources*, *62*, 106–124.

Rühle, F. A., von Netzer, F., Lueders, T., & Stumpp, C. (2015). Response of transport parameters and sediment microbiota to water table fluctuations in laboratory columns. *Vadose Zone Journal*, *14*(5), 1–12.

Säurich, A., Tiemeyer, B., Dettmann, U., & Don, A. (2019). How do sand addition, soil moisture and nutrient status influence greenhouse gas fluxes from drained organic soils? *Soil Biology and Biochemistry*, *135*, 71–84.

Sawicka, J. E., Robador, A., Hubert, C., Jørgensen, B. B., & Brüchert, V. (2010). Effects of freeze–thaw cycles on anaerobic microbial processes in an Arctic intertidal mud flat. *The ISME Journal*, *4*(4), 585–594.

Schimel, J. P., & Clein, J. S. (1996). Microbial response to freeze-thaw cycles in tundra and taiga soils. *Soil Biology and Biochemistry*, *28*(8), 1061–1066.

Scholten, J. C. M., Conrad, R., & Stams, A. J. M. (2000). Effect of 2-bromo-ethane sulfonate, molybdate and chloroform on acetate consumption by methanogenic and sulfate-reducing populations in freshwater sediment. *FEMS Microbiology Ecology*, *32*(1), 35–42.

Sexstone, A. J., Revsbech, N. P., Parkin, T. B., & Tiedje, J. M. (1985). Direct measurement of oxygen profiles and denitrification rates in soil aggregates. *Soil Science Society of America Journal*, *49*(3), 645–651.

Sharma, S., Szele, Z., Schilling, R., Munch, J. C., & Schloter, M. (2006). Influence of freeze-thaw stress on the structure and function of microbial communities and denitrifying populations in soil. *Applied and Environmental Microbiology*, *72*(3), 2148–2154.

Sheng, Y., Li, G., Dong, H., Liu, Y., Ma, L., Yang, M., et al. (2021). Distinct assembly processes

shape bacterial communities along unsaturated, groundwater fluctuated, and saturated zones. *Science of the Total Environment*, *761*, 143303.

Shi, B., Ngueleu, S. K., Rezanezhad, F., Slowinski, S., Pronk, G. J., Smeaton, C. M., et al. (2020). Sorption and Desorption of the Model Aromatic Hydrocarbons Naphthalene and Benzene: Effects of Temperature and Soil Composition. *Frontiers in Environmental Chemistry*, 13.

Siegrist, H., Renggli, D., & Gujer, W. (1993). Mathematical modelling of anaerobic mesophilic sewage sludge treatment. *Water Science and Technology*, *27*(2), 25–36.

Sierra, C. A., Malghani, S., & Loescher, H. W. (2017). Interactions among temperature, moisture, and oxygen concentrations in controlling decomposition rates in a boreal forest soil. *Biogeosciences*, *14*(3), 703–710.

Sihota, N. J., & Mayer, K. U. (2012). Characterizing vadose zone hydrocarbon biodegradation using carbon dioxide effluxes, isotopes, and reactive transport modeling. *Vadose Zone Journal*, *11*(4), vzj2011-0204.

Sihota, N. J., Singurindy, O., & Mayer, K. U. (2011). CO2-efflux measurements for evaluating source zone natural attenuation rates in a petroleum hydrocarbon contaminated aquifer. *Environmental Science & Technology*, *45*(2), 482–488.

Sihota, N. J., Mayer, K. U., Toso, M. A., & Atwater, J. F. (2013). Methane emissions and contaminant degradation rates at sites affected by accidental releases of denatured fuel-grade ethanol. *Journal of Contaminant Hydrology*, *151*, 1–15.

Sihota, N. J., Trost, J. J., Bekins, B. A., Berg, A., Delin, G. N., Mason, B., et al. (2016). Seasonal variability in vadose zone biodegradation at a crude oil pipeline rupture site. *Vadose Zone Journal*, *15*(5).

Silvola, J., Alm, J., Ahlholm, U., Nykanen, H., & Martikainen, P. J. (1996). CO_2 fluxes from peat in boreal mires under varying temperature and moisture conditions. *Journal of Ecology*, 219–228.

Šimůnek, J., & Suarez, D. L. (1993). Modeling of carbon dioxide transport and production in soil: 1. Model development. *Water Resources Research*, *29*(2), 487–497.

Smeaton, C. M., & Van Cappellen, P. (2018). Gibbs Energy Dynamic Yield Method (GEDYM): Predicting microbial growth yields under energy-limiting conditions. *Geochimica et Cosmochimica Acta*, *241*, 1–16.

Song, Y., Zou, Y., Wang, G., & Yu, X. (2017). Altered soil carbon and nitrogen cycles due to the freeze-thaw effect: A meta-analysis. *Soil Biology and Biochemistry*, *109*, 35–49.

Su, D., Mayer, K. U., & MacQuarrie, K. T. B. (2021). MIN3P-HPC: a high-performance unstructured grid code for subsurface flow and reactive transport simulation. *Mathematical Geosciences*, *53*(4), 517–550.

Sun, C. L., Brauer, S. L., Cadillo-Quiroz, H., Zinder, S. H., & Yavitt, J. B. (2012). Seasonal changes in methanogenesis and methanogenic community in three peatlands, New York State. *Frontiers in Microbiology*, *3*, 81.

Tang, J., & Riley, W. J. (2019). A theory of effective microbial substrate affinity parameters in variably saturated soils and an example application to aerobic soil heterotrophic respiration. *Journal of Geophysical Research: Biogeosciences*, *124*(4), 918–940.

Teepe, R., Brumme, R., & Beese, F. (2001). Nitrous oxide emissions from soil during freezing and thawing periods. *Soil Biology and Biochemistry*, *33*(9), 1269–1275.

Tice, A. R., Anderson, D. M., & Banin, A. (1976). The prediction of unfrozen water contents in frozen soils from liquid limit determinations. Cold Regions Research & Engineering

Laboratory. *US Army Corps of Engineers*.
Tiemeyer, B., Albiac Borraz, E., Augustin, J., Bechtold, M., Beetz, S., Beyer, C., et al. (2016). High emissions of greenhouse gases from grasslands on peat and other organic soils. *Global Change Biology*, *22*(12), 4134–4149.
Vavilin, V. A., Rytov, S. V, & Lokshina, L. Y. (2018). Modelling the specific pathway of CH4 and CO2 formation using carbon isotope fractionation: an example for a boreal mesotrophic fen. *Isotopes in Environmental and Health Studies*, *54*(5), 475–493.
Van De Ven, C. J. C., Scully, K. H., Frame, M. A., Sihota, N. J., & Mayer, K. U. (2021). Impacts of water table fluctuations on actual and perceived natural source zone depletion rates. *Journal of Contaminant Hydrology*, *238*, 103771.
Vencelides, Z., Sracek, O., & Prommer, H. (2007). Modelling of iron cycling and its impact on the electron balance at a petroleum hydrocarbon contaminated site in Hnevice, Czech Republic. *Journal of Contaminant Hydrology*, *89*(3–4), 270–294.
Verginelli, I., Pecoraro, R., & Baciocchi, R. (2018). Using dynamic flux chambers to estimate the natural attenuation rates in the subsurface at petroleum contaminated sites. *Science of the Total Environment*, *619*, 470–479.
Vestgarden, L. S., & Austnes, K. (2009). Effects of freeze–thaw on C and N release from soils below different vegetation in a montane system: a laboratory experiment. *Global Change Biology*, *15*(4), 876–887.
Voigt, C., Lamprecht, R. E., Marushchak, M. E., Lind, S. E., Novakovskiy, A., Aurela, M., et al. (2017). Warming of subarctic tundra increases emissions of all three important greenhouse gases–carbon dioxide, methane, and nitrous oxide. *Global Change Biology*, *23*(8), 3121–3138.
Voigt, C., Marushchak, M. E., Mastepanov, M., Lamprecht, R. E., Christensen, T. R., Dorodnikov, M., et al. (2019). Ecosystem carbon response of an Arctic peatland to simulated permafrost thaw. *Global Change Biology*, *25*(5), 1746–1764.
Wagner-Riddle, C., Congreves, K. A., Abalos, D., Berg, A. A., Brown, S. E., Ambadan, J. T., et al. (2017). Globally important nitrous oxide emissions from croplands induced by freeze–thaw cycles. *Nature Geoscience*, *10*(4), 279–283.
Wang, Y., Yuan, F., Yuan, F., Gu, B., Hahn, M. S., Torn, M. S., et al. (2019). Mechanistic modeling of microtopographic impacts on CO2 and CH4 fluxes in an alaskan tundra ecosystem using the CLM-microbe model. *Journal of Advances in Modeling Earth Systems*, *11*(12), 4288–4304.
Wessolek, G., Schwärzel, K., Renger, M., Sauerbrey, R., & Siewert, C. (2002). Soil hydrology and CO2 release of peat soils. *Journal of Plant Nutrition and Soil Science*, *165*(4), 494–500.
Whiticar, M. J. (2020). The biogeochemical methane cycle. *Hydrocarbons, Oils and Lipids: Diversity, Origin, Chemistry and Fate*, 669–746.
Whittington, P. N., & Price, J. S. (2006). The effects of water table draw-down (as a surrogate for climate change) on the hydrology of a fen peatland, Canada. *Hydrological Processes*, *20*(17), 3589–3600.
Wiedermann, M. M., Kane, E. S., Potvin, L. R., & Lilleskov, E. A. (2017). Interactive plant functional group and water table effects on decomposition and extracellular enzyme activity in Sphagnum peatlands. *Soil Biology and Biochemistry*, *108*, 1–8.
Williams, M. D., & Oostrom, M. (2000). Oxygenation of anoxic water in a fluctuating water table system: an experimental and numerical study. *Journal of Hydrology*, *230*(1–2), 70–85.
Wu, H., Xingkai, X., Cheng, W., & Lin, H. (2020). Dissolved organic matter and inorganic N

jointly regulate greenhouse gases fluxes from forest soils with different moistures during a freeze-thaw period. *Soil Science and Plant Nutrition*, *66*(1), 163–176.

Xia, X., Stewart, D. I., Cheng, L., Liu, Y., Wang, Y., & Ding, A. (2022). Variation of bacterial community and alkane monooxygenase gene abundance in diesel n-alkane contaminated subsurface environment under seasonal water table fluctuation. *Journal of Contaminant Hydrology*, *248*, 104017.

Xue, D., Chen, H., Zhan, W., Huang, X., He, Y., zhao, chuan, et al. (2020). *How do water table drawdown, duration of drainage and warming influence greenhouse gas emissions from drained peatlands of the Zoige Plateau?* https://doi.org/10.22541/au.159741423.36340514

Zhang, Y., Chen, W., Smith, S. L., Riseborough, D. W., & Cihlar, J. (2005). Soil temperature in Canada during the twentieth century: Complex responses to atmospheric climate change. *Journal of Geophysical Research: Atmospheres*, *110*(D3).

Zhong, Q., Chen, H., Liu, L., He, Y., Zhu, D., Jiang, L., et al. (2017). Water table drawdown shapes the depth-dependent variations in prokaryotic diversity and structure in Zoige peatlands. *FEMS Microbiology Ecology*, *93*(6).

Zhou, Z., Liu, X., Sun, K., Lin, C., Ma, J., He, M., & Ouyang, W. (2019). Persulfate-based advanced oxidation processes (AOPs) for organic-contaminated soil remediation: A review. *Chemical Engineering Journal*, *372*, 836–851.

Zinder, S. H., Anguish, T., & Cardwell, S. C. (1984). Selective inhibition by 2-bromoethanesulfonate of methanogenesis from acetate in a thermophilic anaerobic digestor. *Applied and Environmental Microbiology*, *47*(6), 1343–1345.

Appendix

*Appendix **I** – Additional experimental results from Chapter 2*

Porewater sulfate and DIC experimental data and model simulations:

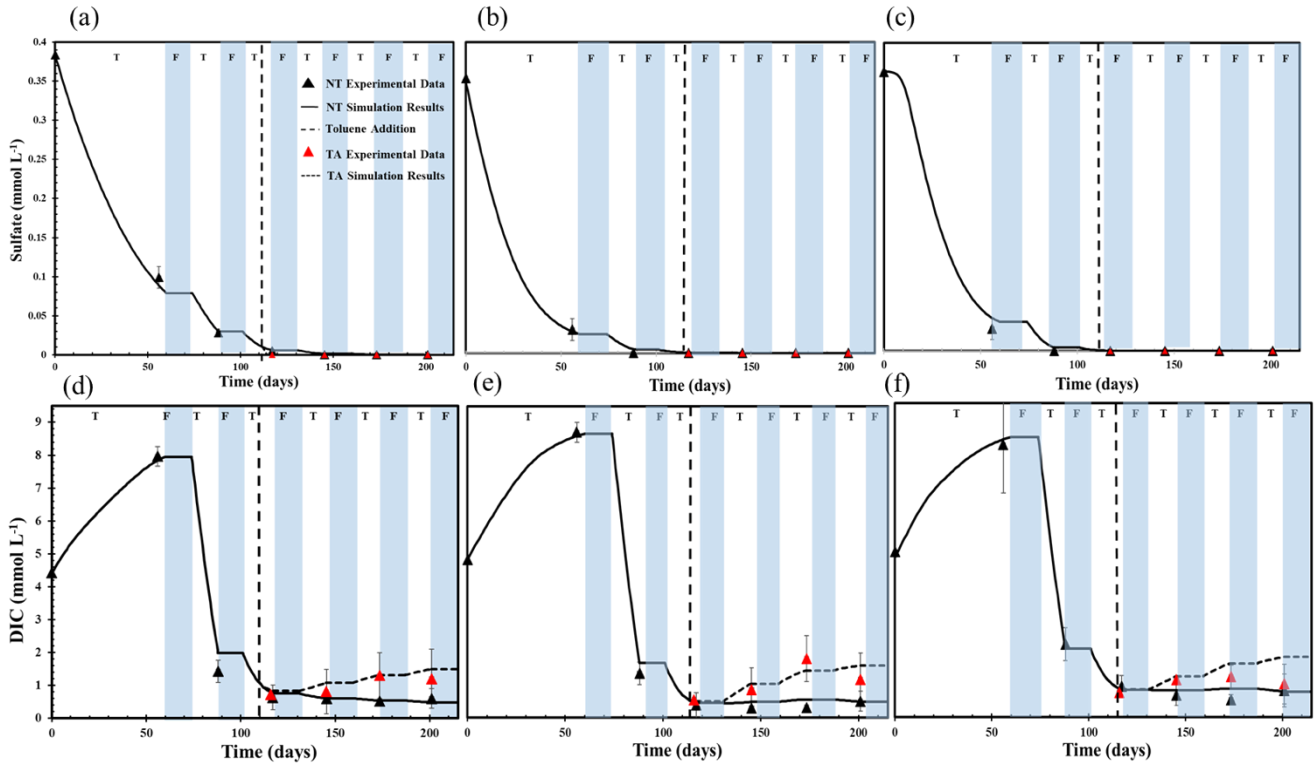

Figure A1-1: SO_4^{2-} concentrations in (a) NL, (b) LA, and (c) BES treatments (-NT and -TA), and DIC concentrations in (d) NL, (e) LA, and (f) BES treatment batch incubations during 215 days of experiment with freeze (F, at -10°C) and thaw (T, at 15°C) cycles.

Reaction rates:

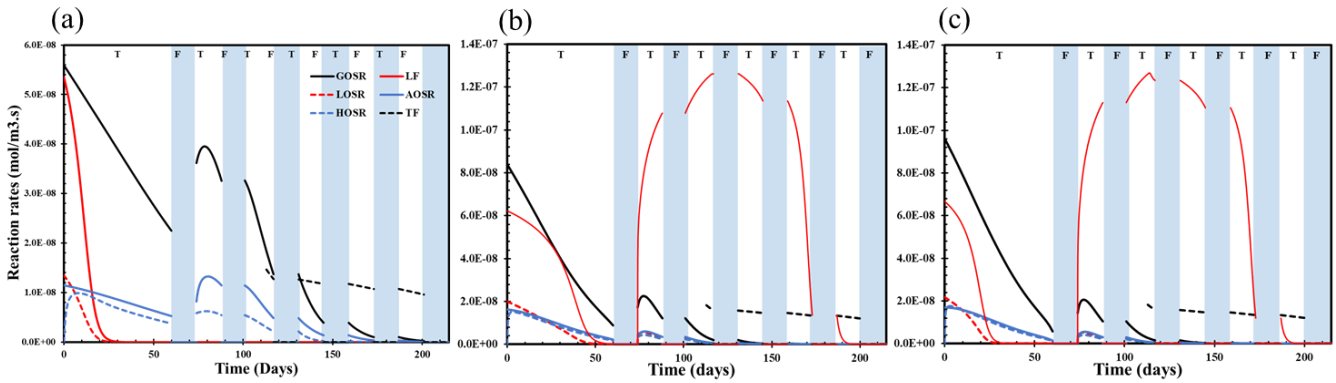

Figure A1-2: Simulation results of the rates of GOSR, LOSR, HOSR, LF, AOSR, and TF in the (a) NL, (b) LA, and (c) BES treatments during 215 days of experiment with freeze (F, at -10°C) and thaw (T, at 15°C) cycles.

*Appendix **II** – Additional experimental results from Chapter 3*

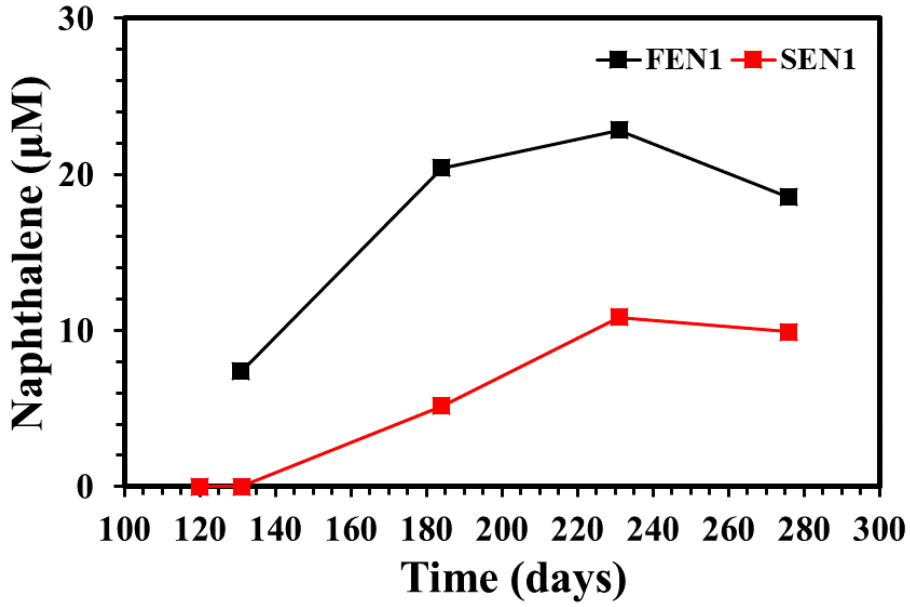

Figure A2-1: Naphthalene concentration in FEN1 and SEN1 at depth 22.5 cm bss

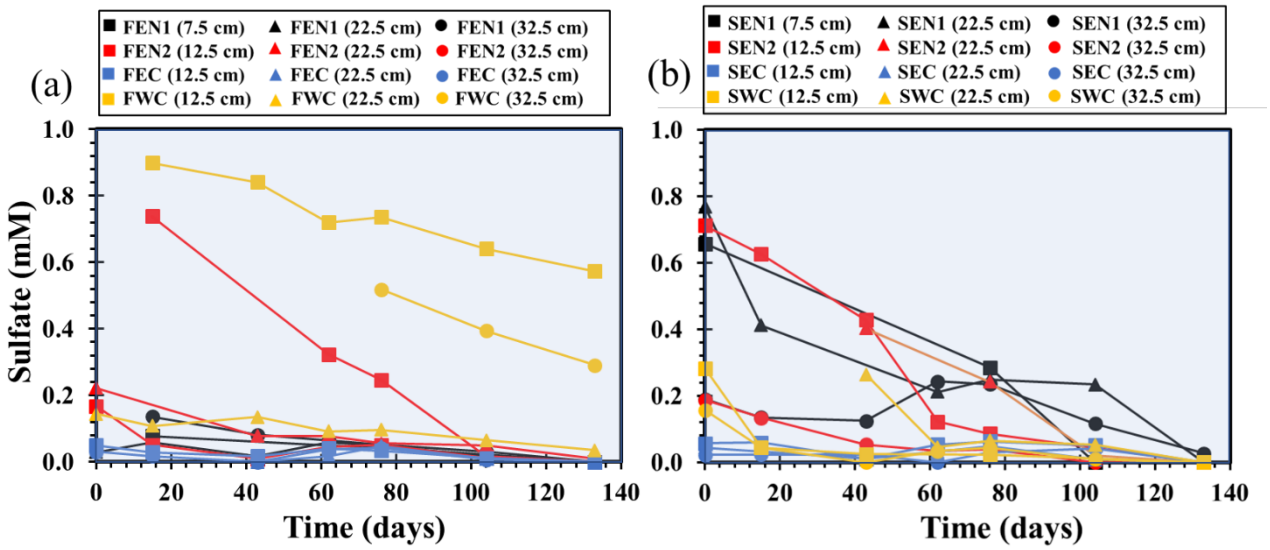

Figure A2-2: Sulfate concentrations measured at depths 2.5-32.5 cm bss in (a) the fluctuating water table columns, and (b) the static water table soil columns.

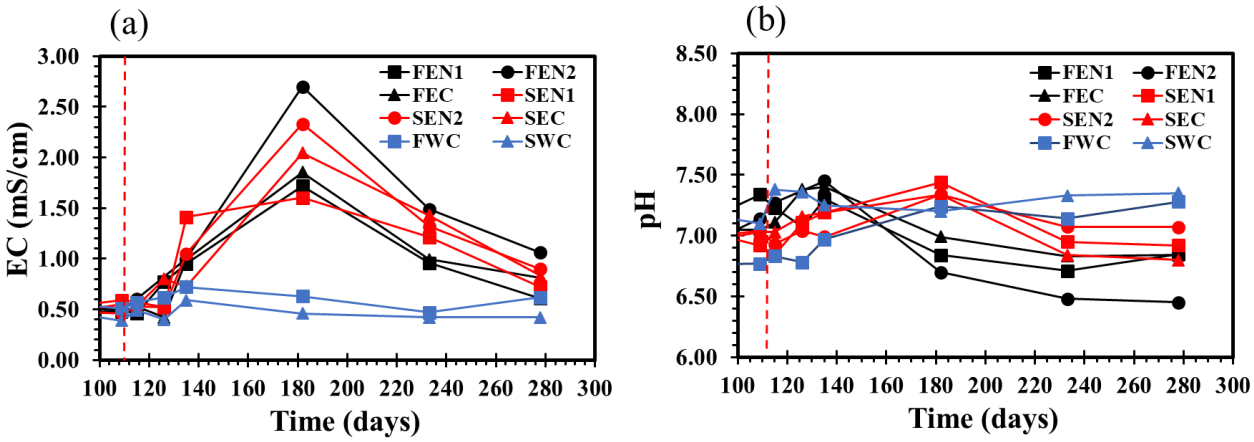

Figure A2-3: The average (a) pH and (b) EC in the fluctuating and the static water table columns.